AN INVESTIGATION OF WAVE-INDUCED MOMENTUM FLUX THROUGH PHASE AVERAGING OF OPEN OCEAN WIND AND WAVE FIELDS

by

Suzanne W. Wetzel

B.S.E., Princeton University (1994)

Submitted in partial fulfillment of the
requirements for the degree of

MASTER OF SCIENCE
at the
MASSACHUSETTS INSTITUTE OF TECHNOLOGY
and the
WOODS HOLE OCEANOGRAPHIC INSTITUTION

September 1996

Signature of Author .....
Joint Program in Applied Ocean Physics and Engineering
Massachusetts Institute of Technology / Woods Hole Oceanographic Institution

Certified by .....
James B. Edson
Associate Scientist, Woods Hole Oceanographic Institution
Thesis Supervisor

Certified by .....
Dara Entekhabi
Associate Professor, Department of Civil and Environmental Engineering, MIT
Thesis Reader

Accepted by .....
Professor Henrik Schmidt
Acting Chairman, Joint Committee for Applied Ocean Physics and Engineering
Massachusetts Institute of Technology / Woods Hole Oceanographic Institution

AN INVESTIGATION OF WAVE-INDUCED MOMENTUM FLUX THROUGH PHASE AVERAGING OF OPEN OCEAN WIND AND WAVE FIELDS

by

Suzanne W. Wetzel

Submitted in partial fulfillment of the requirements for the degree of
Master of Science at the Massachusetts Institute of Technology and the
Woods Hole Oceanographic Institution.

September 1996

ABSTRACT

This thesis presents an investigation of the influence of the dominant, wind-driven, surface waves on the vertical flux of horizontal momentum in the marine surface layer over open ocean conditions. Through a procedure which involves phase averaging the wind fields at the period of the dominant waves, the wave-induced component of the atmospheric fluctuations is isolated and vertical profiles of mean wave-induced momentum flux are computed.

Previous investigators have used phase averaging to remove the turbulence from an oscillatory signal, but the absence of a monochromatic wave field in open ocean conditions complicates this approach. This difficulty is overcome by choosing only the time periods characterized by the most monochromatic-like waves present and filtering those sections of wind data with a narrow band-pass filter centered around the dominant wave frequency before beginning the phase averaging process.

The analysis is carried a step further by investigating the dependence of wave-induced momentum flux on sea state through bin averaging according to wave age. This results in a set of profiles which express the ratio of wave-induced momentum flux to the total flux as a function of the wave age parameter, c/U_{10}. These profiles all tend to zero with height, and remain negligible at all heights over fully developed seas. Over younger seas, this ratio becomes increasingly more positive (corresponding to a positive value for $-\tilde{u}\tilde{w}$) with decreasing wave age; while over older seas, this ratio becomes increasingly more negative with increasing wave age. This provides strong quantitative evidence that there is a significant flux of momentum to the atmosphere from decaying waves, and a transfer of atmospheric momentum to developing waves.

Thesis Supervisor: Dr. James B. Edson
Title: Associate Scientist, WHOI

ACKNOWLEDGEMENTS

I would like to extend my sincerest thanks to my thesis advisor Dr. Jim Edson for his continual support. His enthusiasm for the project and his unselfish committment to my progress provided encouragement and greatly enhanced my experience in the Joint Program. The long hours Jim spent patiently sharing ideas with me contributed directly to this thesis and are deeply appreciated.

A number of other faculty and staff at the Woods Hole Oceanographic Institution have also played an important role in the completion of this thesis and my progress leading up to it. Dr. Tim Duda was my advisor during my first year in the program, and I am grateful for his guidance and time he spent sharing his wisdom with me, on topics ranging from microstructure of the ocean to surfing in San Diego. I am grateful to Dr. Dara Entekhabi for his support over the past two years and his help as a reader of this thesis. Also, the assistance of Judith Ann White, Julia Westwater, and Jake Peirson is deeply appreciated. Jeff Hare provided helpful advice during my first summer on this project, as well as entertainment during dull moments in the office.

I would also like to thank Dr. Carl Friehe, Scott Miller, and Tihomir Hristov of the University of California, Irvine for their thoughtful discussions and their efforts in collecting and analyzing the data.

My Parents, Nana, and siblings have supported me greatly through their continued confidence in me and their friendly correspondence. A final word of thanks to friends who have provided me with insight, perspective, and companionship, especially Hank, Rebecca, and Brenda.

This project was funded by ONR grants N00014-95-1-0804 and N00014-96-1-0012.

TABLE OF CONTENTS

1. INTRODUCTION

The exchange of momentum, heat, and mass across the air-sea interface plays an important role in determining the dynamics and thermal properties of the atmosphere and the ocean. In order to understand either media, it is essential to understand how they interact through the transport, or flux, of quantities across their common boundary. For modeling applications, these fluxes constitute the boundary conditions that force any coupled ocean-atmosphere model. They are also of practical importance in predicting sea surface conditions for use in studies of sediment transport processes, forecasts of wave heights, and interpretation of microwave sea surface radar back-scatter signals.

The vertical flux of horizontal momentum across an interface is defined as the amount of horizontal momentum being transferred across the surface per unit time per unit area, with units of $\left[\frac{M}{LT^2}\right]$. This exchange of momentum is reasonably well understood at the land-atmosphere boundary (*Businger et al.,* 1971), yet we have a much poorer understanding about the fluxes between the atmosphere and the ocean. Over a land surface, momentum flux is comprised of viscous and turbulent components which transmit momentum to the land from the atmosphere. The production of turbulent kinetic energy from the mean flow is equal to the momentum flux times the mean wind shear. Most of this energy is irreversibly dissipated into thermal energy through viscous dissipation. The remainder of the energy is then dissipated by working against the land surface by blowing leaves, felling trees, or carving out hilly landscapes.

Over the ocean, the momentum flux gains an additional component due to the presence of surface waves. These waves influence the transfer of momentum across the air-sea boundary primarily through form drag. The breaking and dissipation of these waves, together with the viscous stress on the surface, contributes to the generation of surface currents and the development of the surface mixed layer. The near surface turbulent and wave-induced fluctuations that are related to these atmosphere-ocean interactions exert a strong influence on evaporation, precipitation, and gas fluxes; which then contribute to global ocean circulation, storm dynamics and, eventually, long term climate changes.

Despite its importance, the influence of the wave field on the overlying atmospheric flow is poorly understood. A strong wave-induced component to the vertical flux of horizontal momentum across an air-water interface has been observed (*Hsu et. al*, 1981; *Mastenbroek et. al*, 1996), but this behavior has yet to be studied comprehensively, particularly in open ocean conditions. Experiments at sea are more difficult to carry out because of the moving platform, flow distortion, and the specialized equipment that is necessary. The analysis of such studies is also difficult because it involves uncertainties that are not present at the land-atmosphere boundary, including the unsteady interface (resulting in ambiguity about the reference height) and the continually changing surface roughness. As a result, the influence of surface waves on atmosphere-ocean fluxes is not well known and scientists often ignore the effect of waves on surface fluxes in numerical models, using parameterizations based on land-derived relationships instead.

The research presented in this thesis is an investigation of the influence of surface waves on the vertical flux of horizontal momentum at the air-sea interface for open ocean conditions. Through a procedure which involves phase averaging of the atmospheric velocity field at the period of the dominant waves, the wave-induced component of the velocity fluctuations is isolated and vertical profiles of mean wave-induced momentum flux are computed. These flux profiles are bin averaged using a parameter that describes the state of wave development (i.e., developing, fully developed, or decaying) to investigate a dependence on sea state.

Chapter 2 provides an introduction to the well-accepted Monin Obukhov similarity theory, its validation over the land surface, and the difficulties in applying this theory to the marine boundary layer. A discussion of the motivation for this study and an introduction to the current state of research in this field, followed by a brief description of the approach of this thesis, is also presented in Chapter 2. Details of the experiment, the instrumentation, and data processing are described in Chapter 3. In an effort to apply the theory of conventional analysis tools to an open ocean setting, some new analysis techniques are employed in this study. These are discussed in Chapter 4. The results of bin averaging the momentum flux profiles are presented in Chapter 5, followed by a discussion of the results. The thesis concludes with a summary of the findings and plans for future research in Chapter 6.

2. BACKGROUND

2.1 MONIN-OBUKHOV SIMILARITY THEORY

The Monin-Obukhov (MO) similarity theory relates turbulent fluxes of atmospheric momentum and heat to the more easily measured mean quantities such as wind speed and temperature. This theory includes mechanical and thermal forcing in the description of surface-layer turbulence, and predicts that the structure of turbulence is based on the relative strength of these two forcing mechanisms. It was developed nearly fifty years ago (*Obukhov*, 1946; *Monin and Obukhov*, 1954) and has since been validated over land by a number of field experiments including the 1968 Kansas (*Businger et al.*, 1971), the 1973 Minnesota (*Champagne et al.*, 1977), and the 1976 International Turbulence Comparison (*Dyer and Bradley*, 1982) experiments. The semi-empirical relationships derived from these experiments are widely used to predict turbulent quantities when direct measurement is not practical, and to estimate the lower boundary flux conditions for numerical forecasts with the mean variables available from the model.

2.1.1 GOVERNING EQUATIONS

The planetary boundary layer is the region of the atmosphere, typically the lowest 1-2 km, in which surface effects are linked to the atmosphere through the vertical exchange of momentum, heat, and moisture. The wind above the planetary boundary layer is generally assumed to be geostrophic, or characterized by a balance between the coriolis force and pressure gradient:

$$\begin{aligned} fV_g &= \frac{1}{\rho_a}\frac{\partial p}{\partial x} \\ fU_g &= -\frac{1}{\rho_a}\frac{\partial p}{\partial y} \end{aligned} \tag{2.1}$$

where $f = 2\Omega\sin\phi$ is the coriolis parameter, ρ_a is air density, p is air pressure, and U_g and V_g represent the geostrophic velocities in the longitudinal (x) and lateral (y) directions, respectively. Within the planetary boundary layer, frictional forces give rise to an

ageostrophic velocity component and the governing equations are

$$\frac{du}{dt} - f(v - V_g) = \frac{1}{\rho_a}\left(\frac{\partial \tau^{xx}}{\partial x} + \frac{\partial \tau^{xy}}{\partial y} + \frac{\partial \tau^{xz}}{\partial z}\right)$$
$$\frac{dv}{dt} + f(u - U_g) = \frac{1}{\rho_a}\left(\frac{\partial \tau^{yx}}{\partial x} + \frac{\partial \tau^{yy}}{\partial y} + \frac{\partial \tau^{yz}}{\partial z}\right) \qquad (2.2)$$

where the τ^{ij} terms represent the surface stresses acting in the i direction on a plane perpendicular to the j axis; u and v are the velocities along the i and j axes, respectively; and $\frac{d}{dt} = \frac{\partial}{\partial t} + u\frac{\partial}{\partial x} + v\frac{\partial}{\partial y} + w\frac{\partial}{\partial z}$ is the total, or material, derivative. Note that the pressure gradient terms have been related to geostrophic velocity according Equation 2.1.

The lowest part of the planetary boundary layer is called the surface layer. According to the MO theory, only a few governing parameters are necessary to describe the structure of atmospheric turbulence in the surface layer, provided the boundary layer conditions satisfy the following constraints: (1) turbulence is influenced only by mechanical and thermal forcing; (2) the atmospheric processes are horizontally homogeneous, quasi-stationary and with no subsidence; (3) the effects of the earth's rotation (i.e., the coriolis force) can be ignored; and (4) the fluxes associated with the mechanical and thermal forcing are constant with height. The assumptions of stationarity and horizontal homogeneity imply that $\frac{\partial}{\partial t} = 0$ and $\frac{\partial}{\partial x} = \frac{\partial}{\partial y} = 0$, respectively, and from the assumption of no subsidence it follows that $w = 0$. Equation 2.2 then becomes:

$$-f(v - V_g) = \frac{\partial \tau^{xz}}{\partial z}$$
$$f(u - U_g) = \frac{\partial \tau^{yz}}{\partial z} \qquad (2.3)$$

Here τ^{xz} and τ^{yz} are the longitudinal (x) and lateral (y) shear stresses on the plane perpendicular to the vertical (z) axis.

Equation 2.3 illustrates that the last two constraints (negligible coriolis force, constant flux layer) are never really satisfied in the atmospheric boundary layer. Instead, the geostrophic

component of the coriolis force is balanced by a vertical flux divergence. This balance leads to a situation where the shear stress varies in both magnitude and direction, as well as Ekman spiral-like solutions of the velocity structure of the atmospheric and oceanic boundary layers when certain constraints are placed on the form of the shear stresses (*Holton*, 1979). However, a good approximation to the constant flux layer is obtained by limiting the definition of the surface layer to the region where fluxes vary by 10% or less from their surface values. Since the momentum flux generally decreases linearly with height, this definition results in a surface layer that occupies the lowest 10% of the atmospheric boundary layer. This has the additional advantage of ensuring that the wind and stress vectors are closely aligned so that the lateral component arising from the earth's rotation can be ignored. Thus, the governing equations of the surface layer reduce to:

$$0 \approx \frac{\partial \tau^{xz}}{\partial z}$$
$$0 \approx \frac{\partial \tau^{yz}}{\partial z} \qquad (2.4)$$

2.1.2 Similarity Parameters

A similarity theory is based on the premise that normalizing measurements by the appropriate scaling parameters provides a means of comparing turbulent statistics measured at different times and places but under similar conditions. Provided the scaling parameters are chosen properly, measurements from one experiment corresponding to the same non-dimensional quantity as those from another experiment should exhibit similar behavior.

Monin-Obukhov similarity theory predicts that the parameters relevant to describing the statistical nature of turbulent flow are

characteristic eddy size	$z \equiv$ distance from ground	
surface stress vector	$\vec{\tau}_o$	(2.5)
buoyancy parameter	$g / \overline{\theta}_v$	
surface buoyancy flux	$Q_o = \overline{\theta_v' w'}$	

where θ_v is the virtual potential temperature and g is the acceleration due to gravity. These four variables can be combined to define two length scales, two velocity scales, and two temperature scales. However, these six scaling variables are not independent (*Wyngaard*, 1973) and it is traditional to choose both length scales, one velocity scale, and one temperature scale:

$$\begin{aligned} &\text{length} && z \\ & && L = \frac{-u_*^3}{\kappa g Q_o / \overline{\theta}_v} \\ &\text{velocity} && u_* = \left| \frac{\vec{\tau}_o}{\rho_o} \right|^{1/2} = [\,(\overline{u'w'})^2 + (\overline{v'w'})^2\,]^{1/4} \\ &\text{temperature} && \theta_* = -\frac{Q_o}{u_*} = -\frac{\overline{\theta_v' w'}}{u_*} \end{aligned} \tag{2.6}$$

where ρ_o is density of air at the surface, κ is von Karman's constant, generally assumed to equal 0.4, and u', v', and w' are the longitudinal, lateral, and vertical velocity fluctuations, respectively. According to the MO similarity hypothesis, a surface layer turbulent quantity normalized by a combination of these scaling parameters will result in a universal non-dimensional function. That is, the non-dimensional function will exhibit the same structure and behavior for all atmospheres consistent with the assumptions of MO similarity.

An example of a similarity function of particular interest to marine meteorologists is the dimensionless wind shear, defined as

$$\phi_m(\zeta) = \frac{\kappa z}{u_*} \left[\left(\frac{\partial \overline{u}}{\partial z} \right)^2 + \left(\frac{\partial \overline{v}}{\partial z} \right)^2 \right]^{1/2} \tag{2.7}$$

where $\zeta = z/L$ is the dimensionless height parameter, z is height above the surface, and L is the Monin-Obukhov length:

$$L = \frac{\overline{\theta}_v u_*^2}{g\, \theta_*} \tag{2.8}$$

2.1.3 VALIDATION

Numerous overland field experiments conducted during the late sixties and seventies have led to a validation of Monin-Obukhov similarity theory for the land-atmosphere surface layer and helped to establish it as a well-accepted theory. The results are widely used and the similarity relations considered universal. *Högström* (1988) presents a comparative study of various results of non-dimensional wind shear profiles $\phi_m(\zeta)$, including the well-accepted formulae of *Businger et al.* (1971) and *Dyer* (1974). Figures 2.1 and 2.2 show $\phi_m(\zeta)$ from various studies for unstable and stable stratification, respectively. The curves in these figures have been modified from the original relations to account for flow distortion. *Högström*(1988) concludes that the discrepancies in the results of different studies do not reflect real differences but rather instrumental shortcomings. Thus, the consistency of the results indicates that ϕ_m is a universal function of ζ in accordance with Monin-Obukhov similarity theory. These results have been generalized into a form which has been accepted universally over land. For unstable and stable conditions, respectively, the following expressions for the non-dimensional shear function, called the Businger-Dyer formulae, are the most widely used (*Panofsky and Dutton*, 1984):

$$\begin{aligned} \phi_m(\zeta) &= (1 - 16\,\zeta)^{-1/4} && \zeta < 0 \\ \phi_m(\zeta) &= 1 + 5\,\zeta && \zeta \geq 0 \end{aligned} \qquad (2.9)$$

2.2 MOTIVATION FOR STUDY

Although the assumptions of Monin-Obukhov similarity theory may be satisfied for the general case over land, there are still spatial limits to its applicability. The preceding discussion showed that even in homogeneous and stationary conditions, the region where MO theory applies is bounded by the height of the surface layer, above which rotational effects can no longer be ignored and the fluxes cannot be considered constant. Additionally, there is a lower bound to the region of applicability of this theory. Very close to the land surface,

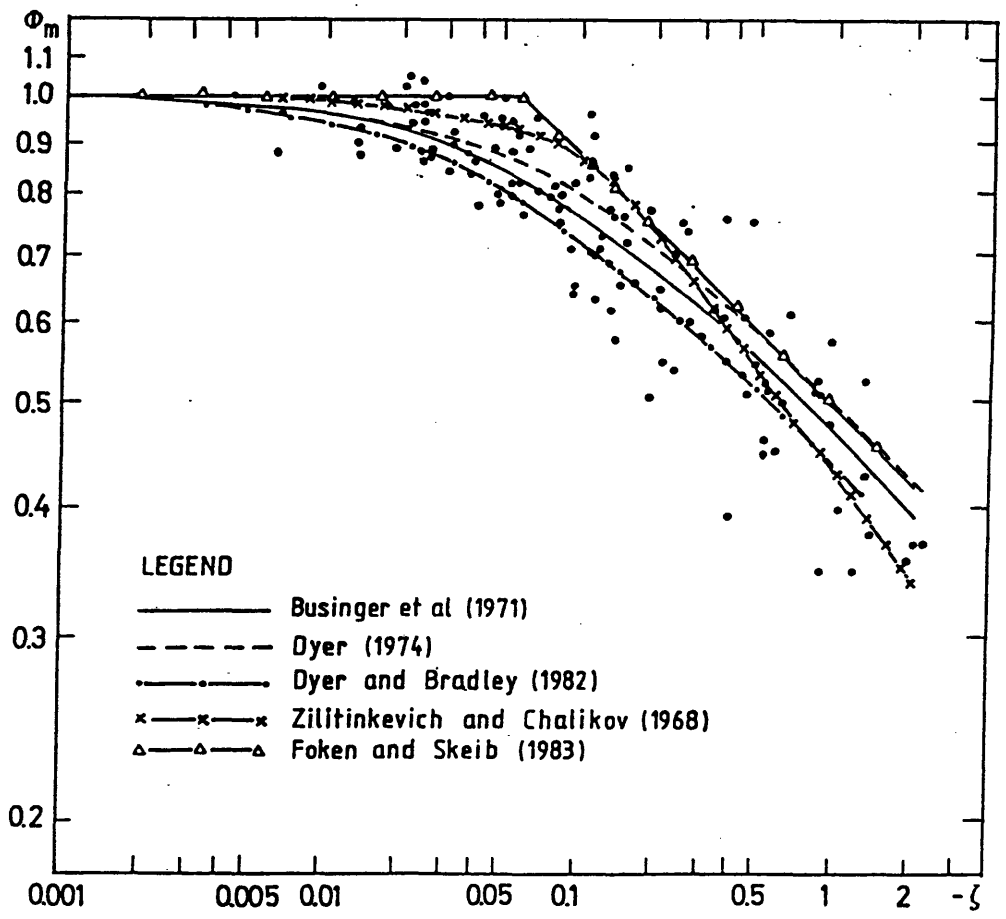

Figure 2.1 Non-dimensional wind shear function $\phi_m(\zeta)$ for unstable stratification from various overland field experiments. The agreement among the results indicates that dimensionless wind shear is a universal function of the dimensionless height parameter ζ for these conditions over land (from *Högström*, 1988).

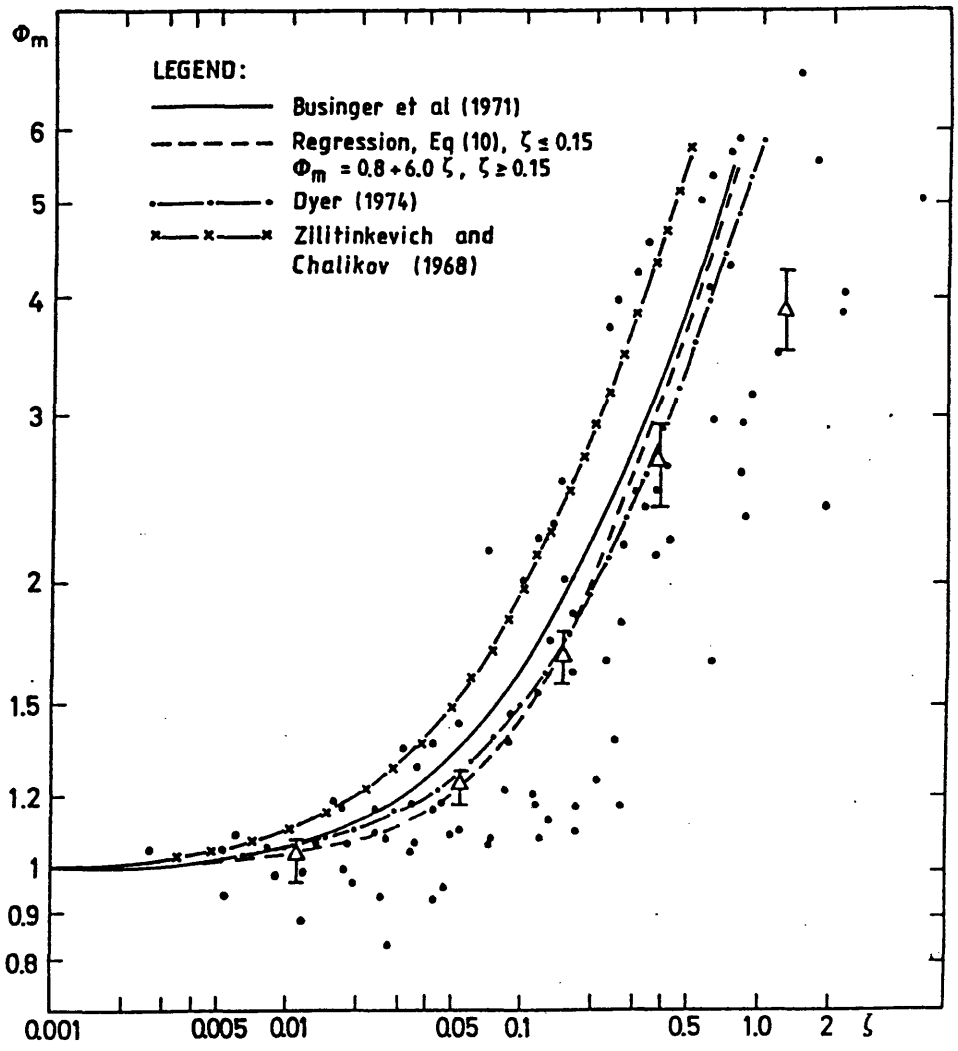

Figure 2.2 Non-dimensional wind shear function $\phi_m(\zeta)$ for stable stratification from various overland field experiments. The agreement among the results indicates that dimensionless wind shear is a universal function of the dimensionless height parameter ζ for these conditions over land (from *Högström*, 1988).

molecular viscosity becomes an important factor in the structure of the flow, and the assumptions of MO theory are not satisfied. This is illustrated by adopting the following decomposition for the total flux ($\vec{\tau}_T$) in the atmospheric surface layer:

$$\vec{\tau}_T(z) = \vec{\tau}_t(z) + \vec{\tau}_v(z) \tag{2.10}$$

where

$$\vec{\tau}_t = -\rho [\hat{i} (\overline{u'w'}) + \hat{j} (\overline{v'w'})] \tag{2.11}$$

is the turbulent momentum flux, and

$$\vec{\tau}_v = \mu \frac{\partial \vec{u}}{\partial z} \tag{2.12}$$

is the flux due to viscous stress. Based on the constant flux hypothesis discussed in Section 2.1.1, the vertical flux profiles should behave as sketched in Figure 2.3. Note that a positive momentum flux indicates a transfer of momentum from the atmosphere to the land. Near the surface in a region termed the viscous sub-layer, the viscous effects dominate and the turbulent component becomes negligible, maintaining a constant total flux. Since the governing parameters of Monin-Obukhov similarity theory only describe the behavior of turbulent fluctuations driven by mechanical and thermal forcing, Figure 2.3 implies that MO theory does not apply inside the viscous sub-layer. *Godfrey and Beljaars* (1991) found that the depth of the viscous sub-layer corresponds to the height of surface roughness, z_o. This value of surface roughness is defined as the height of 'zero' wind speed, found by extrapolating down from the logarithmic wind profile measured well above z_o. Thus, when z or L is of the same order as z_o, the influence of molecular viscosity becomes significant and Monin-Obukhov similarity theory breaks down.

Over the ocean there is evidence that additional spatial limits to MO theory exist due to the presence of waves, yet these limits have not been quantified. It is readily observed that the surface waves exert an influence on the overlying winds. Figure 2.4 shows an illustration of this coupling from a 5-minute section of data. Even as high as the upper sonic anemometer

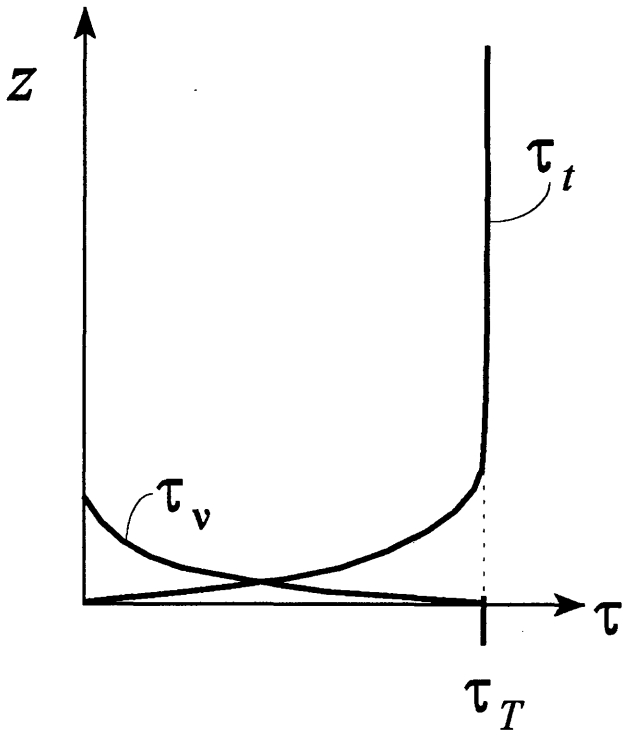

Figure 2.3 Illustration of the vertical decomposition of momentum flux (τ) in the land-atmosphere surface layer. Viscous effects (τ_v) dominate near the boundary and the turbulent component (τ_t) becomes negligible, maintaining a constant total flux (τ_T).

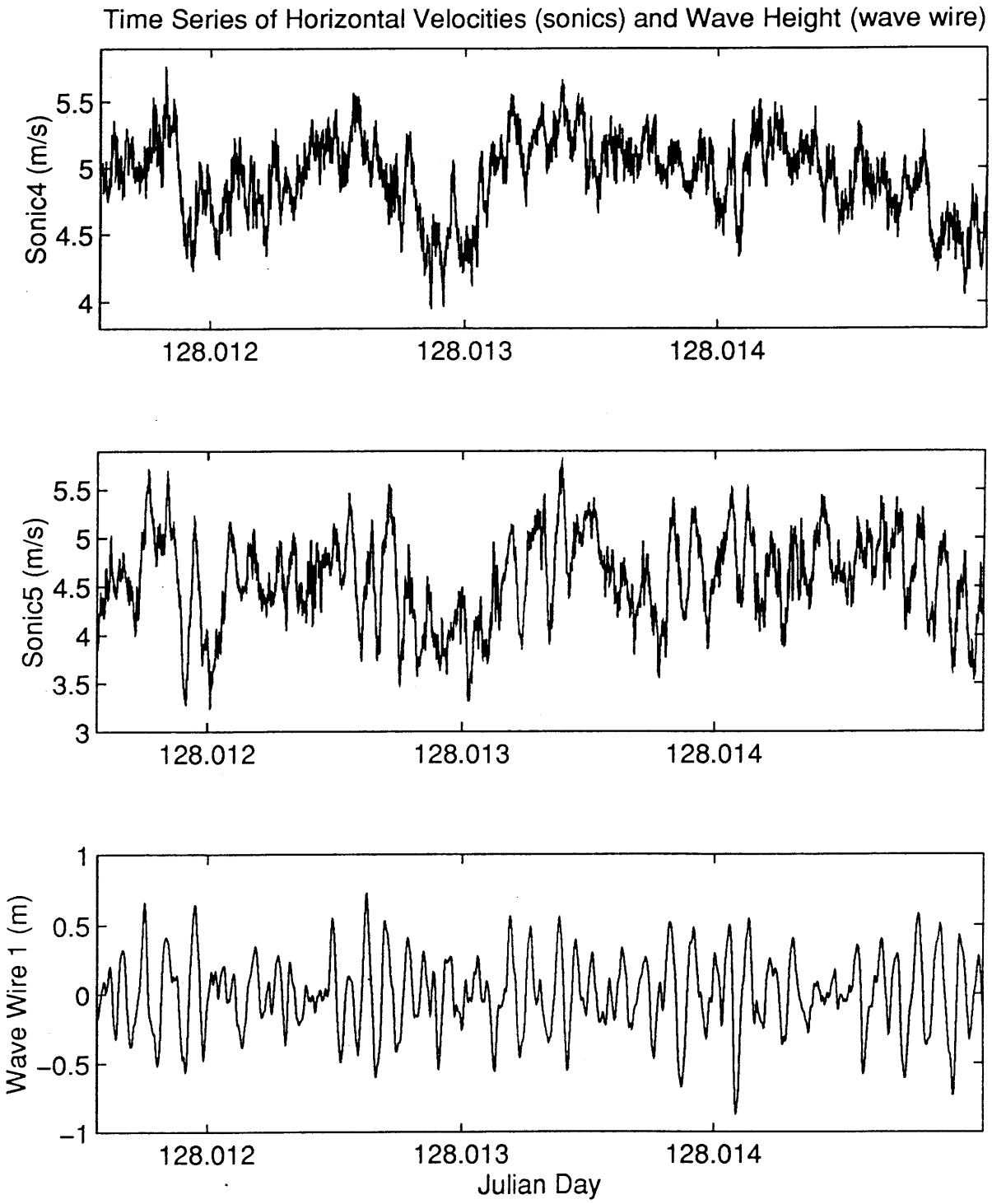

Figure 2.4 Time series of horizontal wind velocity from the upper (sonic 4, at 18.12 m above sea level) and lower (sonic 5, at 3.9 m) levels of sonic anemometers. Both show a strong correlation with the time series of the underlying wave field (wave wire 1). The decrease in wave heights just before day 128.013 is accompanied by a corresponding drop in horizontal wind velocities at both heights.

(18 m above mean sea level), a visual inspection of the time series reveals that the horizontal velocities are notably correlated to the wave heights.

Though difficult to measure directly, it is well known that wave-induced atmospheric fluctuations translate into wave-induced momentum flux. Thus, the flux partitioning presented earlier (Equation 2.10) which is valid over the land must be modified to account for the presence of waves. An additional term, the wave-induced component of the flux, $\vec{\tau}_w$ is added to the flux decomposition to extend its validity to the marine surface layer:

$$\vec{\tau}_T(z) = \vec{\tau}_t(z) + \vec{\tau}_w(z) + \vec{\tau}_v(z) \tag{2.13}$$

The wave-induced component of total flux is a result of the uneven air pressure distribution across the front and rear faces of the waves. This is known as form drag and results from small scale gravity-capillary waves as well as from larger waves. Form drag from the small scale roughness elements is always present, even at very low wind speeds. At high wind speeds, these gravity-capillary waves tend to be more prominent on the backs of the longer waves. In general, the long waves only have a noticeable effect on the air flow when the sea state is developing or decaying (*Geernaert*, 1988). A fully developed steady state sea has a negligible form drag component of the momentum flux due to the long waves (*Hasselmann et al.*, 1991), such that potential flow theory provides a good model of the flow over the waves.

It is common practice to assume that the constant flux hypothesis derived over land can be extended to the marine surface layer (*e.g., Chalikov and Belevich*, 1993). A layer of constant flux implies that the momentum budget 'adjusts' to accommodate the additional wave-induced momentum flux near the boundary. Disregarding the effects of molecular viscosity, this behavior is sketched for the case of a developing sea in Figure 2.5a and for a decaying sea in Figure 2.5b. Because these figure assume a constant flux layer, the sum of turbulent and wave-induced components remains constant. Well away from the surface the wave-induced components tend to zero and the turbulent components dominate. For the developing sea when it is expected that the atmosphere is giving momentum to the waves, the

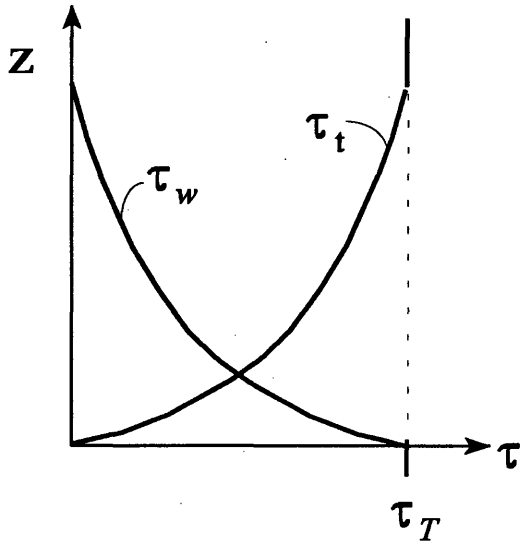

Figure 2.5a Conceptual momentum flux profile over a developing sea, neglecting viscous effects. This sketch assumes that total flux remains constant, as is the case over land. The wave-induced component (τ_w) approaches zero with height and the turbulent effects dominate. Near the surface, the wave-induced flux is positive, indicating a transfer of momentum from the atmosphere to the ocean wave field.

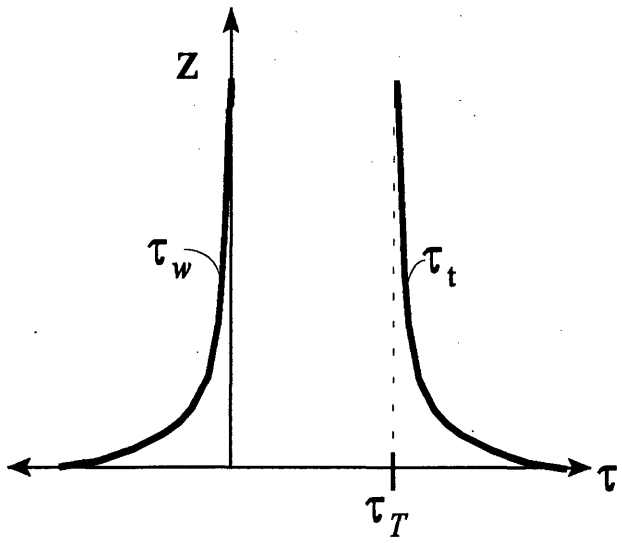

Figure 2.5b Conceptual sketch of the vertical decomposition of flux contributions from wave and turbulent effects for a decaying sea, under the assumption that total flux remains constant with height. The turbulent flux must increase considerably near the surface to maintain a constant total flux.

wave-induced flux is positive, or downward (corresponding to a positive value for τ_w), and the turbulent component tends to zero, maintaining a constant total flux. For a decaying sea, it is expected that the direction of transfer is reversed, i.e., the waves provide momentum to the atmosphere. Thus, the turbulent component must increase near the surface to compensate for the wave-induced flux if the assumption of a constant flux layer is to hold.

At heights above the layer of wave influence where flux is only a function of turbulence, it is assumed that MO theory applies. Therefore, the turbulent component of flux at this height is equal to the total momentum flux at the surface regardless of the influence of the waves, provided that the total flux is constant. The wind shear function introduced in Section 2.1.2 can be used to illustrate this behavior. An additional term ϕ_w can be added to the non-dimensional wind shear function to represent the wave-induced contribution:

$$\frac{\kappa z}{u_{*T}} \frac{\partial u_H}{\partial z} = \phi_m(\zeta) + \phi_w(?) \tag{2.14}$$

where u_{*T} represents the total surface momentum flux, including the turbulent, viscous, and wave-induced components. As indicated by the question mark, not much is known about the function ϕ_w. However, above the wave boundary layer, total momentum flux u_{*T} is equal to the turbulent momentum flux u_*, and ϕ_w must be negligible. Equation 2.14 then reduces to the conventional MO similarity relation for non-dimensional shear (Equation 2.7). If measurements are made outside the wave boundary layer and the assumption that total flux is constant over the ocean, this provides a means of estimating surface fluxes without understanding the structure and partitioning of the wave-induced component ϕ_w.

However, measurements at height are not always available. For example, data from surface buoys is often collected within the wave boundary layer, and most air-sea models must compute surface fluxes given near-surface meteorological information. Additionally, it is not clear that the constant flux hypothesis and MO theory, derived over land, can be extended to the marine surface layer. For this to be a reasonable extension, the assumptions of horizontal homogeneity, stationarity, and no subsidence must all apply. Yet even if these conditions exist there is good reason to believe that the assumption of a constant flux layer

is often invalid within the wave boundary layer (this is discussed further in Chapters 5 and 6). Thus, the theory behind the analysis techniques used in this thesis are independent of the assumption that total momentum flux is constant within the marine surface layer, and the results can be used to investigate the validity of this assumption.

2.3 Current State of Research

A first step in understanding the behavior of the wave-induced momentum flux is to determine the spatial limits to the influence of the waves and thus the range of applicability of Monin-Obukhov similarity theory over the ocean. The analogous problem over land was discussed at the beginning of Section 2.2. A widely used, simple parameterization developed by *Charnock* (1955) defines the height of the wave boundary layer, or roughness height, in a fully developed sea in the absence of any form drag by long waves,

$$z_{o_c} = \alpha \frac{u_*^2}{g} \tag{2.15}$$

where α is an empirical constant that is approximately equal to 0.011 for open ocean conditions (*Fairall et al.*, 1996a). *Smith* (1988) added the well known parameterization for the roughness length in smooth flow,

$$z_o = z_{o_c} + 0.11 \frac{\nu}{u_*} \tag{2.16}$$

to parameterize both viscous drag and the form drag from the gravity-capillary waves. For steady state conditions, this height provides an estimate of the lower limit of applicability of Monin-Obukhov similarity theory. As in the case over land, if either z or L is of the same order as z_o, then the effects of viscosity and form drag become significant and MO similarity theory breaks down. Charnock's relation has proved to be an accurate parameterization of the surface roughness for the condition of a fully developed sea, yet this condition is rarely met in coastal seas and over substantial portions of the open ocean at any given time. For a developing or decaying sea, the additional effects of form drag from the longer waves must

also be considered. Little is known about the structure and height of this wave-induced flow above the surface and there have been no direct measurements at sea.

However, there is significant indirect evidence from field data indicating that the magnitude of the total momentum flux is a function of sea state. For example, measurements of the drag coefficient at sea have been observed to exhibit a wave age dependence. The drag coefficient is defined by the relation

$$C_D\,[u(z) - u(z_o)]^2 = u_*^2 \tag{2.17}$$

Using the integrated form of the non-dimensional shear (to be introduced in Section 3.2.3, Equation 3.21), the definition for C_D can be rewritten as

$$C_D = \left[\frac{\kappa}{\ln(z/z_o) - \psi_m(\zeta)}\right]^2 \tag{2.18}$$

This indicates that the drag coefficient should be a function only of stability (ψ_m) and surface roughness (z_o), if MO similarity holds. Therefore, for a given wind speed which would determine the roughness, the neutral drag coefficient (with $\psi_m(0) = 0$) should be a constant:

$$C_{DN} = C_D\left[1 + \frac{C_D^{1/2}\psi_m(\zeta)}{\kappa}\right]^{-2} = \left[\frac{\kappa}{\ln(z/z_o)}\right]^2 \tag{2.19}$$

However, results from experiments in the marine surface layer show considerable variation in the neutral drag coefficient. Figure 2.6 from *Geernaert* (1990), shows the drag coefficient as a function of wind speed for numerous field studies. The inconsistency in these results implies that there is no universal relation between wind speed and roughness over the ocean and suggests a dependence on an additional parameter. Results from a study by *Donelan et al.* (1993), shown here in Figure 2.7, found that field measurements of surface roughness length showed a strong dependence on wave age c_p/U_{10} where c_p is the phase speed of the waves at the spectral peak and U_{10} is the horizontal wind velocity measured at 10 m. Together these studies strongly support the idea that momentum flux is a function of wave age.

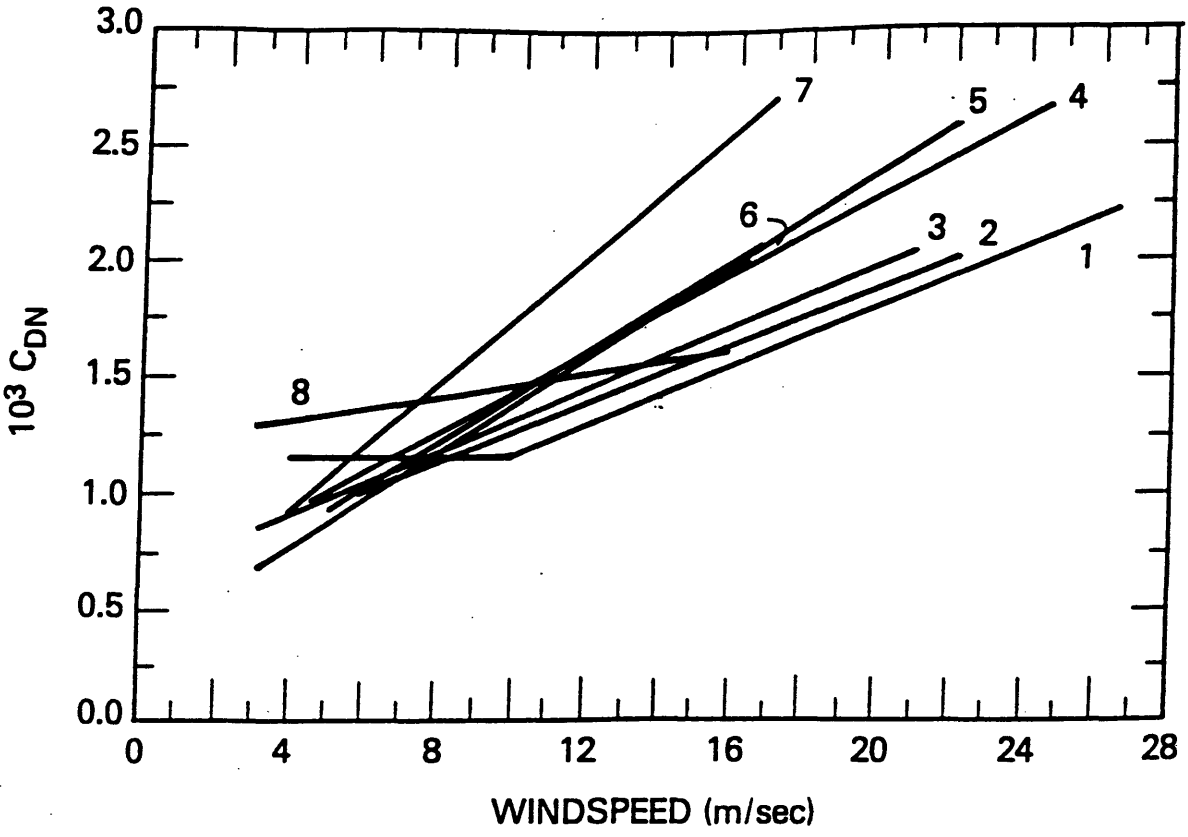

Figure 2.6 Distribution of neutral drag coefficient C_{DN} with wind speed from different marine boundary layer field experiments. Sites range from a deep ocean (1) to the 30 m and 16 m depths in the North Sea (4 and 5, respectively) to the shallow 3 m Lake Geneva (8). The systematic variation of these results suggests a dependence of C_{DN} on another parameter besides just wind speed (from *Geernaert*, 1990).

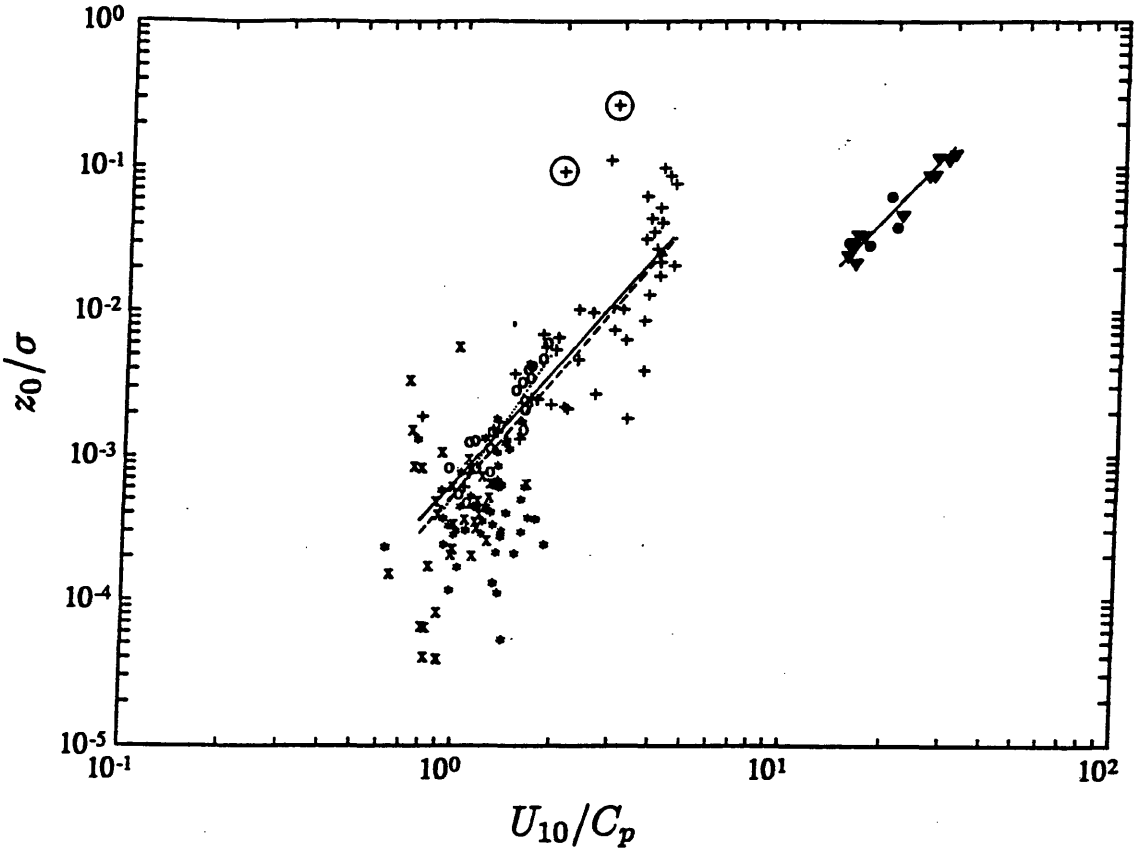

Figure 2.7 Ratio of roughness length z_o to rms wave height σ vs. inverse wave age U_{10}/c_p for open ocean field experiments with long fetch (*), limited fetch (x), Lake Ontario (+), and laboratory experiments (solid circles, triangles). The consistency in the results from field experiments strongly implies a wave age dependence of surface roughness (from *Donelan et al.*, 1993).

The closest any researcher has come to measuring wave-induced momentum flux directly in the field involves estimating form drag from the pressure-wave slope correlation term in the integrated horizontal momentum equation. This equation is (*Deardorff*, 1967):

$$\left[\overline{\tilde{u}\tilde{w}} + \overline{u'w'} + \nu\frac{\partial\bar{u}}{\partial z}\right]_h = \frac{1}{\rho_a}\overline{p_\eta\frac{\partial\eta}{\partial x}} + \nu\overline{\left(\frac{\partial u}{\partial z}\right)_\eta} - \nu\overline{\left(\frac{\partial u}{\partial x_i}\right)_\eta\frac{\partial\eta}{\partial x_i}} \qquad (2.20)$$

where η is wave height, p_η is the surface pressure, ρ_a is air density, ν is kinematic viscosity of air, and h is a reference elevation (often taken to be at $z = 10$ m above sea level). The three terms on the left-hand side represent the vertical flux of horizontal momentum at height h due to waves, turbulence, and viscosity, respectively. The first term on the right-hand side is the air pressure-wave slope correlation, and the second and third terms represent the viscous stress. Neglecting viscosity and evaluating Equation 2.20 at the surface where the turbulent components go to zero results in a relation expressing the wave-induced momentum flux, or form drag, as a function of the pressure-wave slope correlation:

$$\rho_a\,\overline{\tilde{u}\tilde{w}}\,|_\eta = \overline{p_\eta\frac{\partial\eta}{\partial x}} \qquad (2.21)$$

This suggests that measurements of wave-induced air pressure perturbation and wave slope can be used to quantify wave-induced momentum flux (*Snyder, et al.*, 1981). However, it is prohibitively difficult to measure pressure at the surface, and extrapolation from measurements at height is problematic because the structure of the wave-induced pressure field is not well known. *Hare* (1995) has shown that this is particularly true over developing waves, where the wave-induced pressure field associated with the form drag does not decay monotonically.

Although the structure of the wave boundary layer has yet to be studied comprehensively in open ocean conditions, laboratory experiments have provided researchers with direct measurements of the wave-induced wind and pressure fields and thus the momentum flux. The applicability of lab results to the open ocean is continually in question due to the difficulty in matching the various scales of motion. Wave reflection from the tank ends, unrealistic

wave fields, and limits to the range of conditions (wind speed, fetch) that can be generated contribute to the uncertainty in studying ocean wave phenomena in the laboratory. For example, a study by *Donelan et al.* (1993) noted that the roughness resulting from laboratory waves is notably less than that of the corresponding wave in the field. Although this result has been questioned by *Jones and Toba* (1995), the ensuing controversy merely emphasizes that more work is needed to understand the relationship between laboratory and field results. However, if the results can be properly scaled, laboratory studies provide a good idea of what to expect in the field. Additionally, techniques developed for the analysis of laboratory data are commonly used to study the behavior of the open ocean.

Hsu, Hsu, and Street (1981) measured the structure of the wave-induced turbulent flow field and found a significant contribution to the total momentum flux at the surface. This study used a wave-following coordinate system and phase averaging to isolate the organized wave component of the air flow above mechanically-generated 1 Hz deep water waves. The waves were maintained at a constant wave length and amplitude and the free stream air velocity was 2.4 m/s. The resulting wave age c/U_{10} was approximately 0.65 which corresponds to a developing sea. Wind speed was measured at 18 elevations, ranging from 0.016 m - 0.39 m above the water surface. The use of a wave-following coordinate system and these near surface measurements enabled them to resolve the velocity structure in the wave troughs, revealing a recirculating wind pattern (Figure 2.8).

By phase averaging the wind field at a period corresponding to the period of the underlying waves, they found that the surface values of the mean vertical flux of horizontal wave-induced momentum ($-\overline{\tilde{u}\tilde{v}}$ in their coordinate system) were positive and large compared to the turbulent momentum flux at the interface and decreased to a negative minimum before tending toward zero with height (Figure 2.9). They did not speculate why this overshoot occurs, although a similar behavior is noted in the results of modeling this flow field numerically (*Zou,*1995; *Mastenbroek et. al,* 1996). The positive values of surface wave-induced flux represents a transfer from the air to the water, as expected for developing waves. The maximum wave-induced flux at the surface corresponds to 47% of the total flux, using a value for friction velocity of $u_* = 0.0856$ computed from direct measurements. Their

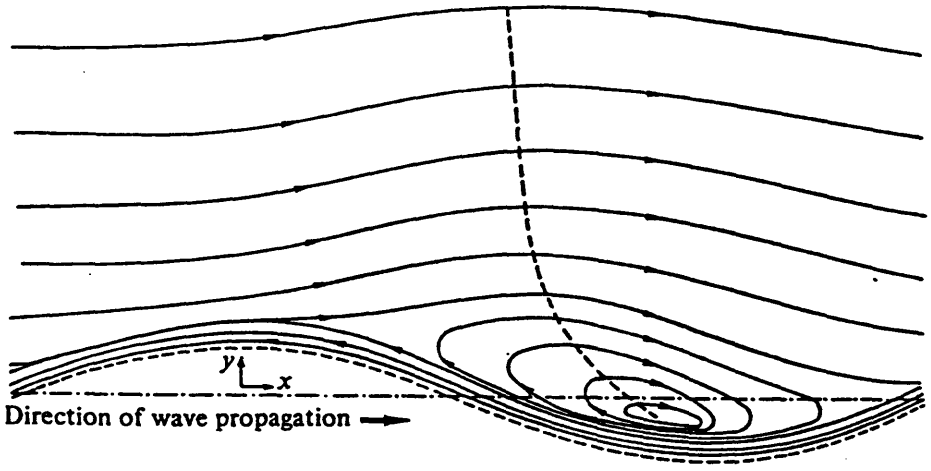

Figure 2.8 Sketch of the streamline pattern as observed in a frame moving with the wave speed (from *Hsu et al.*, 1981).

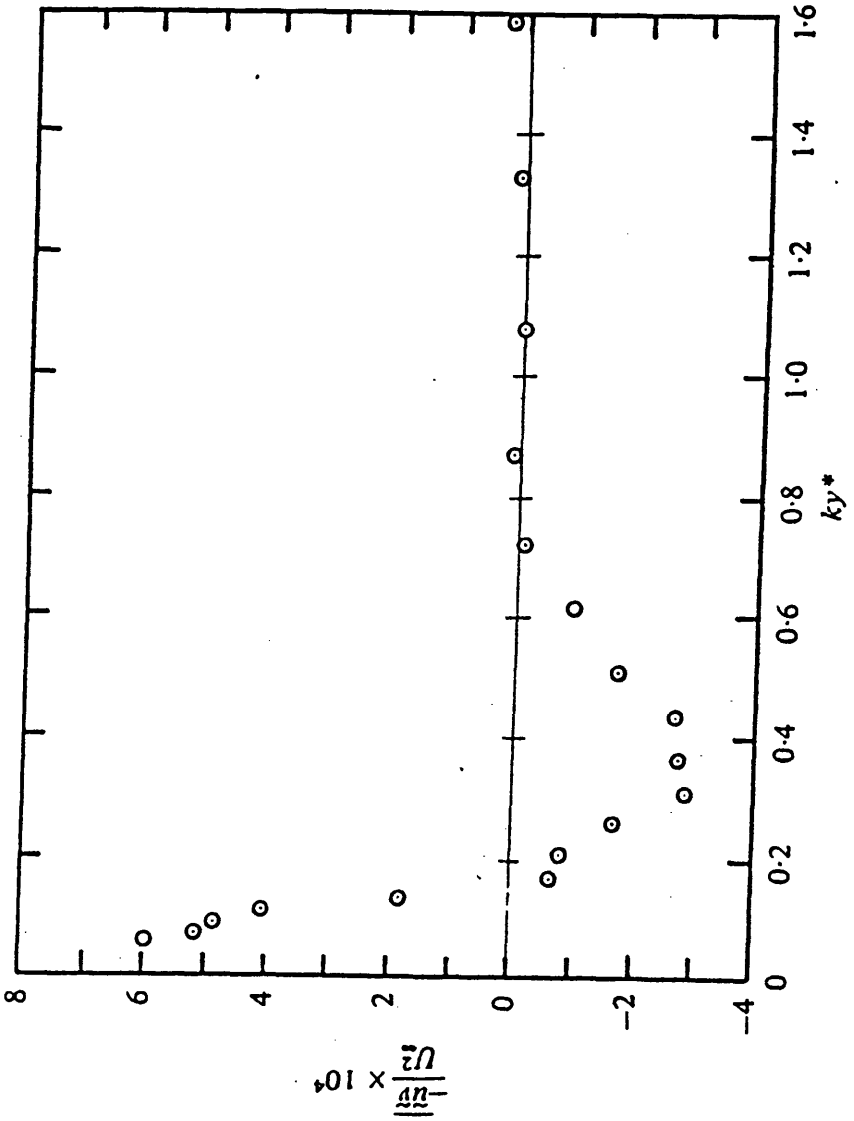

Figure 2.9 Distribution of wave-induced momentum flux ($-\overline{\tilde{u}\tilde{v}}$ in their coordinate system) normalized by free-stream velocity over a developing laboratory-generated wave field. Note that the sign of the x-axis is reversed (from *Hsu et al.*, 1981).

results also indicate that the wave influence becomes negligible at $ky^* = 0.8$, where y^* is distance above the water surface in a wave-following coordinate system, and $k = 4.03\ m^{-1}$ is the wave number. This study demonstrates the effectiveness of using phase averaging to measure the wave-induced velocities and therefore momentum flux. Since their experiment was limited to a monochromatic wave field, the techniques are not directly applicable to open ocean conditions but can be incorporated as part of the analysis of field data.

2.4 Approach of this Study

The analysis performed in this thesis is similar to that of *Hsu et al.* (1981), although some new techniques are employed to accommodate open ocean conditions. This study focuses on an open ocean field experiment and uses simultaneous measurements of wave heights and overlying wind speeds to investigate the influence of surface waves on momentum flux. A correlation between the wind and waves in the data is readily identified, as shown earlier by comparing time series of wind and wave data in Figure 2.4, and illustrated here in Figure 2.10. This figure compares the spectrum of vertical wind speeds measured with a sonic anemometer during this open ocean experiment with the well-accepted Kaimal w-velocity spectrum (*Kaimal et al.*, 1972):

$$S_w(f) = 2u_*^2 z \Big/ \left[\bar{u}\,(1 + 5.3f^{5/3})\right] \tag{2.22}$$

To identify the wave frequencies, the spectrum of wave heights (multiplied by 0.1) is also plotted. The open ocean velocities show a notable increase in wind energy at the dominant wave frequencies over that predicted by the Kaimal spectra. A similar behavior is observed for the u-velocity spectra. The Kaimal spectra were derived over land, so this behavior can be attributed to the disturbing influence of the waves.

These figures strongly imply a wave-induced component to the surface momentum flux. However, it is difficult to quantify this contribution because the atmospheric fluctuations also contain turbulence which must be separated from the wave components. As mentioned earlier, laboratory investigations have used phase averaging to remove the turbulence from

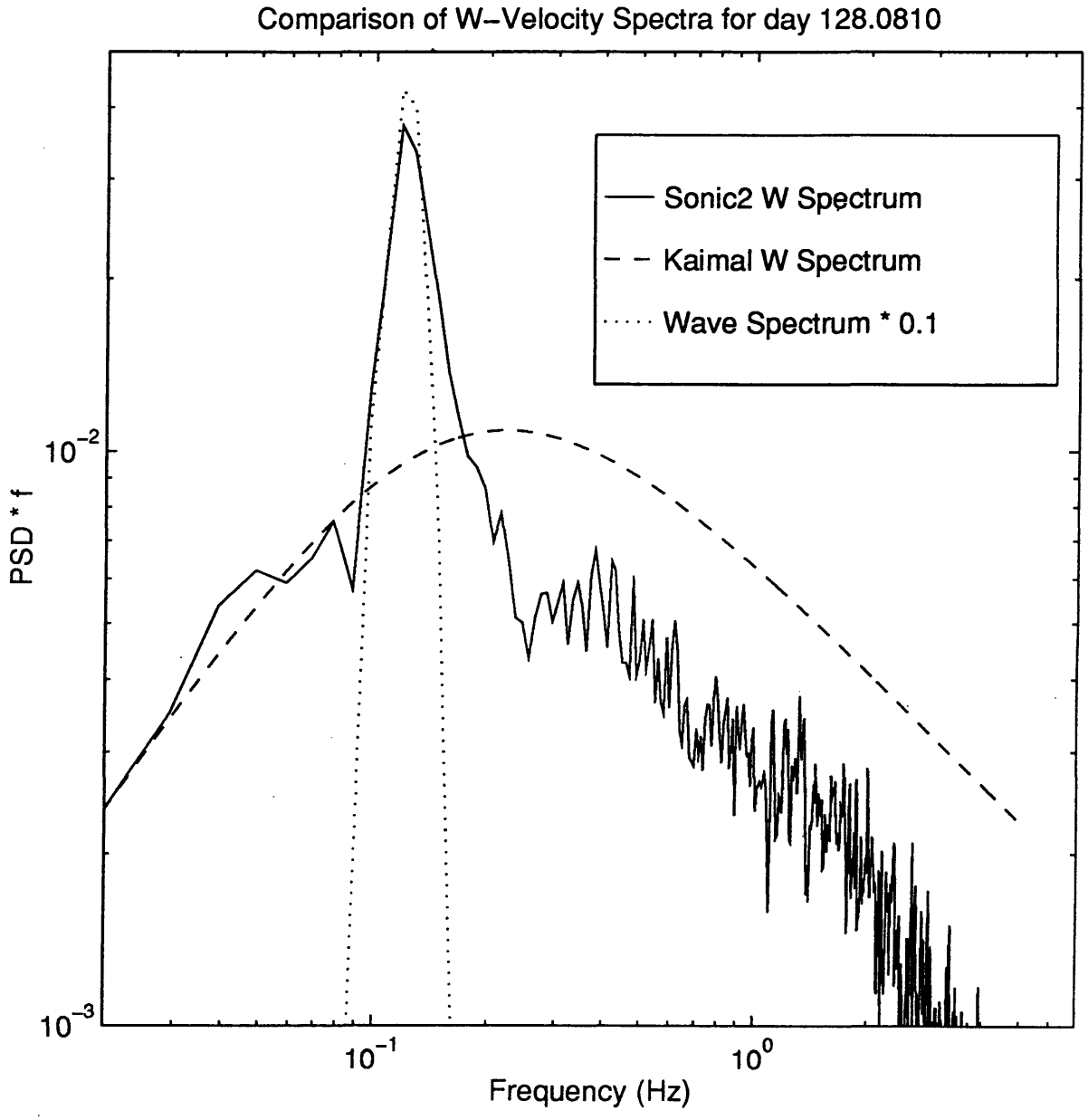

Figure 2.10 Comparison of w-velocity spectrum from the sonic anemometer measurements of this marine boundary layer experiment with the well accepted Kaimal spectrum derived over land (*Kaimal et al.*, 1972). The increase in energy at the wave frequencies (dashed line) indicates a strong correlation between the wind and the waves.

an oscillatory signal, however the absence of a monochromatic wave field in any field study complicates this approach. In this thesis, a technique is introduced to overcome this difficulty. Filtering the wind data with a narrow band-pass filter centered around the dominant wave frequency and choosing only the time periods characterized by the most monochromatic-like waves present, results in a time series suitable for phase averaging. The analysis is then carried a step further and the dependence of wave-induced momentum flux on sea state is investigated by bin averaging profiles of mean wave-induced momentum flux according to wave age c/U_{10}.

3. EXPERIMENT

The data used in this investigation was collected during the Marine Boundary Layer II experiment aboard the R/P FLIP (Floating Instrument Platform), shown in Figure 3.1. The platform is a 110-meter spar buoy owned by the U.S. Navy and operated by the Marine Physical Laboratory at University of California's Scripps Institution of Oceanography (SIO). The R/P FLIP does not have its own propulsion system and is towed in the horizontal position to the experiment site where it 'flips' to the vertical position in about 20 minutes by flooding tanks in the stern section. Once flipped, the platform extends 17 meters above the mean water level. It is designed to be a stable platform once it is vertical in the water and is capable of measuring simultaneous profiles of atmospheric and oceanographic properties.

The experiment was conducted during April-May, 1995, thirty miles west of Monterey, CA. During the first week of the experiment an instrumented mast, 15 meters long, was constructed along the FLIP's port boom. Once completed, the mast was deployed vertically from the end of the 16-meter port boom, extending from roughly 3 to 18 m above the sea surface. This mast held the sonic anemometers, cup anemometers, and wind vanes used for this study. Figure 3.2 shows the orientation of the R/P FLIP with respect to the dominant wind direction, illustrating that flow distortion by the platform is not a concern for this time period.

This study focuses on the last six days of the experiment, Julian days 123-128, a period when all the relevant instruments were functioning properly. During this period, weather conditions were typical of those generally found off the coast of California. A low pressure system which began to set up over California shortly before the first day intensified during the week, resulting in northwest winds of increasing intensity. The mean winds reached velocities of greater than 15 m/s and the waves reached heights of 6 m (Figure 3.3). Near the end of this period, the system began to weaken and the wind speeds decreased without changing direction. These conditions provided a complete range of sea states, from developing to fully developed and then decaying, and established a unique setting for an analysis of the coupling between the wind and the waves.

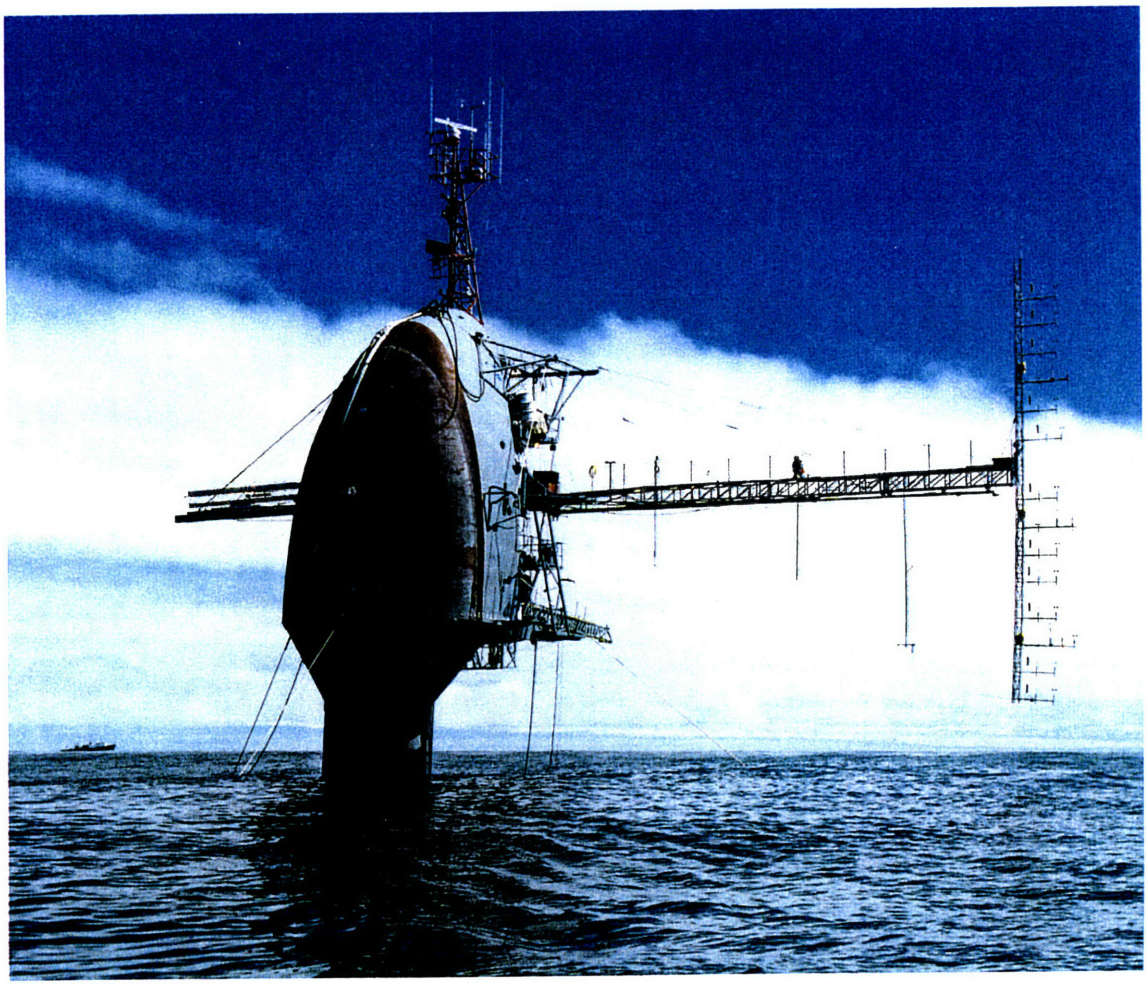

Figure 3.1 The R/P FLIP in the vertical position after deployment of the instrument mast.

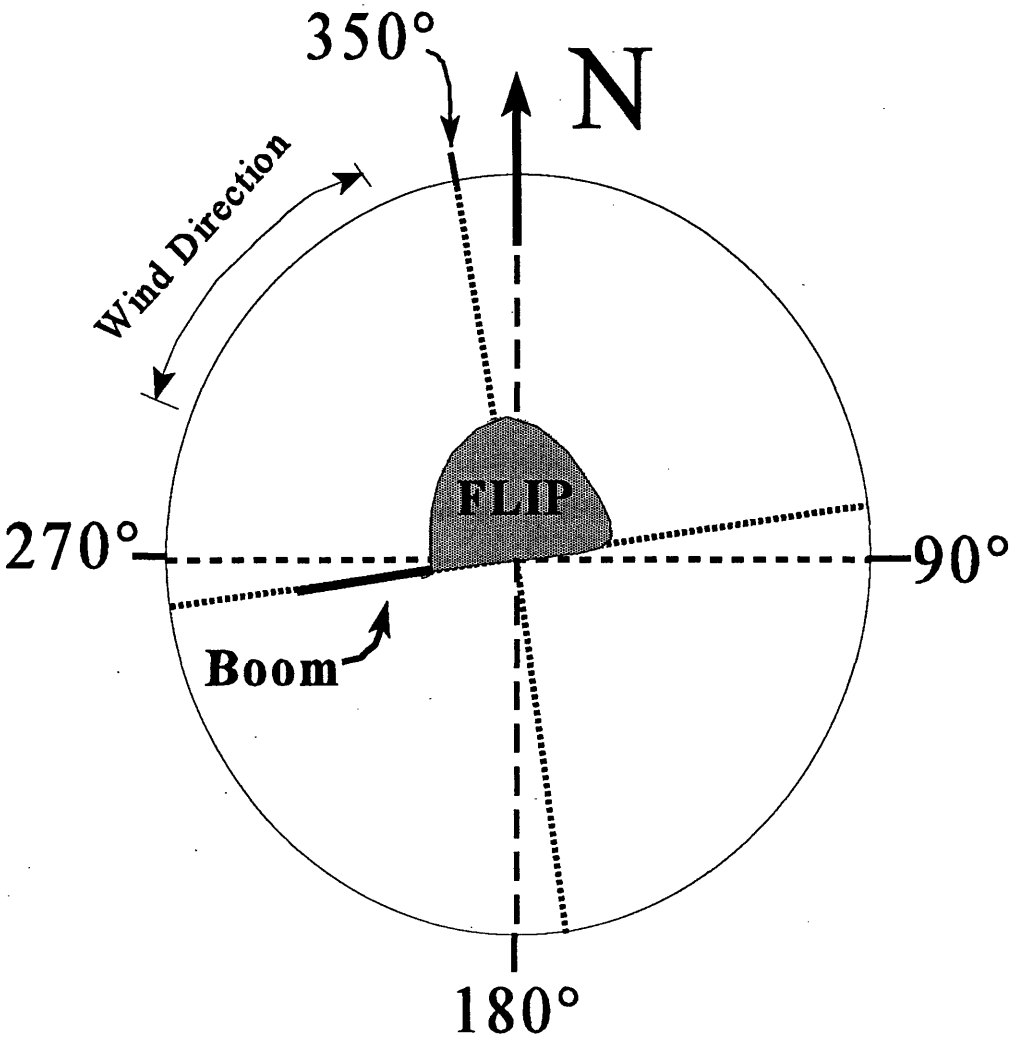

Figure 3.2 Orientation of the FLIP with respect to 0° N. As shown by the range of wind directions during the time period of this study, flow distortion from the FLIP is not a concern.

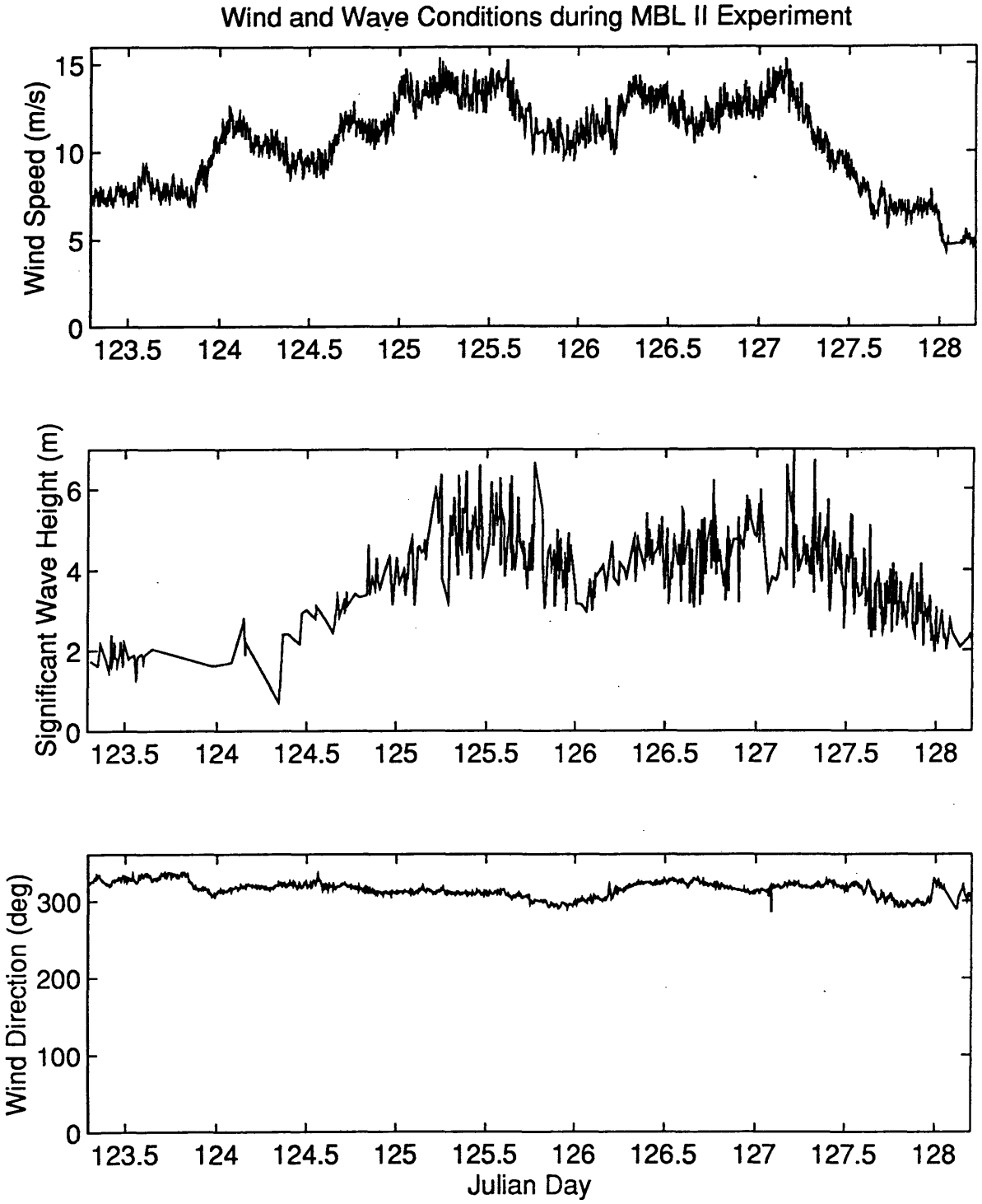

Figure 3.3 Time series of wind speed, significant wave height, and wind direction for the six-day period used in the analysis.

3.1 INSTRUMENTATION

3.1.1 WIND MEASUREMENTS

Wind speed and direction were recorded by sonic anemometers, cup anemometers, and vanes mounted on the FLIP's mast. Figure 3.4 illustrates the experimental setup and identifies the instruments by number where appropriate. The sonic anemometers provided estimates of the mean wind and virtual temperature as well as time series of the turbulent quantities u', v', w', and θ_v'. Four of the five sonic anemometers were located on the mast 4.75 m, 8.7 m, 13.8 m, and 18.12 m above mean sea level. The fifth sonic was hung from the boom, 3.7 m away from the mast and 3.9 m above sea level, to supplement the measurements of the lowest sonic on the mast. The twelve cup anemometers and eleven vanes were fairly evenly spaced between 2.6 - 16.4 m above mean sea level and provided profiles of the mean horizontal wind speed and direction, respectively. The cup anemometer located at the level of the boom (cup 7) was not used for this analysis because of concern for flow distortion. On Julian day 125, the waves damaged the lower two cup anemometers, and after that time the analysis is limited to the upper ten levels.

The cup anemometers, Model 010C Wind Speed Sensors, were manufactured by Met One Instruments. They consist of three rotating cups, coupled to a slotted disc wheel. This wheel rotates and interrupts the light path of an optical link, producing a pulsed frequency output proportional to wind speed. The wind vanes, Model 020C Wind Direction Sensors, were also manufactured by Met One Instruments. These instruments have one airfoil vane coupled to a potentiometer, providing voltages which can be converted to azimuth data.

The sonic anemometers, made by Gill Instruments, provide a three-axis measurement of air velocity and speed of sound. These instruments consist of a sensing head with six ultrasonic transducers arranged in three pairs. The pairs are aligned with a non-orthogonal coordinate system, so the direction and magnitude of the incident air flow can be derived. Each transducer acts as both a transmitter and a receiver, sending and receiving pulses of high frequency sound waves. The times of flight in each direction, $t1$ and $t2$, between a pair of transducers are defined according to:

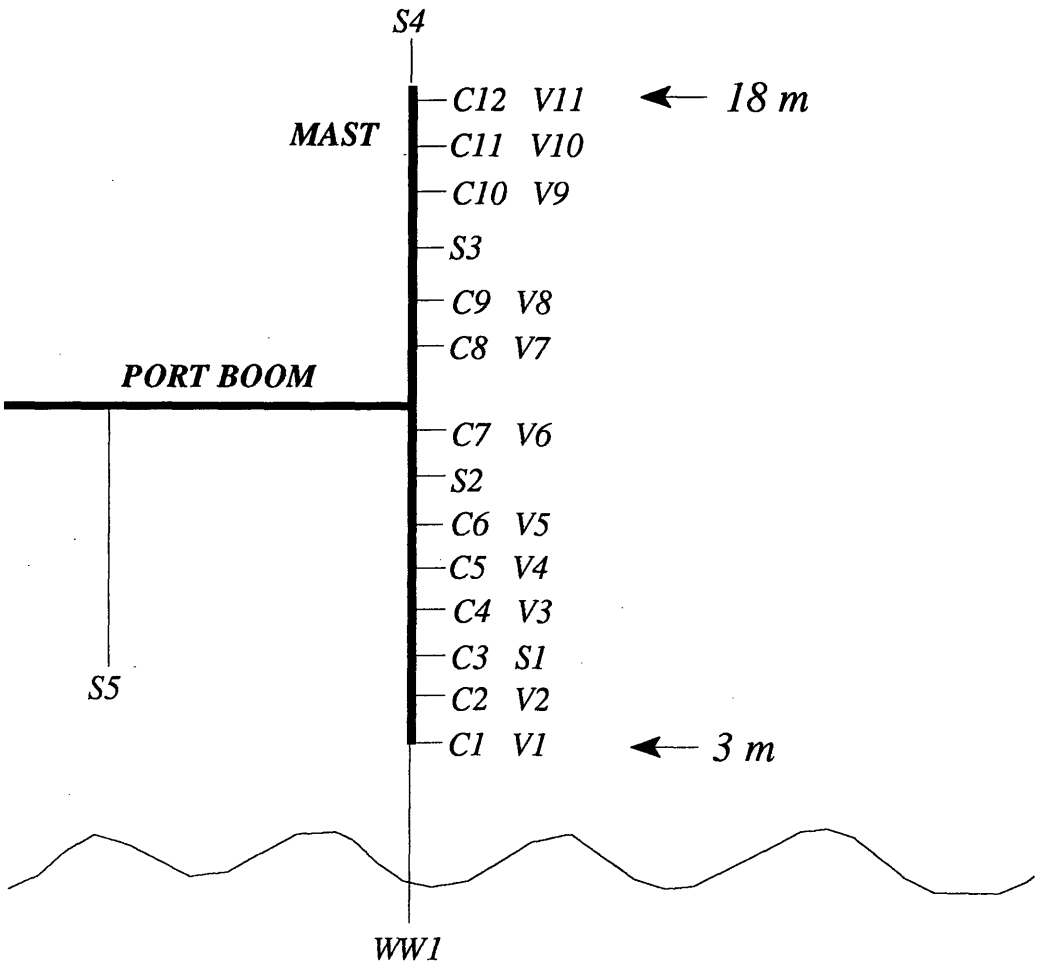

Figure 3.4 Diagram of instrument locations on FLIP's port boom and mast. The instruments are identified by letters (*S* sonic anemometer, *C* cup anemometer, *V* wind vane, *WW* wave wire) and each is assigned a number.

$$t1 = \frac{L}{(c + V)} \qquad t2 = \frac{L}{(c - V)} \tag{3.1}$$

where c is the speed of sound in air, L is the distance between transducers, and V is the air flow parallel to the line of the transducers. Given these flight times, V and c can be computed explicitly:

$$V = \frac{L}{2}\left(\frac{1}{t1} - \frac{1}{t2}\right) \tag{3.2}$$

$$c = \frac{L}{2}\left(\frac{1}{t1} + \frac{1}{t2}\right) \tag{3.3}$$

The speed of sound is then used to compute the virtual temperature. There is a small effect on $t1$ and $t2$ caused by the air flow normal to the line of the transducers which must be accounted for in these temperature calculations. This correction is described in Section 3.2.2. Wind tunnel calibration of the sonic and cup anemometers after the experiment showed good agreement with their factory calibrations.

3.1.2 Wave Height Measurements

Wave heights for this study were measured by a single wave wire, manufactured by SIO, mounted directly beneath the mast. This ensured that all measurements of wind velocity occurred over the same position or phase of the wave as measured by the wave wire. Data from three other wave wires, located halfway out the face boom, could be used in future work for computing directional spectra. These instruments operate on the principles that seawater is a good conductor and that shorter wires have lower resistance. When a wave passes the wire, it decreases the distance between the top of the wire and the surface of the water (which acts as ground), thus lowering the resistance. Measurements of resistance are converted to voltage and logged with the rest of the data.

The wave wires were calibrated by comparing the variance of the wave wire data to the variance of subsurface pressure sensor data collected by Dave Checkley of SIO. The ratio of the variance of the pressure sensor data to that of the wave wires was used to find the

calibration coefficients for each wire. Since the subsurface wave-induced pressure fluctuations beneath the waves decrease with increasing depth, and waves with larger wave numbers are more rapidly attenuated with depth than low frequency waves, the pressure data was first corrected according to the standard procedure presented by *Earle and Bishop* (1984). In this procedure, the corrected wave height spectrum $E(f)$ for wave height is computed from the wave pressure spectrum $E_p(f)$ according to:

$$E(f) = \frac{E_p(f)}{K^2} \tag{3.4}$$

where K is the depth attenuation factor between surface elevation and pressure, defined by:

$$K(f) = \frac{\cosh[k(z + D)]}{\cosh(kD)} \tag{3.5}$$

where k is the wave number, z is the depth of the sensor below the surface (negative downward), and D is the water depth. In the FLIP experiment, conditions were characteristic of deep water waves ($kD > \pi$) and Equation 3.5 simplifies to:

$$K(f) = e^{kz} \tag{3.6}$$

3.2 Data Processing

All data were sampled at 50 Hz and averaged down to 10 Hz for the final analysis. A boxcar averaging window with no overlap between successive windows was used for this conversion. Before the final analysis, a motion and tilt correction algorithm was applied to all the sonic anemometer measurements. This involved removal of the velocity contamination that arises from three sources: (1) instantaneous tilt of the anemometer due to the pitch, roll, and heading variations of the platform; (2) angular velocities at the anemometer due to rotation of the platform about its local coordinate system axes; and (3) translational velocities of the platform with respect to a fixed frame of reference (*Hare et al.*, 1992).

The approach described by Edson et al. (1996) was used to correct this contamination.

Using this approach, the true wind vector (i.e, uncontaminated by motion) can be written

$$\vec{V}_{true} = \boldsymbol{T}(\vec{V}_{obs} + \vec{\Omega}_{obs} \times \vec{R}) + \vec{V}_{mot} \tag{3.7}$$

where $\vec{V}_{true}$ is the desired wind velocity vector in the reference coordinate system; $\vec{V}_{obs}$ and $\vec{\Omega}_{obs}$ are the measured wind and platform angular velocity vectors in the platform frame of reference, respectively; T is the coordinate transformation matrix from the platform frame coordinate system to the reference coordinates; $\vec{R}$ is the position vector of the wind sensor with respect to the motion package; and $\vec{V}_{mot}$ is the translational velocity vector measured at the location of the motion package. The transformation matrix is used to transform the tilted measurements back to the fixed frame, and requires estimates of the roll, ϕ, pitch, θ, and yaw, Ψ. The $\vec{\Omega}_{obs} \times \vec{R}$ term corrects for the angular velocities that arise due to the time rate of change of this rotation.

A Systron-Donner MotionPAK was strapped down to the mast just above the walkway on the port boom. The MotionPAK provided measurements of the angular velocity vector, $\vec{\Omega}_{obs}$, and acceleration vector, $\vec{\ddot{x}}_{ob.}$. In a strapped-down system, the measured accelerometer output is a combination of the gravitational component due to the pitching and rolling of the platform plus the accelerations arising from the motion of the platform along the accelerometer axes. This tilt-induced contamination can be used to our advantages through complementary filtering, which combines the low-passed accelerations and heading with the high-passed integrated angular rates to compute the desired angles (*Edson et al.*, 1996). The angles were then used in the coordinate transformation matrix given by

$$\boldsymbol{T} = \begin{bmatrix} \cos(\Psi)\cos(\theta) & \sin(\Psi)\cos(\phi)+\cos(\Psi)\sin(\theta)\sin(\phi) & -\sin(\Psi)\sin(\phi)+\cos(\Psi)\sin(\theta)\cos(\phi) \\ -\sin(\Psi)\cos(\theta) & \cos(\Psi)\cos(\phi)-\sin(\Psi)\sin(\theta)\sin(\phi) & -\sin(\theta)\cos(\phi)\sin(\Psi)-\sin(\phi)\cos(\Psi) \\ -\sin(\theta) & \cos(\theta)\sin(\phi) & \cos(\theta)\cos(\phi) \end{bmatrix} \tag{3.8}$$

where the sign convention here is based on a right-handed (x,y,z) coordinate system with x positive forward (to bow/keel), y positive to port, z positive upward, Ψ positive for the platform's bow yawed clockwise from north, ϕ positive for the port side rolled up, and θ positive for the bow pitched down. Note that ϕ and θ are right-handed rotations but to

conform to the normal convention for heading, we have used a left-handed definition for Ψ. This definition allows us to directly use the FLIP's compass in the transformation matrix.

Because the R/P FLIP used a three point mooring to keep it from drifting, the mean translational velocities relative to earth are zero and the fluctuating component was computed by integration of the accelerometer measurements. This involved rotation of the measured accelerations into the vertical using the transformation matrix. The gravity vector was then added to the rotated accelerations to remove the tilt-induced component and leave behind the motion-induced accelerations. The resulting accelerations were then high-pass filtered to remove any drift before integrating. This process can be summarized by the following expression:

$$\vec{V}(t)_{mot} = \int [Hp(T\,\vec{\ddot{x}}(t)_{obs} + \vec{g})]\,dt \tag{3.9}$$

where Hp represents a high-pass filter operator, and $\vec{g} = (0,0,-g)$. This high-passed component represents the wave-induced motions of the platform where we use a time constant of 2 minutes for the filter.

The angular velocity was then computed using the position vector for each sonic, and the resulting velocities were added to the observed measurements to compute the true velocities given by Equation 3.7. The resulting time series of wave height and wind speed measurements were used for this study of the influence of waves on momentum flux. Some additional parameters were required for this analysis, and the computation procedures for them are outlined below.

3.2.1 Wave Phase Speed and Wave Number

Wave phase speed is defined as $c = \omega/k$, where ω is radian frequency. Wave number is defined as $k = 2\pi/\lambda$, where λ is the wavelength. The dispersion equation relates radian frequency to wave number:

$$\omega^2 = gk\tanh(kD) \tag{3.10}$$

For deep water waves ($kD > \pi$), Equation 3.10 simplifies to

$$k = \frac{\omega^2}{g} \tag{3.11}$$

It follows that wave phase speed for deep water waves is

$$c = \frac{g}{\omega} \tag{3.12}$$

To compute phase speed and wave number from the FLIP data, the spectrum of 5 minutes of wave height data was computed and the dominant wind-driven wave frequency f was chosen as that corresponding to the highest point on the spectrum. Radian frequency was then computed from the definition:

$$\omega = 2\pi / f \tag{3.13}$$

3.2.2 Air Temperature

Using the sonic anemometer measurements for the speed of sound c, temperature T_v is calculated according to (*Fairall et al.*, 1996b):

$$T_v = \frac{c^2 + u_N^2}{403} \tag{3.14}$$

where

$$u_N^2 = v^2 + \frac{1}{2}(u + w)^2 \tag{3.15}$$

is a correction for curvature in the path the sound waves travel from one receiver to the other. This is converted to potential temperature according to:

$$\theta_v = T_v + \Gamma_v z \tag{3.16}$$

using the adiabatic lapse rate $\Gamma_v = 9.8\ ^\circ/km$. Mean potential temperature $\overline{\theta}_v$ is computed by averaging 15-minutes of data.

3.2.3 FLUXES

Using sonic anemometer data, the fluctuations about the mean of the velocity and virtual potential temperature were computed according to the following decomposition:

$$\begin{aligned} u'(t) &= u(t) - \bar{u} \\ v'(t) &= v(t) - \bar{v} \\ w'(t) &= w(t) - \bar{w} \\ \theta_v'(t) &= \theta_v(t) - \bar{\theta}_v \end{aligned} \tag{3.17}$$

It is important to note that these primed variables represent the net fluctuations about the mean, including contributions due to turbulent and wave-induced effects. Thus, calculations of momentum flux from these sonic anemometer measurements represents the total flux (see Equation 2.13).

The desired covariances were calculated by multiplying the vertical velocity fluctuation with u', v', and θ_v' and averaging over 15 minutes for each sonic. Using these covariances, the friction velocity u_* and the virtual temperature scaling parameter θ_{v*} were estimated from

$$u_* = [\,(\overline{u'w'})^2 + (\overline{v'w'})^2\,]^{\frac{1}{4}} \tag{3.18}$$

$$\theta_{v*} = -\frac{\overline{\theta' w'}}{u_*} \tag{3.19}$$

Additionally, another value for u_* was computed using the profile method. This method uses the equation for a logarithmic wind profile corrected for stability derived over land:

$$u_H(z) - u_H(z_o) = \frac{u_*}{\kappa}\,[\,\ln(\frac{z}{z_o}) - \psi_m(\zeta)] \tag{3.20}$$

where $u_H(z)$ is the horizontal wind velocity at height z and $\psi_m(\zeta)$ is the integrated wind shear function:

$$\psi_m(\zeta) = \int [\,1 - \phi_m(\zeta)]\,\frac{\partial \zeta}{\zeta} \tag{3.21}$$

The most commonly used form of this function is found by integrating the Businger-Dyer expressions for ϕ_m (see Section 2.1.3, Equation 2.9). For unstable and stable conditions, respectively, these expressions are (*Paulson*, 1970)

$$\psi_m(\zeta) = \ln\left[\left(\frac{1 + x(\zeta)^2}{2}\right)\left(\frac{1 + x(\zeta)}{2}\right)^2\right] - 2\tan^{-1}x(\zeta) + \frac{\pi}{2} \qquad \zeta < 0$$

$$\psi_m(\zeta) = -5\zeta \qquad \zeta \geq 0 \tag{3.22}$$

where

$$x(\zeta) = (1 - 16\zeta)^{1/4} \tag{3.23}$$

By rearranging Equation 3.20 and assuming $u_H(z_o) = 0$ (surface currents will be incorporated into the analysis when they become available), the equation for the wind profile becomes:

$$\ln(z) - \psi_m(\zeta) = \frac{\kappa}{u_*} u_H(z) + \ln(z_o) \tag{3.24}$$

It follows that the slope of a line fit to a plot of $\ln(z) - \psi_m(\zeta)$ vs. $u_H(z)$ is equal to κ / u_*, and the y-intercept is equal to $\ln(z_o)$. The friction velocity and roughness lengths are then calculated from these quantities. Since the profile method of computing friction velocity is derived from semi-empirical expressions validated over land, and assumes a constant flux layer this quantity provides an interesting comparison with direct measurements of friction velocity over the ocean. This is discussed further in Section 5.1.3.

4. ANALYSIS

The objective of this analysis is to: 1) identify the periods when the wind-driven wave field has a clearly defined spectral peak, 2) quantify the influence of this wave field on the overlying winds, and 3) then derive the wave-induced momentum flux from this information. The following velocity decomposition is adopted:

$$u = \bar{u} + \tilde{u} + u' \tag{4.1}$$

where the prime now represents the turbulent fluctuations, the overbar denotes a time average:

$$\bar{u} = \lim_{T\to\infty} \frac{1}{T} \int_0^T u(t)\, dt \tag{4.2}$$

and tilde represents the wave-induced component, defined with the use of the phase-averaging operator (*Finnegan et al.*, 1984):

$$\langle u \rangle = \bar{u} + \tilde{u}(t) = \lim_{N\to\infty} \frac{1}{N} \sum_{n=1}^{N} u(t+n\tau) \tag{4.3}$$

$$\tilde{u} = \langle u \rangle - \bar{u} \tag{4.4}$$

where τ is the period of the organized oscillation, and N represents the number of consecutive wavelengths averaged together to get one phase-averaged wave.

The phase averaging operator can be regarded as the equivalent of a time average for a periodic signal, for which the conventional time average would equal zero. Instead of averaging all data points together for a given averaging time, a phase average averages N successive frames of data together, with τ determining the length of each frame. This operation can be thought of as stacking the N frames on top of one another and averaging down through the stack all the points having the same phase. This preserves the wave-like behavior of a periodic function. Note that there are two time scales in this operation; τ is the

period of organized oscillation present in the signal, and $N \cdot \tau$ is equal to the averaging time. For example, an averaging time of 1 minute and a wave period of 6 seconds corresponds to averaging 10 frames together (i.e. N = 10 in equation 4.3), with each frame being one wavelength long.

Turbulence by definition is a random process, so both the time average and the phase averaging operators will remove the turbulent components of the signal at all frequencies, provided the averaging time is long enough. This attribute is essential to an investigation of the influence of organized waves on the overlying wind field, since this requires isolating the wave-induced signal from the turbulence. For this application, the period of oscillation (τ in the definition of phase averaging, Equation 4.3) is equal to the period of the dominant waves, and the averaging time ($N \cdot \tau$) must be long enough to remove most of the turbulent components from the atmospheric flow. This period and time are then used to phase average the wind field at various heights, resulting in a 2-D field of the wave-induced horizontal and vertical wind velocities $\tilde{u}$ and $\tilde{w}$. The product of these quantities integrated in space along the entire wave (or equivalently, over all phases in time), $\overline{\tilde{u}\tilde{w}}$, is defined as the wave-induced momentum flux.

4.1 Applying the Phase Averaging Technique to Open Ocean Conditions

Finnegan et al. (1984) used a phase averaging technique to remove the turbulent components from an atmospheric boundary layer perturbed by Kelvin-Helmholtz internal waves. In their study, wave frequency remained constant for many cycles, a feature which is fundamental to the use of the phase averaging operator for separating the periodic and turbulent components. For open ocean conditions such as those characteristic of the FLIP experiment, it is unreasonable to assume a monochromatic wave field, i.e., a wave field with constant phase. The unsteady ocean surface is continually changing as the wind forcing varies in magnitude and direction and wave-wave interaction moves energy between the spectrum of wavelengths. Additionally, swell propagating in from other regions influences the frequency of the dominant wave and contributes to the formation of a non-monochromatic wave field.

For such a time series with a variable frequency, the definition of phase averaging cannot be applied in the limit as N approaches infinity. Instead, the number of cycles included in the phase average must be reduced until the phase variation of the dominant wave is negligible, while still ensuring that the averaging time is long enough for the turbulent components to average to zero. To accomplish this, the signal (fluctuations cause by the dominant waves) to noise (turbulence plus phase variability) ratio of the atmospheric fluctuations must be maximized. The approach taken in this thesis involves choosing only the time periods with the most monochromatic-like wave fields and applying a narrow band-pass filter centered around the dominant wave frequency to the overlying winds. By choosing only the time periods with the most well-defined wave-induced fluctuations, the amount of phase variation caused by interaction among waves of different frequencies is reduced. By removing most of the turbulent components before averaging, shorter averaging times can be used to accommodate the remaining phase variations.

4.2 Choosing the Most Monochromatic Wave Fields

The effect of frequency modulation on phase averaging is demonstrated in Figure 4.1. The dotted line in this figure displays a sinusoid whose amplitude matches that of the original wave. Variations in the frequency of the spectral peak result in ambiguity as to the we are along the phase of the wave at a given time. As a result, the amplitude of the phase-averaged wave is significantly decreased from the original signal. To address this problem, the study must be limited to the most well-defined wave-induced fluctuations in order to reduce the amount of phase variation caused by wave-wave interactions. That is, only the time periods with the most monochromatic-like wave fields that one can expect to find in the open ocean are used for the analysis. These time periods are characterized by wave spectra with a single, well-defined peak which is easily distinguished from the swell and other frequency contributions.

Figures 4.2-4.5 illustrate the effect of frequency modulation of the dominant, or most energetic, wave component on phase averaging using the actual open ocean FLIP data. These figures stress the importance of choosing only these monochromatic-like wave fields for the

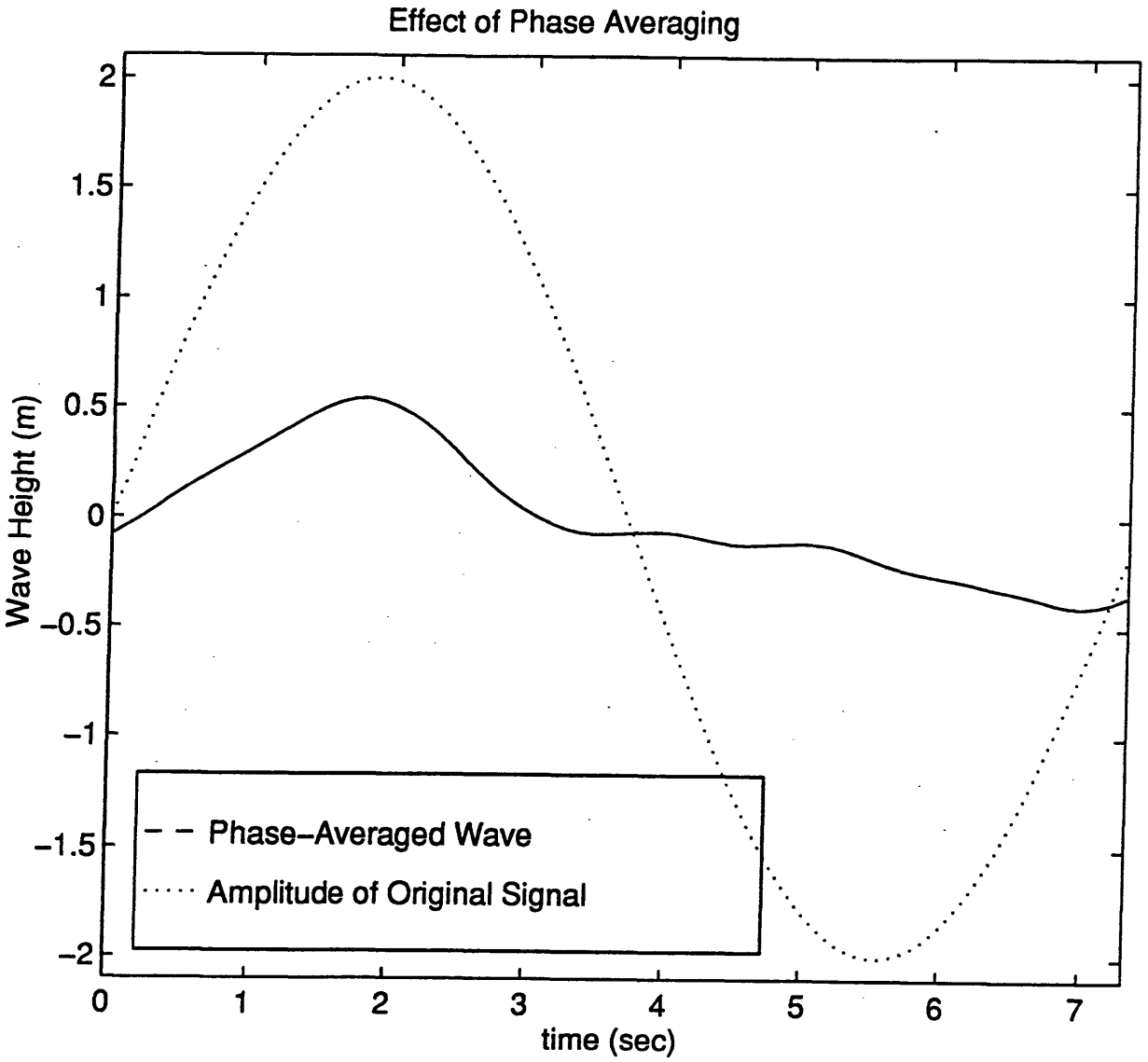

Figure 4.1 Illustration of the effect of frequency modulation of the dominant wave on phase averaging. The dotted line is a sinusoid whose amplitude approximately matches that of the original wave.

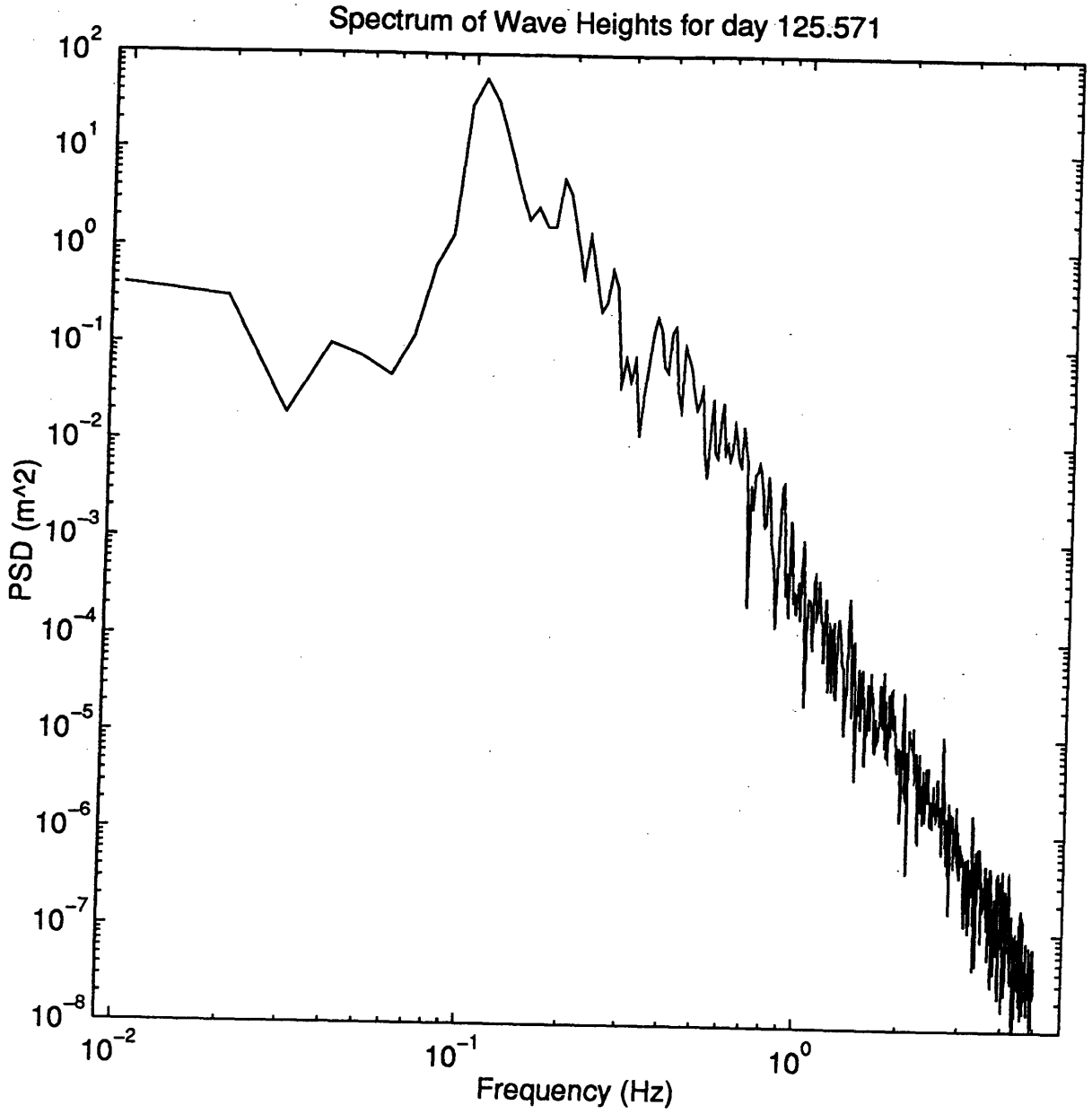

Figure 4.2 Unfiltered spectrum of wave heights with a narrow, well-defined spectral peak.

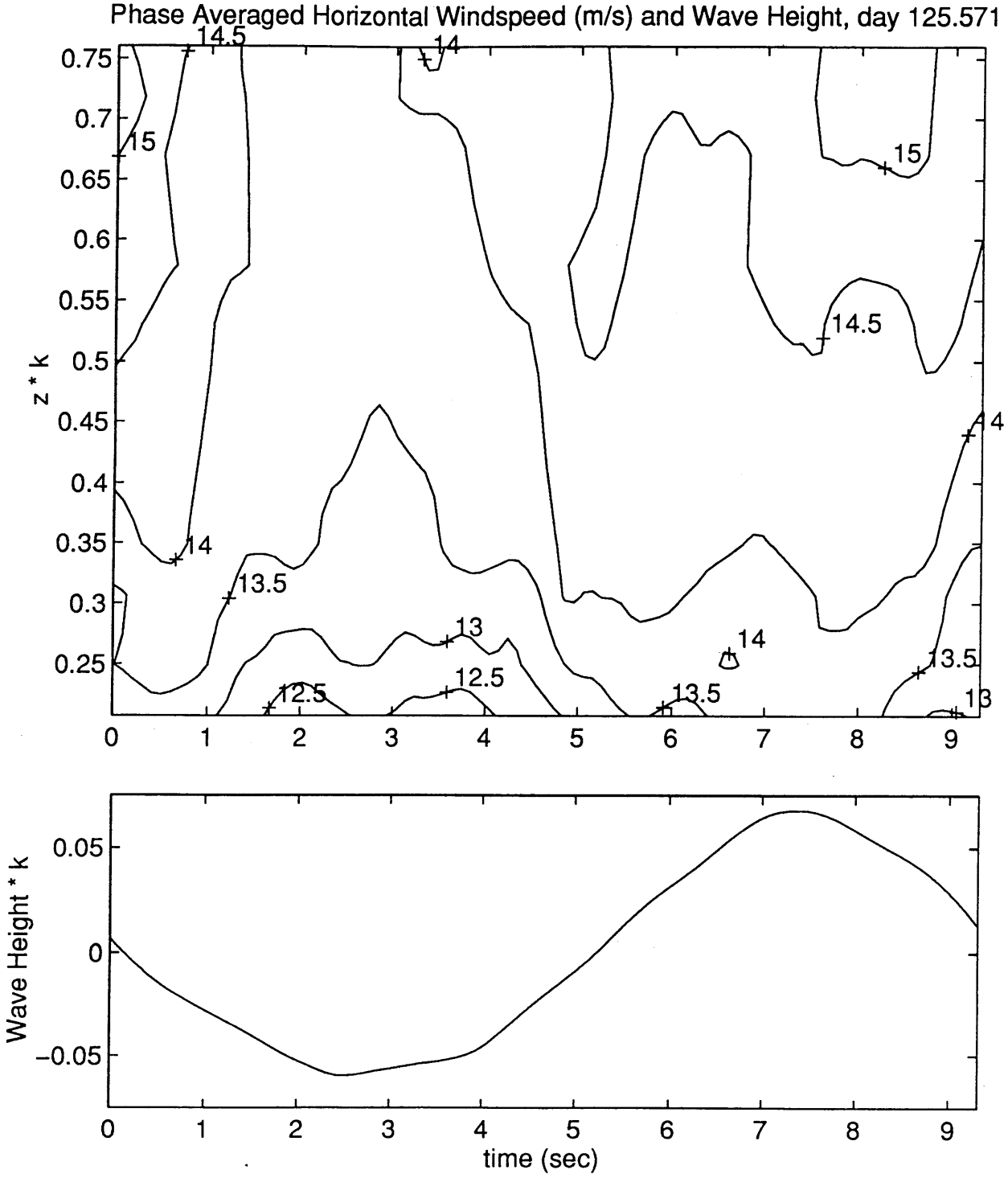

Figure 4.3 Contours of constant phase-averaged wind velocity (top), overlying the wave field of Figure 4.2. The corresponding phase-averaged wave (bottom) closely resembles a monochromatic wave, with minimal attenuation of the original amplitude ($k*amplitude \approx 0.07$). There is a notable wave-induced structure to the overlying atmospheric wind velocities.

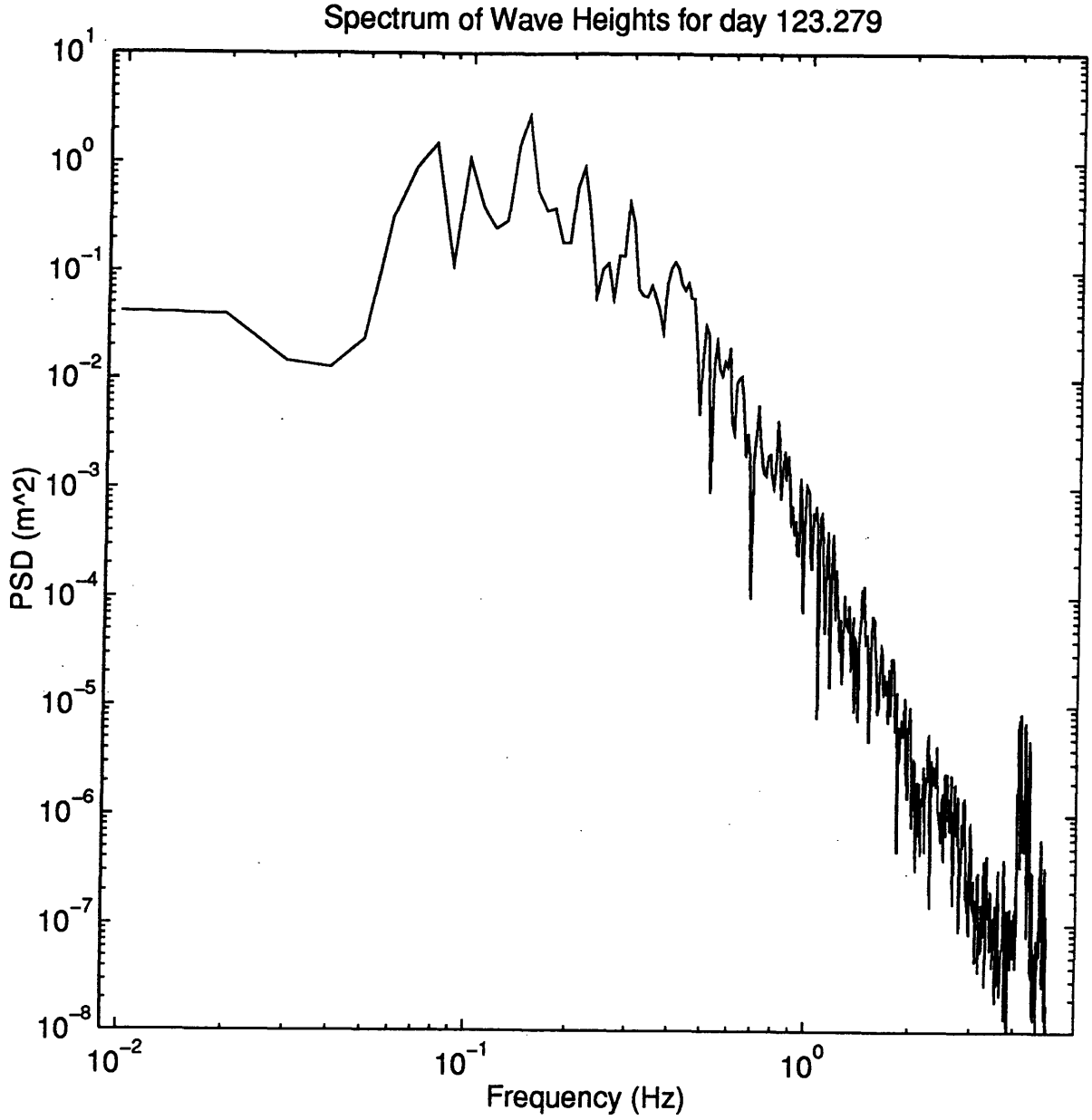

Figure 4.4 Unfiltered spectrum of wave height without a well-defined spectral peak. Significant energy is present at a wide range of frequencies that is not easily distinguished from the energy at the dominant wave frequency.

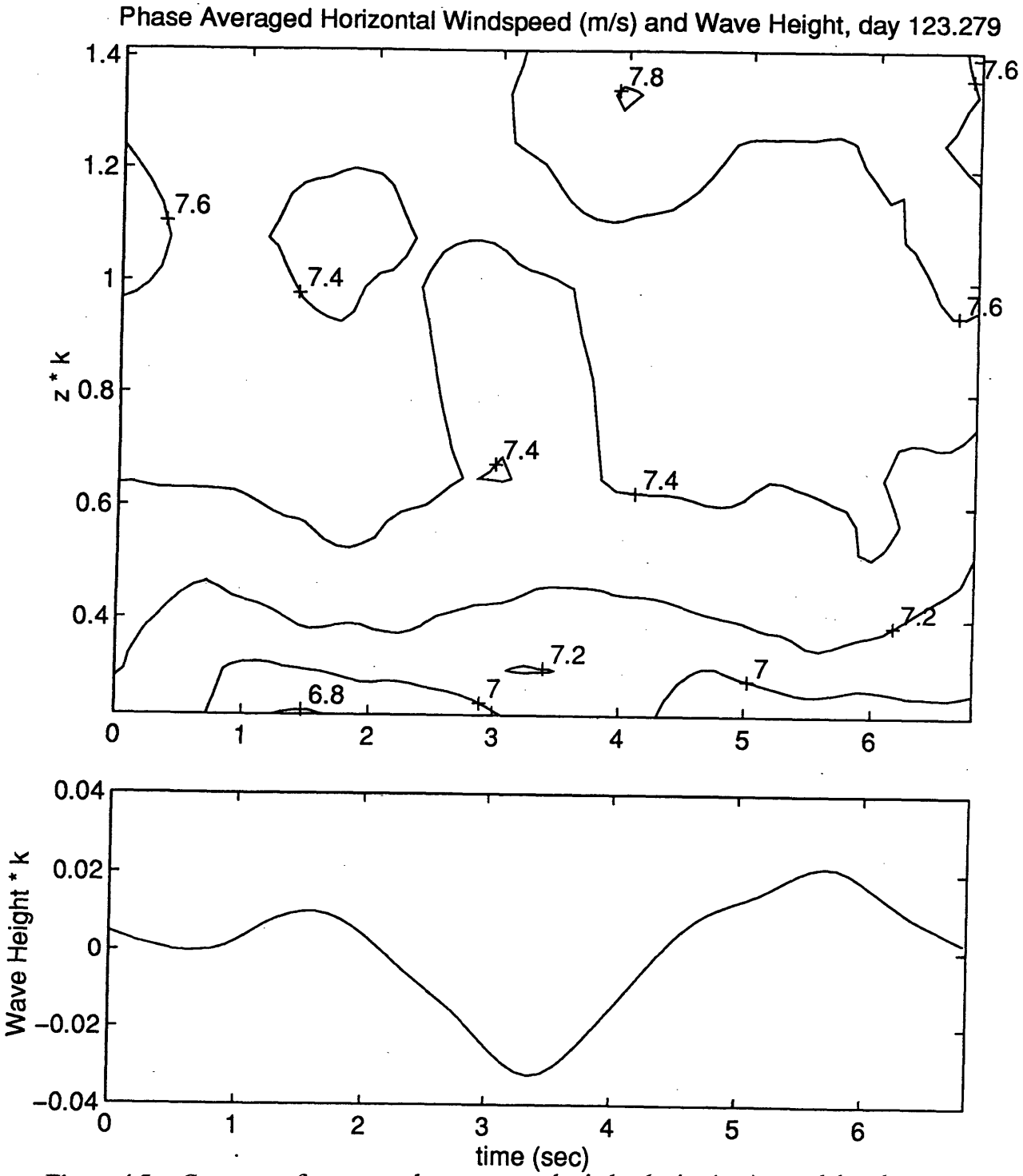

Figure 4.5 Contours of constant phase-averaged wind velocity (top), overlying the wave field of Figure 4.4. The amplitude of the corresponding phase-averaged wave (bottom) was noticeably attenuated from that of the original signal ($k*amplitude \approx 0.04$) due to the presence of energy at a wide range of frequencies in the wave field. There is no considerable wave-induced structure to the overlying wind velocities.

analysis. Figure 4.2 shows the spectrum for a 5-minute time series of wave heights, and the phase-averaged wave from 1 minute of this time series is shown in Figure 4.3. The basis of the decision to average for 1 minute is discussed later in this Section. These figures show that the spectrum has a narrow, well-defined spectral peak and the corresponding phase-averaged wave closely resembles a monochromatic wave. A comparison of the amplitude (normalized by wave number) of the phase-averaged wave in Figure 4.3 with the original value of approximately 0.07, reveals that the amplitude of the phase-averaged wave is not appreciably attenuated from the original signal. The contour plot (illustrating lines of constant velocity) of the overlying phase-averaged winds also shown in Figure 4.3 indicates that there is a coherent structure to these winds that appears to be well-correlated to the phase-averaged wave. In this example, the contours of constant velocity are appreciably elevated over the trough, corresponding to lower wind speeds than at the same elevation over the crest.

On the other hand, Figures 4.4 and 4.5 illustrate a case where this phase averaging procedure is less appropriate. The spectrum shows significant energy present at a wide range of frequencies that is not easily distinguished from the energy at the dominant wave frequency. The result of phase averaging 1 minute of this time series (Figure 4.5) is a highly non-monochromatic waveform with a relatively small amplitude compared to the amplitude of the original signal ($k * amplitude \approx 0.04$). The phase-averaged overlying winds show far less coherent wave-induced structure than do those in Figure 4.4. Thus, this wave field is too disperse for the phase averaging approach to be an effective means of isolating the wave-induced fluctuations.

The question remains of how to choose those spectra which are best suited to this analysis. Owing to the amount of data that must be processed for the statistical analysis, it is impractical to go through the data and pick them out one by one. This investigation found that an effective quantitative way to choose the sections of data which best mimic a monochromatic wave is to compute the ratio of the variance of band-pass filtered wave data to the variance of the unfiltered wave data. In this procedure, filtered and unfiltered wave spectra from each 5-minute record are computed. The analysis then proceeds with only those spectra that have variance ratios greater than 0.7. This variance ratio criteria thereby selects

time periods where the band pass filtered data explains 70% or more of the wave variance. Experience has shown that such wave fields adequately mimic the characteristics of a monochromatic wave field, enabling the use of the phase-averaging technique over the open ocean.

To compute the filtered wave data for the variance ratio, a narrow band-pass filter is applied to the time series. The pass-band of this filter is centered around the dominant, wind-induced wave frequency. Figure 4.6 shows the magnitude and phase of a second-order Butterworth filter typical of the those used in this analysis. To eliminate the nonlinear phase distortion inherent in an Infinite Impulse Response filter such as the Butterworth filter, a zero-phase filtering technique is applied, using MATLAB®'s *filtfilt* function (*Krauss et al.*, 1994). Figure 4.7 shows power spectral density plots, for a 5-minute time series of filtered and unfiltered wave heights. These spectra are the result of averaging together the results of three consecutive 1024-point fast Fourier transforms (after multiplying each by its complex conjugate). In the unfiltered spectrum, the low frequency swell contribution is readily apparent, as well as the wind-driven wave peak and contributions at other frequencies.

Even for the time periods selected by the variance ratio criteria, the averaging time of this analysis is still limited because even the most monochromatic-like open ocean waves are not truly monochromatic. Using a section of data with a well-defined peak in the wave spectrum, Figure 4.8 shows that the amplitude of a phase-averaged wave is still considerably attenuated from the original 1.6 m amplitude for longer averaging times, implying that frequency modulation cannot be neglected in this study for averaging times less than or equal to 1 minute. In the next section, the question of whether 1 minute is a long enough averaging time to remove the atmospheric turbulence is addressed.

4.3 Removing the Turbulence from the Air Flow

The problems associated with using a finite averaging time to remove the turbulent component of atmospheric turbulence are difficult to demonstrate with actual data, mainly because it would require knowledge of the wave-induced components beforehand. However, this problem can be addressed by simulating a turbulent flow field over a wavy surface as in

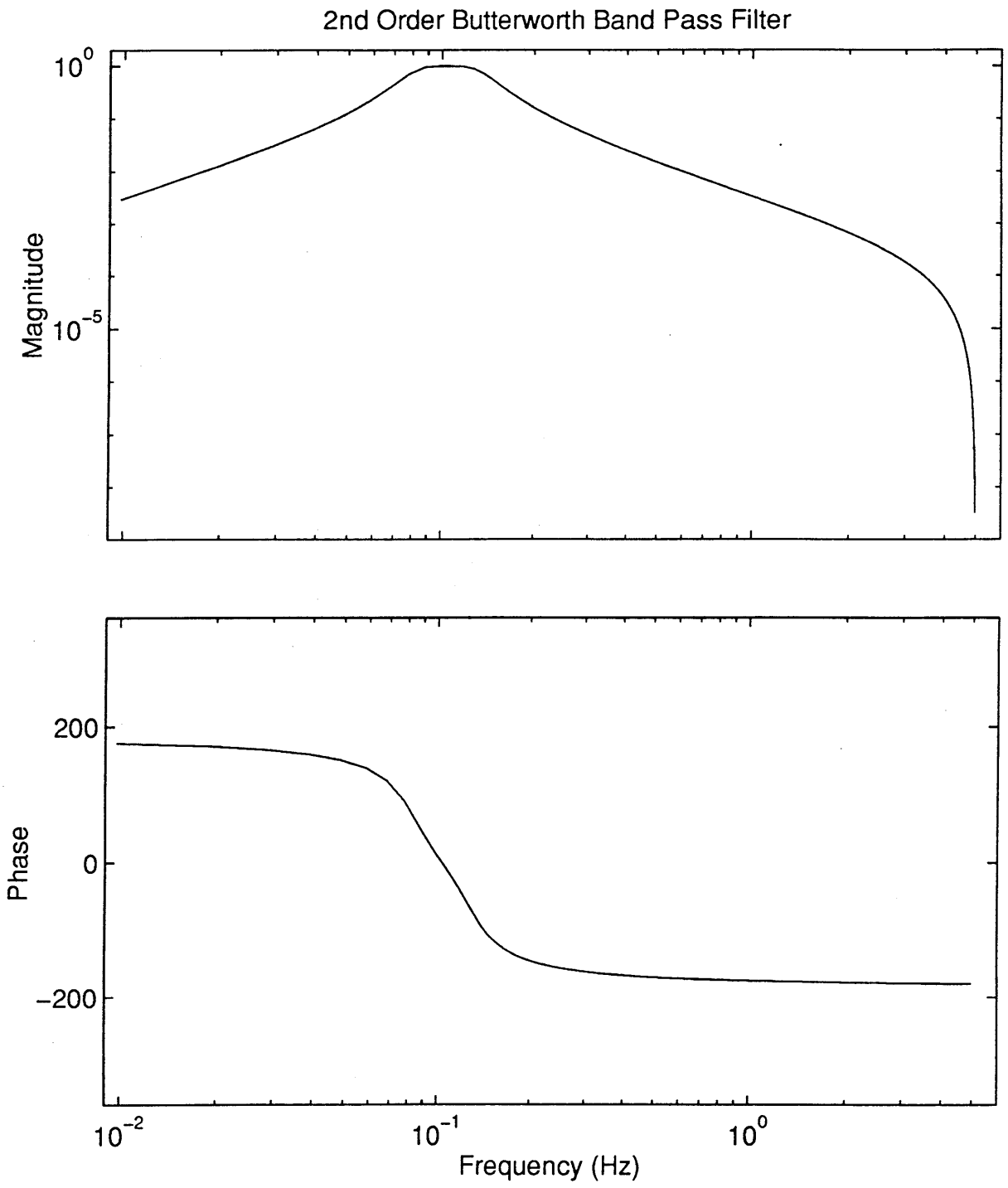

Figure 4.6 Illustration of the shape and phase of a 2nd order band-pass Butterworth filter, typical of those used in the analysis. The band-pass region is centered around the dominant wave frequency.

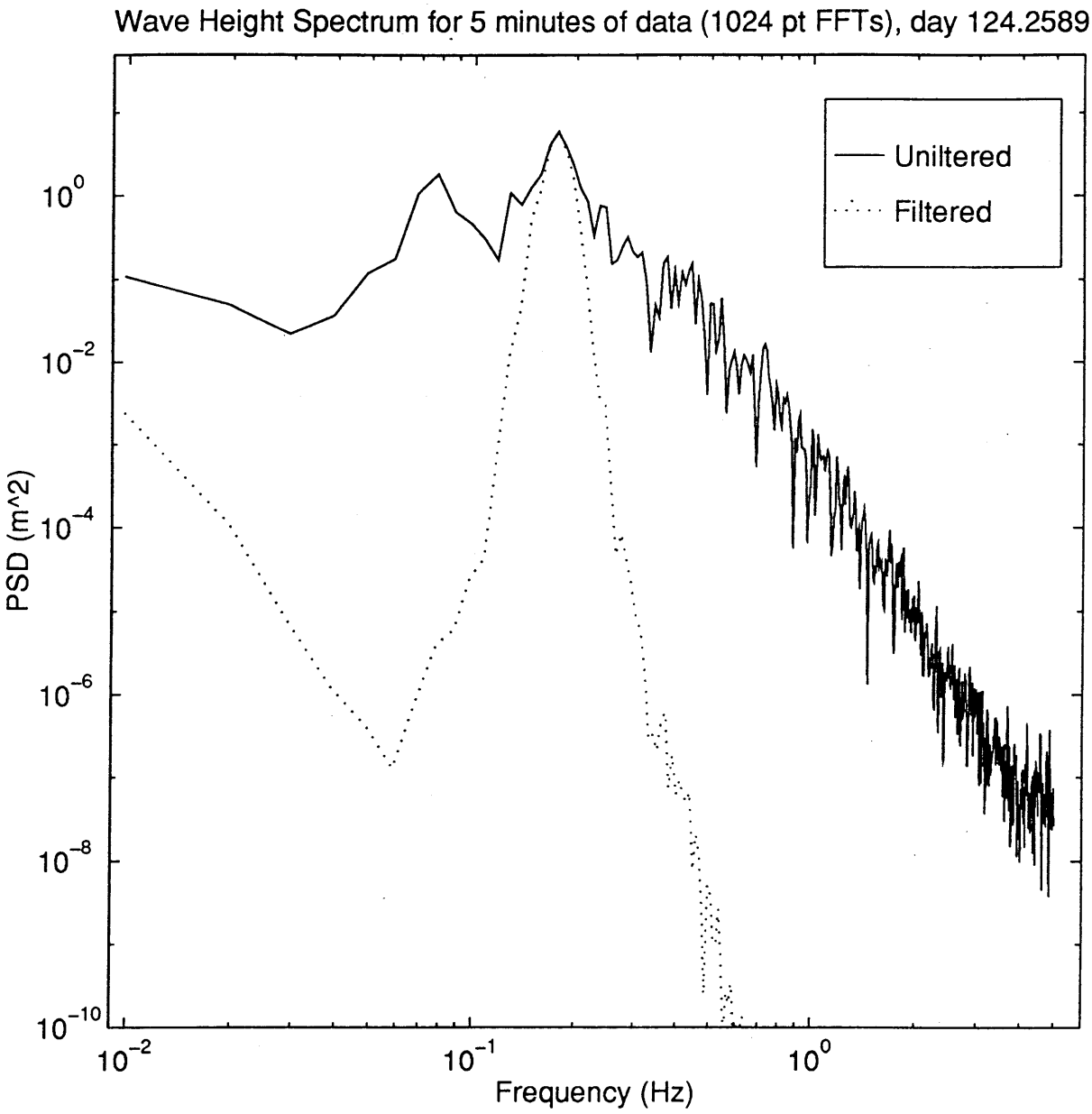

Figure 4.7 Filtered and unfiltered wave height spectra, illustrating the effectiveness of the filter in isolating the signal at the dominant wave frequency.

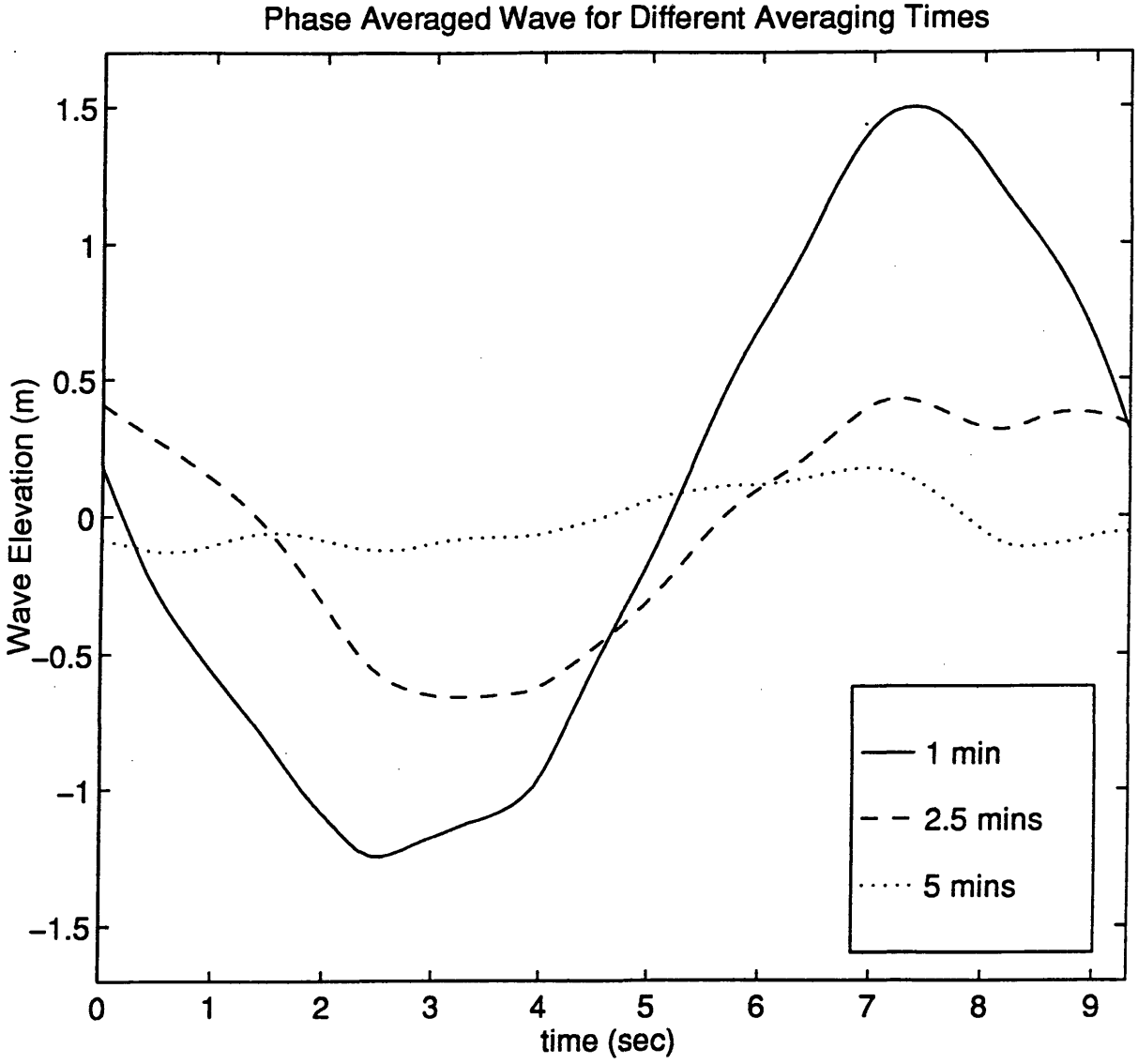

Figure 4.8 Illustration of the effect of different averaging times on the amplitude of the phase-averaged wave, for a time period characterized by a monochromatic-like wave field. This shows that averaging time greater than 1 minute are still too long to consider the wave period a constant.

Andreas et al. (1995). The simulation consists of a potential flow velocity field over fully developed waves. A turbulent component is added to the wave-induced atmospheric fluctuations using the spectral intensity of the horizontal components modeled after the Kaimal u-velocity spectra (*Kaimal et. al.*, 1972). This is linked to the vertical component of turbulence by ensuring that the cospectral phase and amplitude matches that predicted by Kaimal. The resulting atmospheric flow field is then phase averaged over the period of the underlying waves to remove the turbulence, and the momentum flux profile is computed by averaging the product of the horizontal and vertical velocities over the wave period. Since the waves are fully developed and the atmospheric response purely irrotational, potential flow theory predicts that the wave-induced component of this flux is identically zero, and phase averaging without the turbulence has shown this to be true. Thus, the phase-averaged momentum flux is composed entirely of turbulence and it is expected that this contribution will approach zero as the averaging time is increased. Figure 4.9 shows $\overline{uw}/u_{*_T}^2$ vs. averaging time, where $\overline{uw}/u_{*_T}^2$ represents the turbulent fraction of total flux remaining after averaging, since the wave-induced contribution to the flux is exactly zero. These results indicate that averaging for 1 minute only reduces the turbulent fraction of total momentum flux by 10%, which is not sufficient for this analysis as shown in the Appendix.

This problem is addresses by band-pass filtering the velocities prior to beginning the phase averaging procedure, which removes most of the atmospheric fluctuations that are not induced by the dominant waves. The same filter designed for the simultaneous time series of wave heights (Section 4.2) is applied to the horizontal and vertical velocity measurements. The spectra in Figure 4.10 illustrate the use of the filter as a first step in isolating the wave-induced components of the atmospheric fluctuations.

The effectiveness of this procedure is demonstrated by using the filtered time series in the simulation of turbulent reduction by phase averaging described above. Figure 4.11 shows the results from this simulation for both the filtered and unfiltered data. A one-minute averaging time now corresponds to a 1.5% reduction in the turbulent fraction of total momentum flux at all frequencies as a result of both filtering and phase averaging. It will be shown in Chapter 5 that the remaining turbulence is insignificant to the results and conclusions. As a further

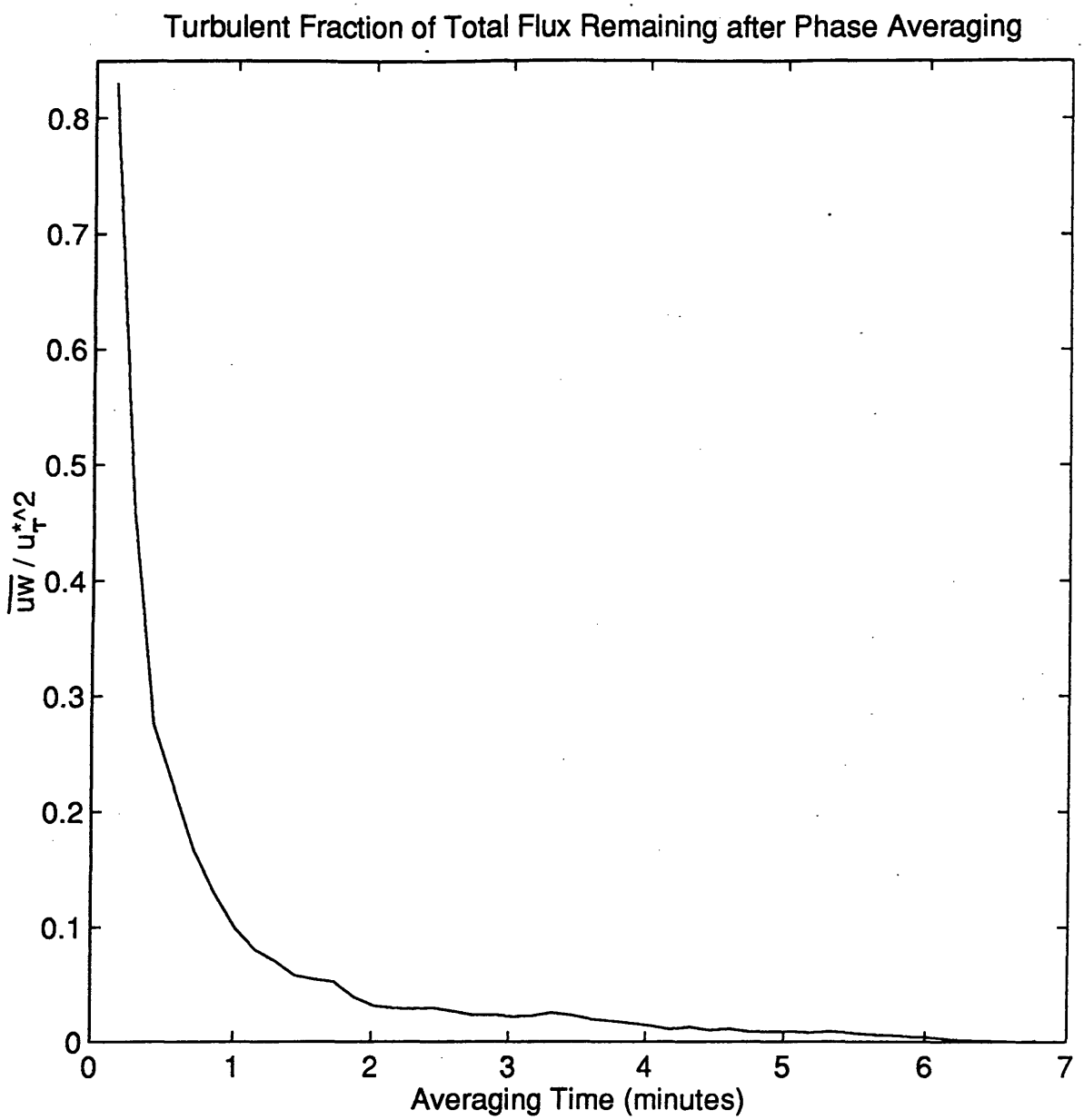

Figure 4.9 Results from the simulation of turbulent reduction by phase averaging. This plot indicates that after phase averaging for one minute, there still remains a 10% contribution to total flux from the turbulence.

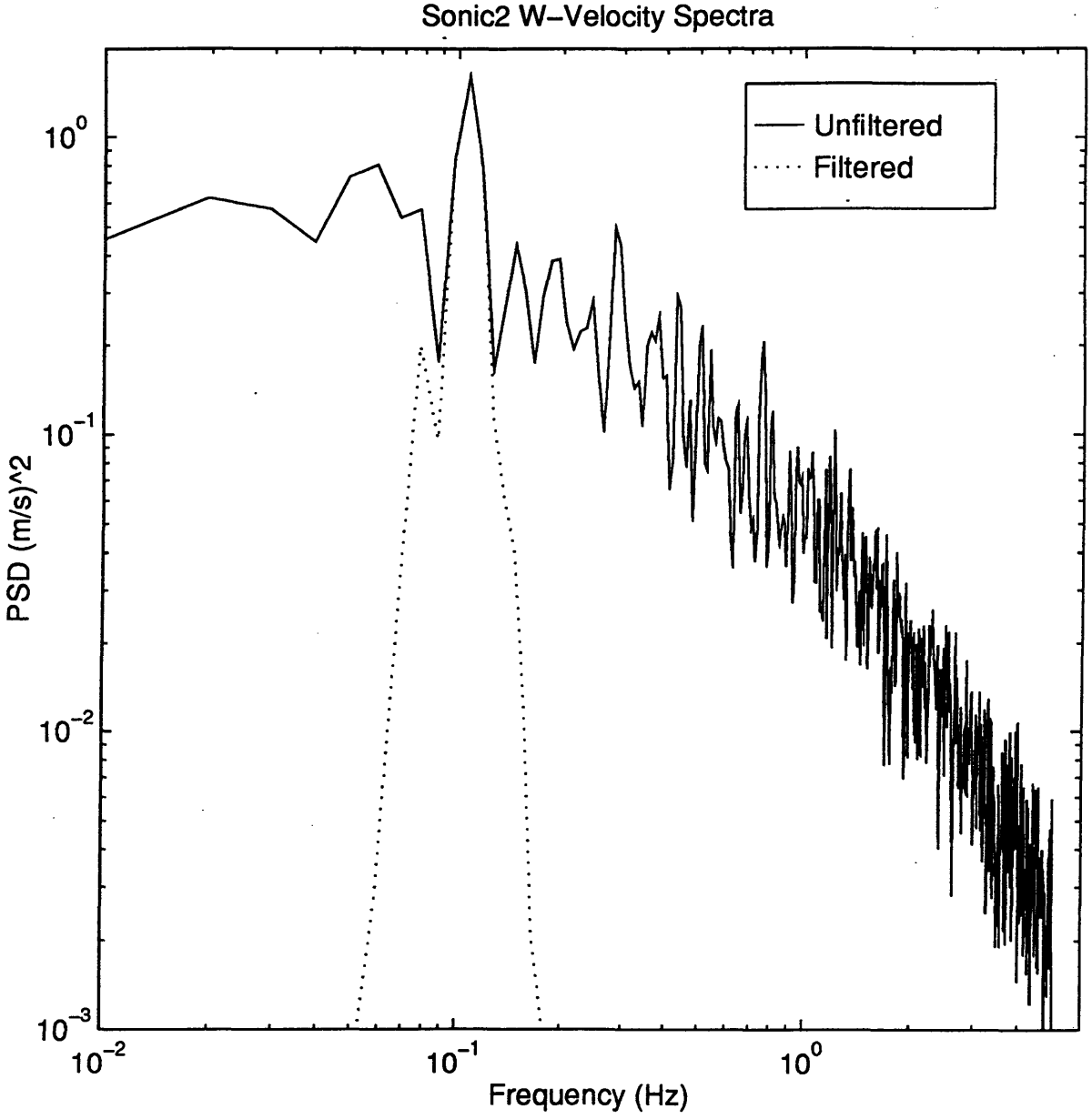

Figure 4.10 Atmospheric horizontal velocity spectrum, before and after filtering. This illustrates the effectiveness of using a filter with a band-pass region centered around the dominant wave frequency as a first step in removing the high frequency atmospheric turbulence.

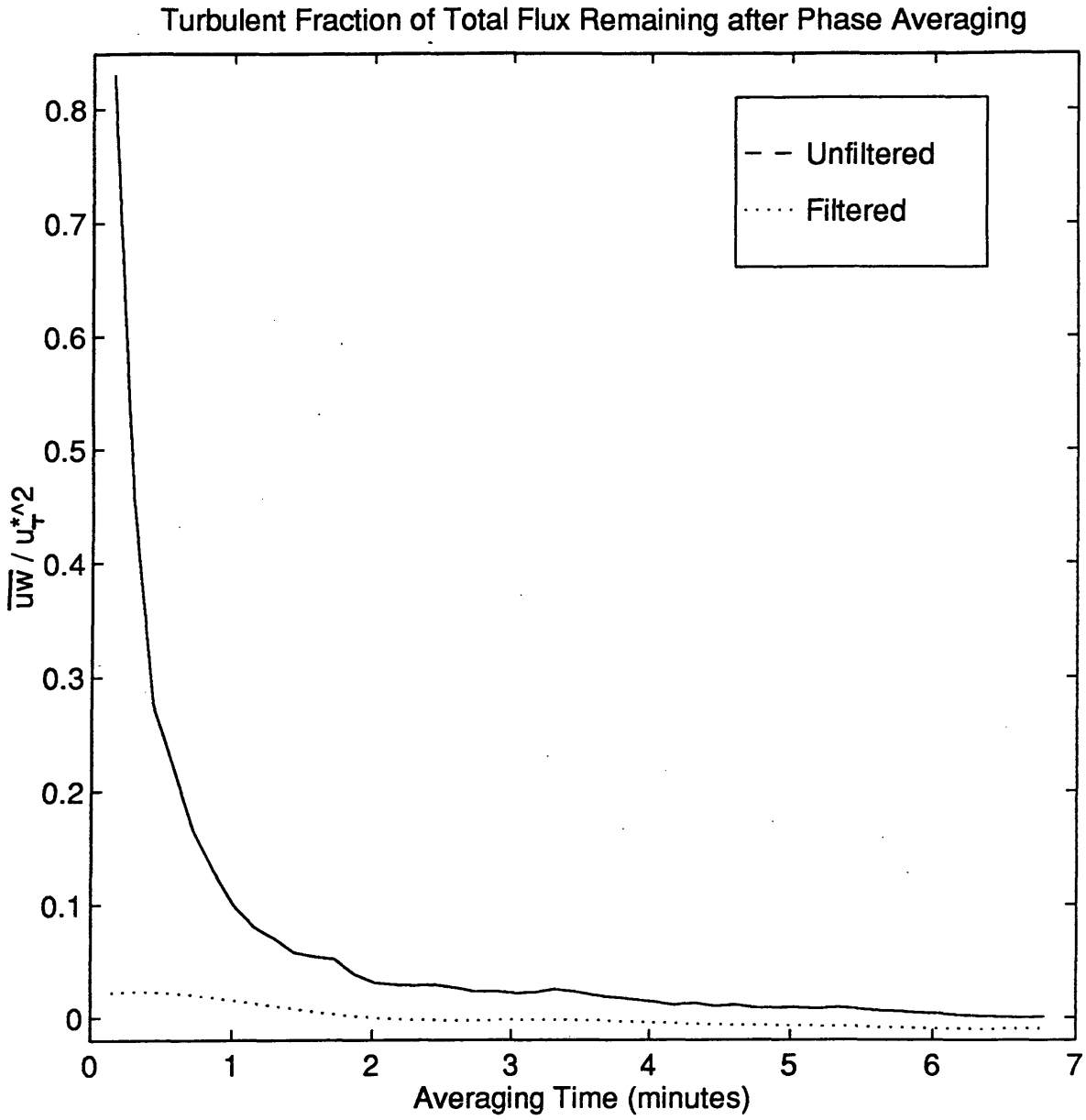

Figure 4.11 Comparison of results from the simulation of turbulent reduction by phase averaging for the filtered and unfiltered time series. The filtered results show a turbulent fraction of only 1.5% remaining, indicating that a combination of filtering and phase-averaging successfully removes the turbulent contribution to total momentum flux.

illustration of the role filtering plays in this analysis, the entire investigation of wave-induced momentum flux will be performed for both the filtered and unfiltered data. A comparison of the filtered and unfiltered results is presented in the Appendix and shows a reduction in flux consistent with the results from the turbulence simulation of Figure 4.11.

In summary, filtering performs a dual purpose. It serves as a tool to remove contributions to the signal at frequencies other than that of the wave frequency, and provides a quantitative means of limiting the study to the most monochromatic wave fields. The filter is used to remove turbulence because the phase averaging times cannot be as long as necessary without encountering problems of frequency modulation. Thus, this combination of filtering and phase averaging is roughly equivalent to phase averaging for a longer period of time. Additionally, filtering reduces the effects of waves generated elsewhere propagating into the experiment site by removing the low frequency swell. The resulting time series can be phase averaged for a short enough time to avoid difficulties with frequency modulation, while still ensuring that the turbulent components average to zero. It is important to note that this limits the results to the most well-defined seas, but as a starting point it is a reasonable procedure.

5. RESULTS AND DISCUSSION

The results presented in this Section are taken from a six-day period between May 3 (JD 123) and May 8 (JD 128), 1995. Employing the procedure outlined in Chapter 4, the one-minute records with the most monochromatic-like wave fields are chosen according to the variance ratio criteria. The overlying velocity fields are then band pass filtered as a first step in isolating the wave-induced fluctuations. For each one-minute record, the phase-averaged horizontal and vertical velocity field is computed (from Equation 4.3) and the wave-induced fluctuations $\tilde{u}$ and $\tilde{w}$ are found by subtracting the mean from the filtered, phase-averaged velocities (as defined in Equation 4.4). The product of these wave-induced velocity fluctuations $-\tilde{u}\tilde{w}$ for a typical one-minute record corresponding to a decaying sea is shown in Figure 5.1. By averaging these products over the wave period at each height, the wave-induced momentum flux profile $-\overline{\tilde{u}\tilde{w}}$ is computed (Figure 5.2). Finally, these flux profiles are bin averaged by a wave age parameter, resulting in a set of curves expressing momentum flux as a function of wave age. Sections 5.1 and 5.2 present the results of this bin averaging, and the results from a number of variations on this analysis are presented in the Appendix.

5.1 BIN AVERAGED MOMENTUM FLUX PROFILES

The ocean wave spectrum does not adjust instantaneously to changes in wind forcing. If this were the case, conditions at the air-sea interface would always be fully developed and the ratio of phase speed (c) to the mean wind velocity at 10 m (U_{10}) would equal a constant, or critical value. Instead, there is a wide range of wave development in the open ocean and the ratio c / U_{10} quantifies the stage of development, or age, of the waves. An often-used criteria for wave age (*Donelan*, 1990) states that a fully developed sea corresponds to $c / U_{10} = 1.2$. Values of wave age considerably less than this critical value correspond to developing seas, i.e., the winds are blowing faster than the waves and contributing to their growth. For wave ages greater than critical, the waves are traveling faster than the winds and thus decaying.

The wave age parameter c / U_{10} is used in this study to bin average the wave-induced momentum flux profiles. That is, profiles computed from time periods with similar wave ages

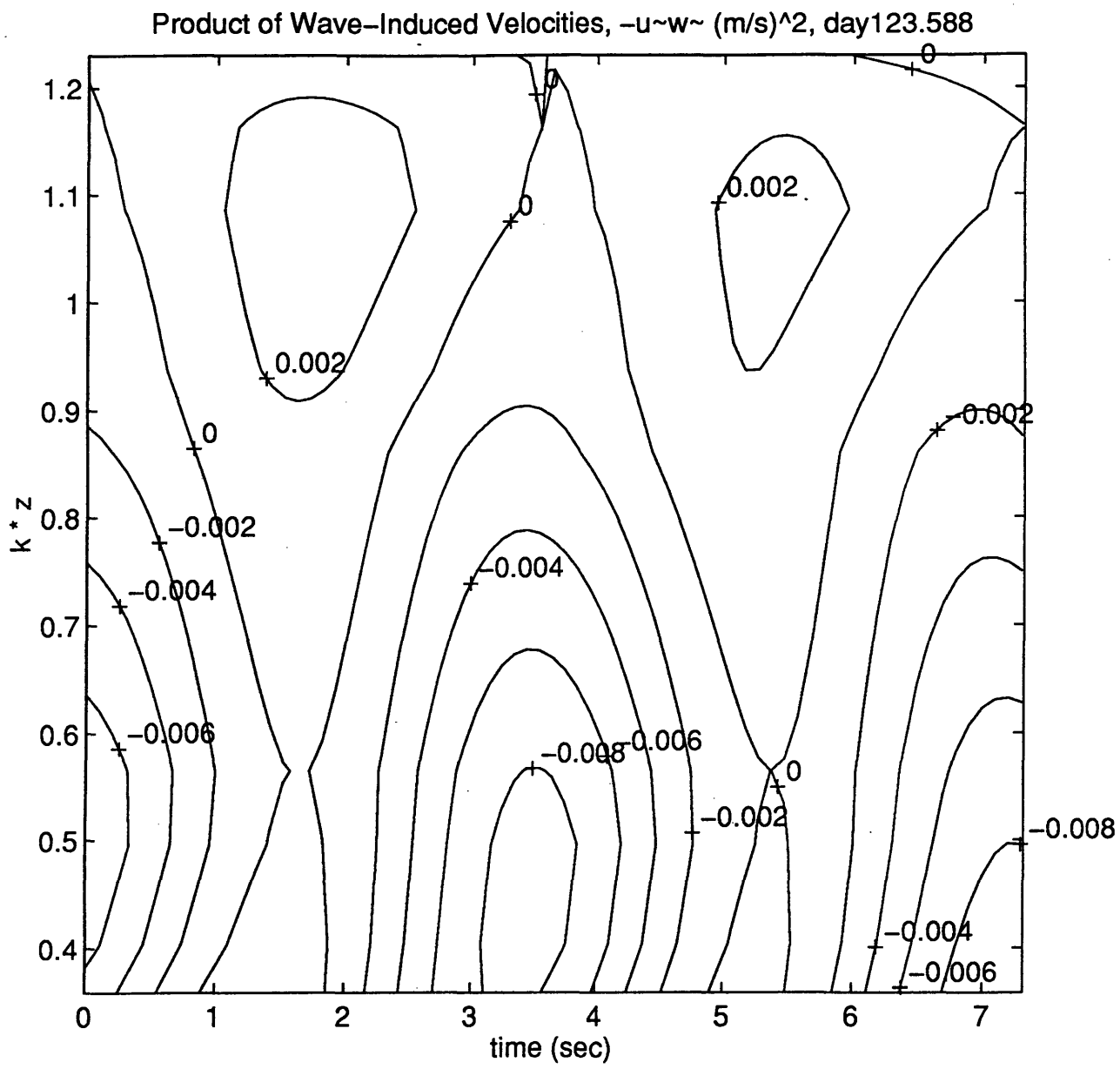

Figure 5.1 Contours of constant $-\tilde{u}\tilde{w}$ for a typical one-minute segment of data over a decaying sea. The x-axis represents one wave period corresponding to the period used for phase averaging.

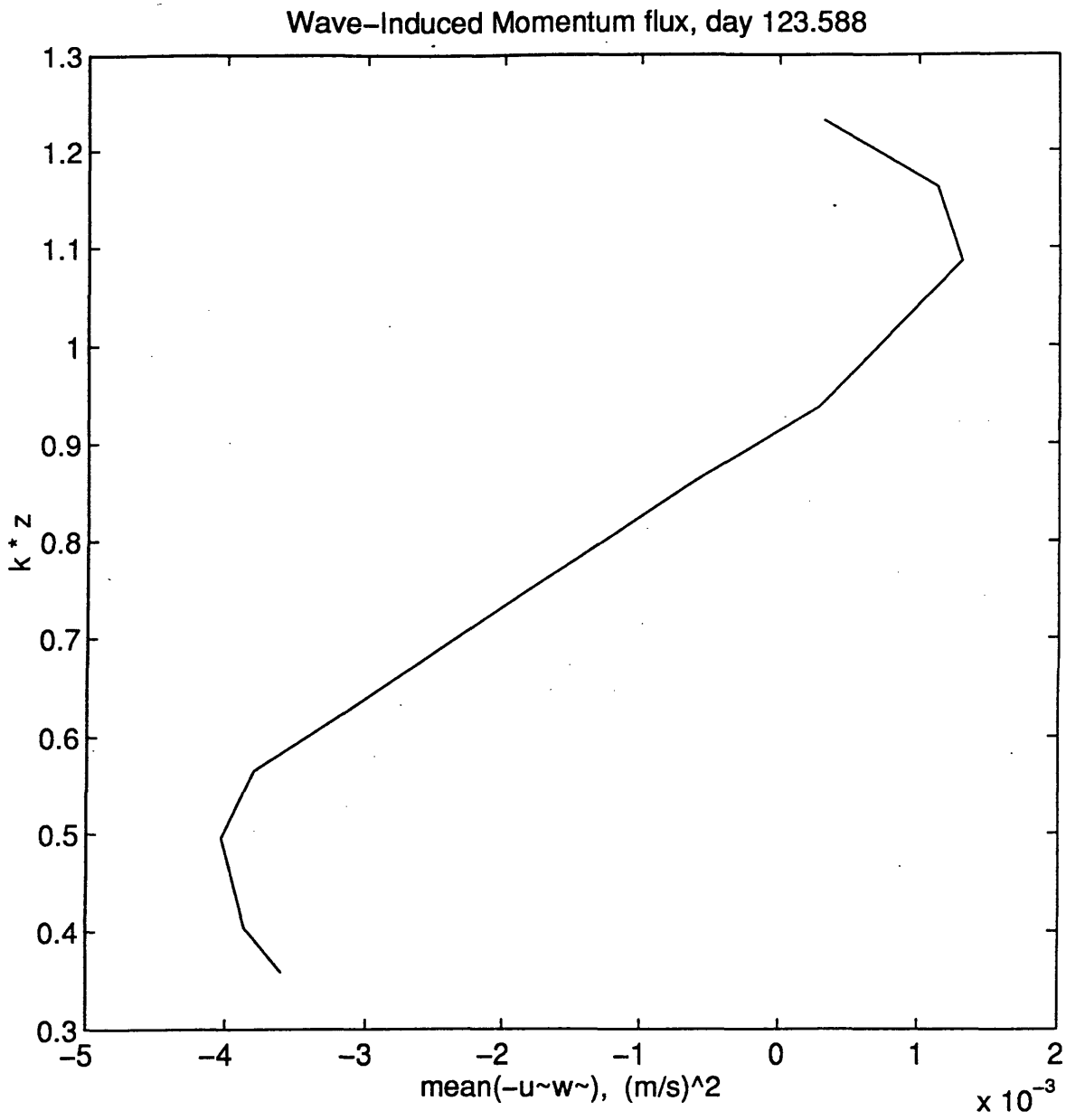

Figure 5.2 Typical profile of wave-induced momentum flux $-\overline{\tilde{u}\tilde{w}}$ for a decaying sea. This was computed from the product of the wave-induced velocities in Figure 5.1 by averaging across one wave period at each height.

are averaged together. The wave age groups, number of profiles averaged in each group, and the corresponding sea state (according to Donelan's criteria) used for bin averaging the wave-induced momentum flux profiles are listed in table 5.1.

Sea State	Bin Number	c / U_{10}	# of profiles, *n*
Developing	1	0.75 - 0.9	11
	2	0.9 - 1.1	138
Fully Developed	3	1.1 - 1.3	244
Decaying	4	1.3 - 1.6	166
	5	1.6 - 2.0	115
	6	2.0 - 2.5	101
	7	2.5 - 3.4	16

Table 5.1 Wave age groups used in the analysis

The number of developing cases is lower than the number of fully developed or decaying for at least two reasons. At the beginning of the portion of the experiment used in this study, the wind speeds were low and there was a significant swell component to the wave field. Thus when the winds began to increase and the waves were developing, two distinct peaks were observed in the spectra and fewer records from this time period pass the variance ratio criteria. Also, Figure 3.3 shows that the winds generally increased gradually during the first 4 days and decreased more rapidly over the final two days. During this first period, the time scales associated with changes in the atmospheric forcing were nearly slow enough to allow the waves to adjust to the changes in wind speed (i.e., the direction remained nearly constant).

The bin averaging results in a set of profiles expressing the normalized wave-induced

momentum flux as a function of dimensionless height and wave age,

$$F_w = -\frac{\overline{\tilde{u}\tilde{w}}}{u_*^2}(kz,\ c/U_{10}) \tag{5.1}$$

These profiles are shown in Figure 5.3 and agree quite well with what is expected conceptually (recall Figures 2.3 and 2.5). The dotted lines represent the standard error, $\sigma/\sqrt{n}$, where σ is the standard deviation and n the number of profiles averaged together. As the edge of the wave-boundary layer is approached, contributions to momentum flux by the waves are expected to become negligible and turbulent effects to dominate. In the region where the flux is predominately turbulent, it is likely that Monin-Obukhov similarity theory applies. In Figure 5.3, the wave-induced momentum flux tends to zero with height for all wave ages as expected, indicating that the wave boundary layer ends and the MO layer begins at a height of approximately $k\,z = 1$. If we assume that total flux is constant with height, this implies that measurements of the turbulence above a height of $k\,z = 1$ can be used to estimate surface fluxes based on MO similarity relations.

5.1.1 Developing Sea

Independent of this constant flux assumption, Figure 5.3 shows that the wave-induced momentum flux has a positive, or downward (corresponding to a positive value for $-\tilde{u}\tilde{w}$) contribution to total flux for a developing sea, indicating a transfer of momentum from the atmosphere to the oceanic wave field. This result is conceptually plausible because the waves must gain momentum and energy from the atmosphere to become larger, and it is consistent with the results of the laboratory study of a developing wave field by *Hsu, Hsu, and Street* (1981) shown earlier in Figure 2.9. Furthermore, an overshoot similar to that observed in the laboratory by *Hsu, Hsu, and Street* and also in the numerical model results of *Mastenbroek et al.* (1996) and *Zou* (1995) is observed in a number of the momentum flux profiles that were averaged together to yield the curves shown in Figure 5.3. Figure 5.4 illustrates one such profile from this study for a time period characterized by developing waves, with a value of c/U_{10} of 0.93. Figure 5.2 is an example of a similar overshoot corresponding to a decaying sea.

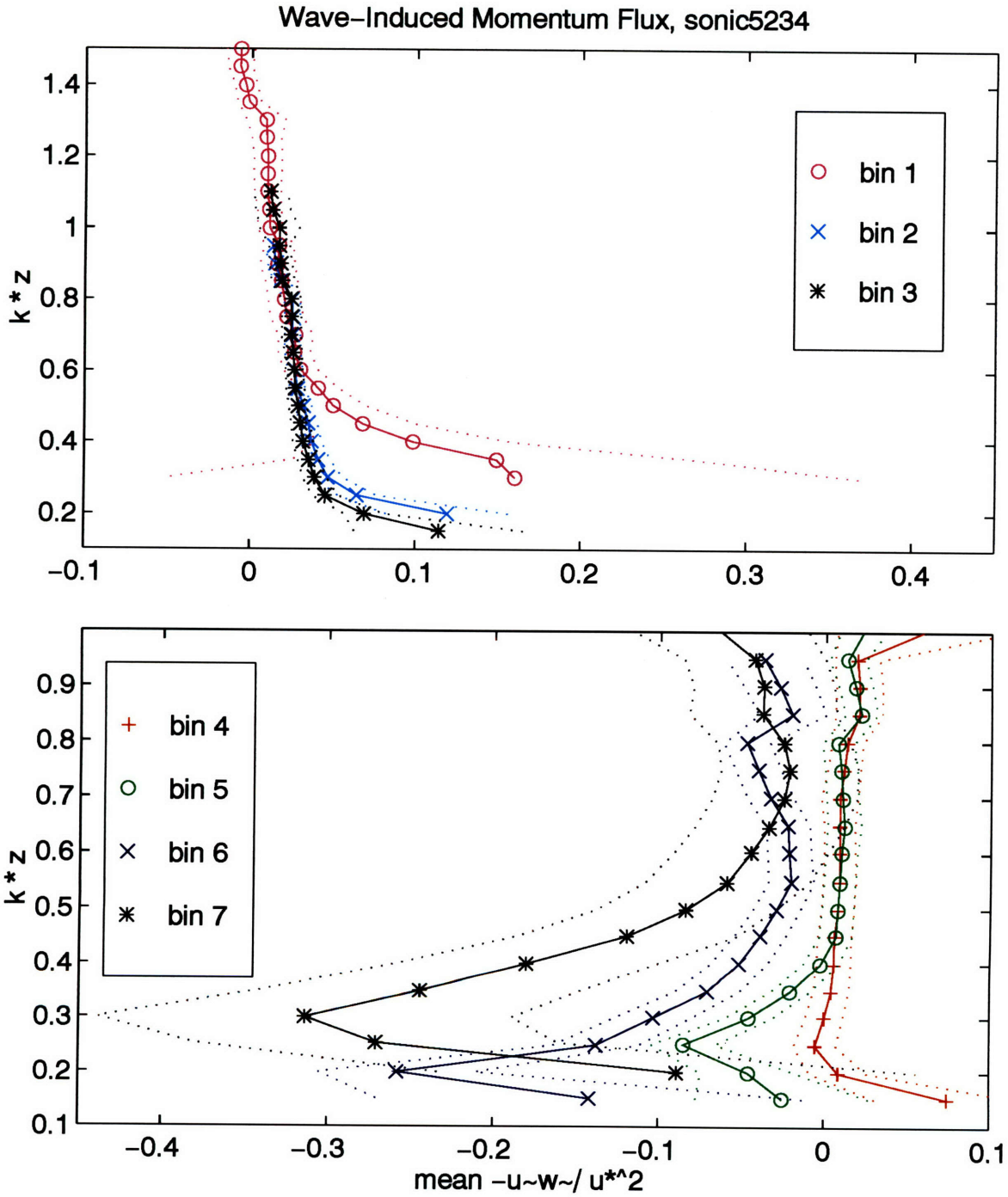

Figure 5.3 Results of bin averaging profiles of wave-induced momentum flux by wave age. The first three bins, corresponding to developing waves, show a transfer of atmospheric momentum to the ocean wave field. The flux is nearly zero for the fully developed sea and becomes negative indicating a transfer of momentum from the waves to the atmosphere for decaying seas. The wave age groups corresponding to each bin are listed in table 5.1.

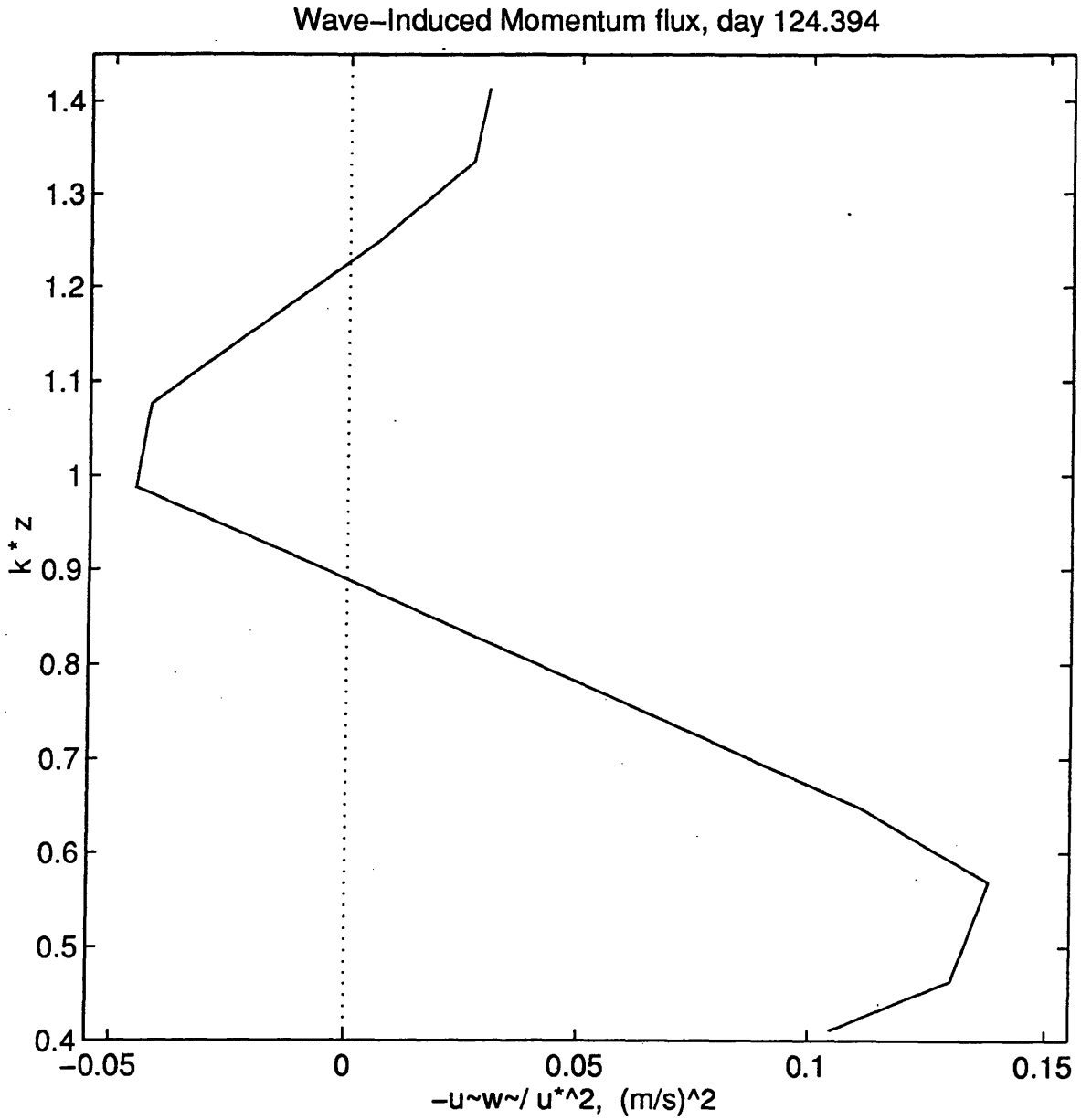

Figure 5.4 Profile of wave-induced momentum flux for a developing sea which shows an overshoot similar to that observed by *Hsu et al.* (1981) in the laboratory and predicted by a number of numerical modeling studies (*Zou*, 1995; *Mastenbroek et al.*, 1996).

5.1.2 FULLY DEVELOPED SEA

For fully developed seas, the results of this study indicate that the wave-induced momentum flux is nearly zero for all heights within the range of measurement, $k\,z > 0.1$. These steady-state seas are generally assumed to be in equilibrium with the atmosphere such that the contribution to the wave-induced momentum flux by form drag of the long waves is negligible and Charnock's relation applies (see Section 2.3). The results shown in Figure 5.3 support this assumption, particularly since the analysis technique is expected to include only the effect of form drag from the longer waves. The form drag due to the smaller, gravity-capillary waves does contribute to the momentum flux near the surface, even for fully developed seas, but this influence has been removed through the filtering and phase averaging process which focused on the dominant wind-driven wave, as well as by our height above the surface. Since the small waves are the instantaneous result of wind blowing on the water, they should always correspond to a transfer of momentum from the atmosphere to the oceanic wave field (downward momentum flux), which is the assumed direction of the flux in any parameterization using Charnock's relation. Thus, the true wave-induced momentum flux profile over a developing sea is expected to have a large positive value very near the surface, most likely closer to the surface than the lowest measurements of this study (i.e., where $k z_o \sim O(1)$).

Recall that the accepted critical value for a fully developed wave field is $c / U_{10} = 1.2$ (*Donelan*, 1990). This value corresponds to bin 3 in Figure 5.3, which has positive values of wave-induced momentum flux at the surface. On the other hand, bin 4 (corresponding to $c / U_{10} = 1.3$ - 1.6) shows nearly zero wave-induced momentum flux at all heights. This indicates that a more appropriate critical value for the wave age parameter is in the range 1.3 - 1.6, somewhat larger than the value of 1.2 that is commonly used. However, the values of U_{10} were not corrected for stability in this analysis, and c / U_{10} might be slightly over-estimated as a result. This is discussed further in Chapter 6.

5.1.3 DECAYING SEA

The most striking results of this analysis are found for wave ages associated with

decaying seas. The wave-induced fraction becomes increasingly negative as momentum is transferred back to the air from the sea. The momentum transfer by the oldest waves reaches a minimum at -0.3 ± 0.1, corresponding to a wave-induced component of total flux approximately equal to -30%. If the assumption of a constant total flux is to hold, this implies that the turbulent component must be +130% of the total to compensate for the negative wave-induced flux (see Figure 2.5b).

The constant flux assumption can be tested using indirect estimates of the fluxes derived by the profile method (described in Section 3.2.3). If the turbulent component is driven primarily by shear, then one could expect a velocity profile with greater near surface shear when compared to a law of the wall profile. It is worth noting that one would expect the opposite to be true over developing seas, where a velocity profile with lower shear is expected. If this hypothesis holds, then one would expect estimates of u_{*_P}, taken from the velocity profile (indicative of the shear) to be smaller than the total flux u_{*_T}, computed from the sonic anemometers for developing seas and larger over decaying seas.

However, the results from this investigation do not seem to support this hypothesis as shown in Figure 5.5. In fact, this figure shows that the opposite appears to be true where u_{*_P} is larger than u_{*_T} at high winds (generally developing seas) and smaller at low wind speeds (generally decaying seas). This result, and others throughout the investigation brings the assumption of a constant flux layer into question. In fact, Figure 5.6 shows that the momentum flux profile at 8 m is generally larger than the flux at 18 m by an amount that appears larger than the flux divergence expected through Equation 2.3. This finding points out the importance of this investigation, since it is imperative that we understand how the waves are affecting the flow in order to understand this behavior.

5.2 General Remarks

Figure 5.3 shows a consistent trend in the wave-induced momentum fluxes with variations in wave age. Larger wave ages correspond to smaller or more negative fluxes. This systematic variation indicates that a parameterization based on wave age may allow Monin-Obukhov similarity theory to be extended into the wave boundary layer. That is, if all the

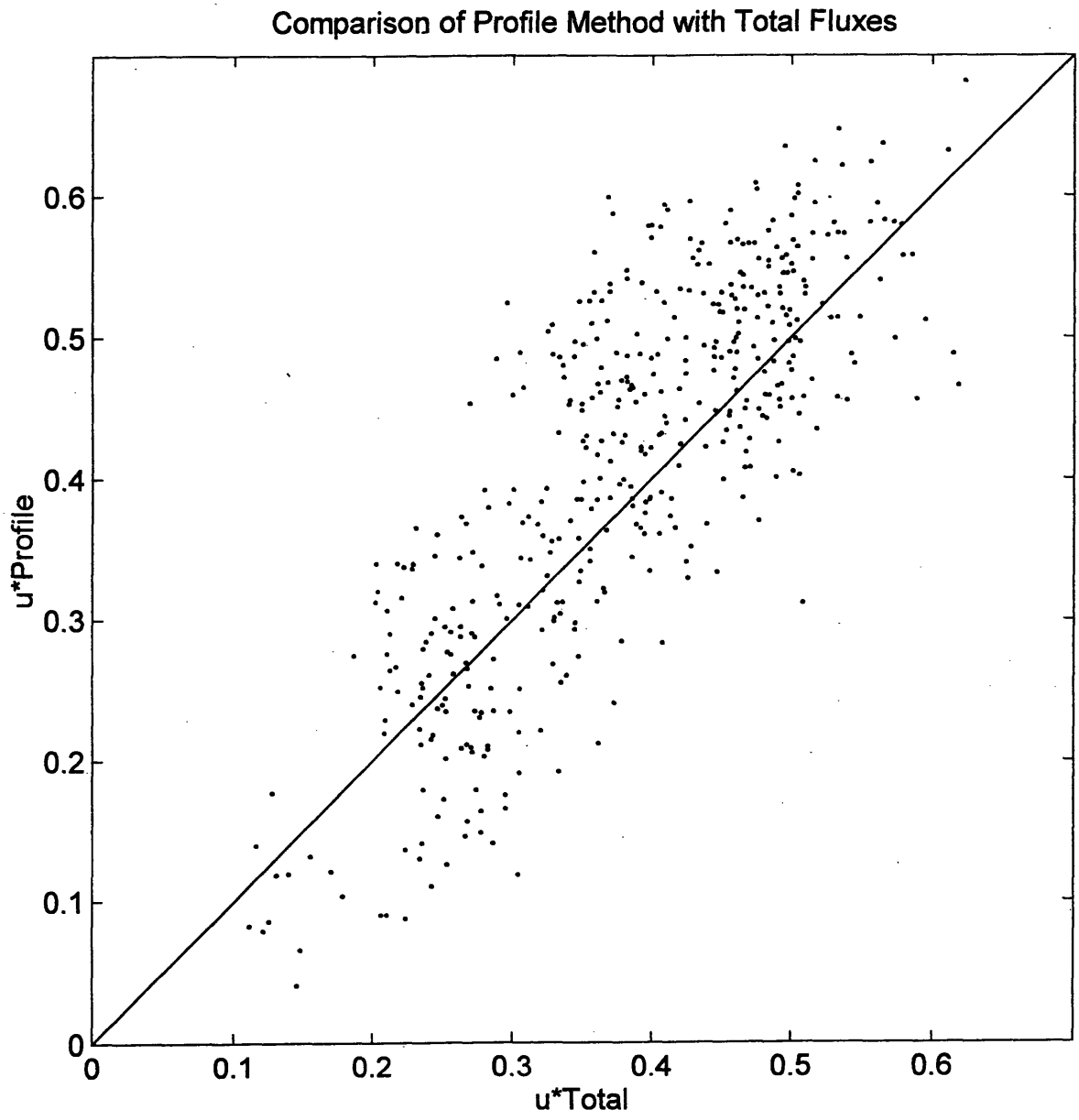

Figure 5.5 Comparison of u_{*_P} calculated by the profile method with the total flux, u_{*_T} computed from sonic anemometer measurements.

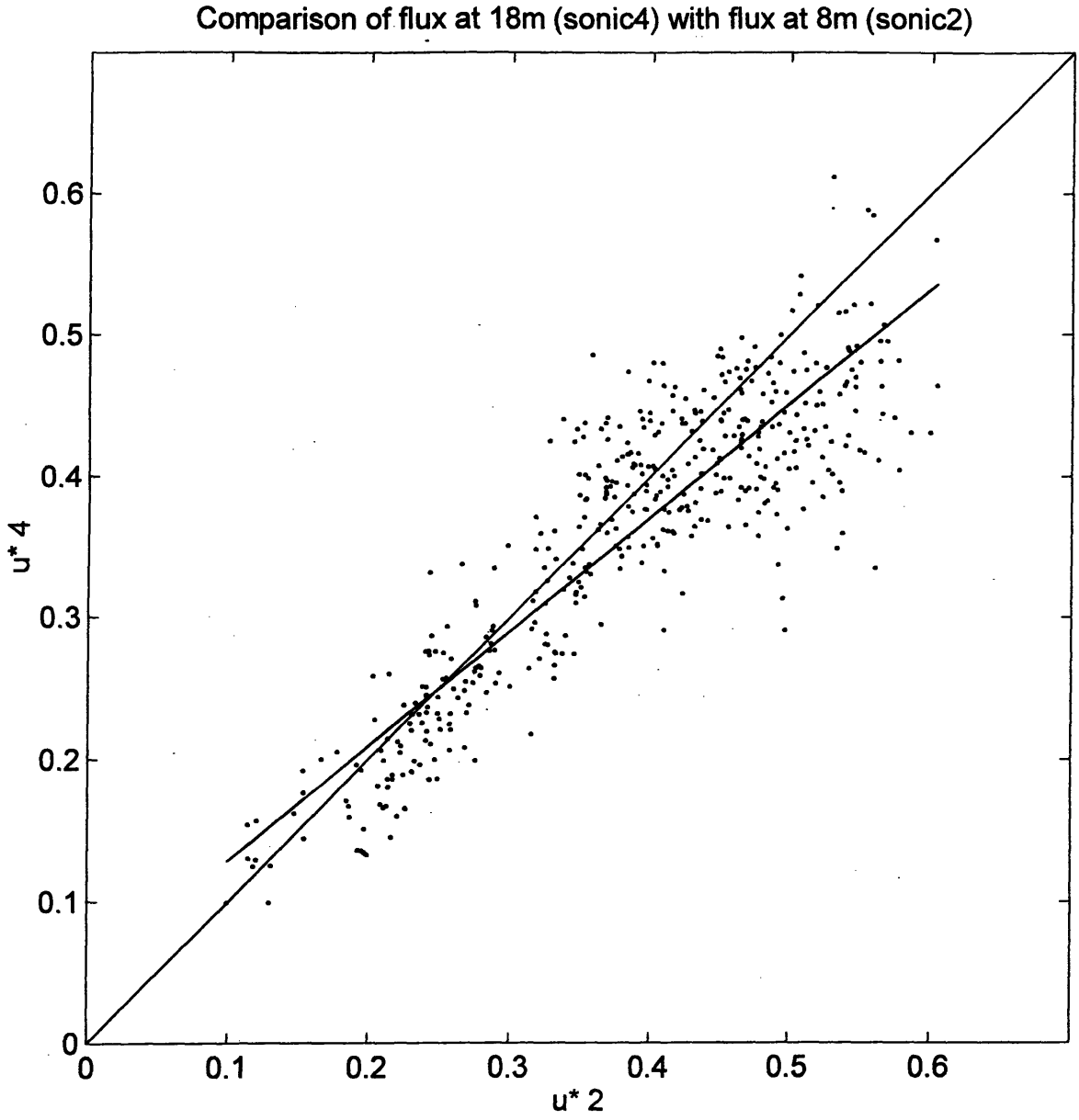

Figure 5.6 Comparison of total flux at 18 m (u_*4) with total flux at 8 m (u_*2).

profiles can be collapsed together to describe the momentum flux as a function of both dimensionless height and wave age, this parameterization can be incorporated into the existing MO theory and new similarity relations can be developed to describe the behavior of turbulence near the air-sea interface.

It is not the goal of this thesis to develop such a parameterization, yet a preliminary investigation reveals a good agreement between the wave-induced momentum flux profiles for a developing sea and the following expression:

$$-\frac{\overline{\tilde{u}\tilde{w}}}{u_*^2}\left(\frac{c}{u_{10}}, kz\right) = e^{-\gamma kz} \tag{5.2}$$

where γ is a parameter that varies as a function of wave age. A value for γ is chosen which provides the best fit to the profiles of wave-induced momentum flux. An illustration of this parameterization for two profiles over a developing sea is shown in Figure 5.7, where $\gamma = 6$ was used for bin 1 and $\gamma = 15$ for bin 3. In both cases, there is an offset between the exponential decay and the data as $k\,z$ increases since the profiles do not tend exactly to zero. This is likely due to the residual turbulent flux that is not removed by either filtering or phase averaging.

Another feature of note in the results shown in Figure 5.3 is that the wave-induced fraction of total momentum flux tends back toward zero near the surface for the decaying waves, while for developing waves the profiles reach their maximum at the lowest data point. That is, both cases tend toward more positive values close to the interface. This behavior is consistent with what is expected conceptually. However, the near-surface values of wave-induced momentum flux are subject to question because at these heights the results are limited by the vertical extent of data as well as the techniques employed in the analysis. The lowest measurement of wind speed is above the wave crests, so the velocity structure in the troughs cannot be resolved and the analysis is limited to heights greater than the wave amplitudes. Additionally, as discussed in Section 5.1.2, the analysis techniques employed in this study limit the results to include only the effect of form drag from the longer waves on momentum flux,

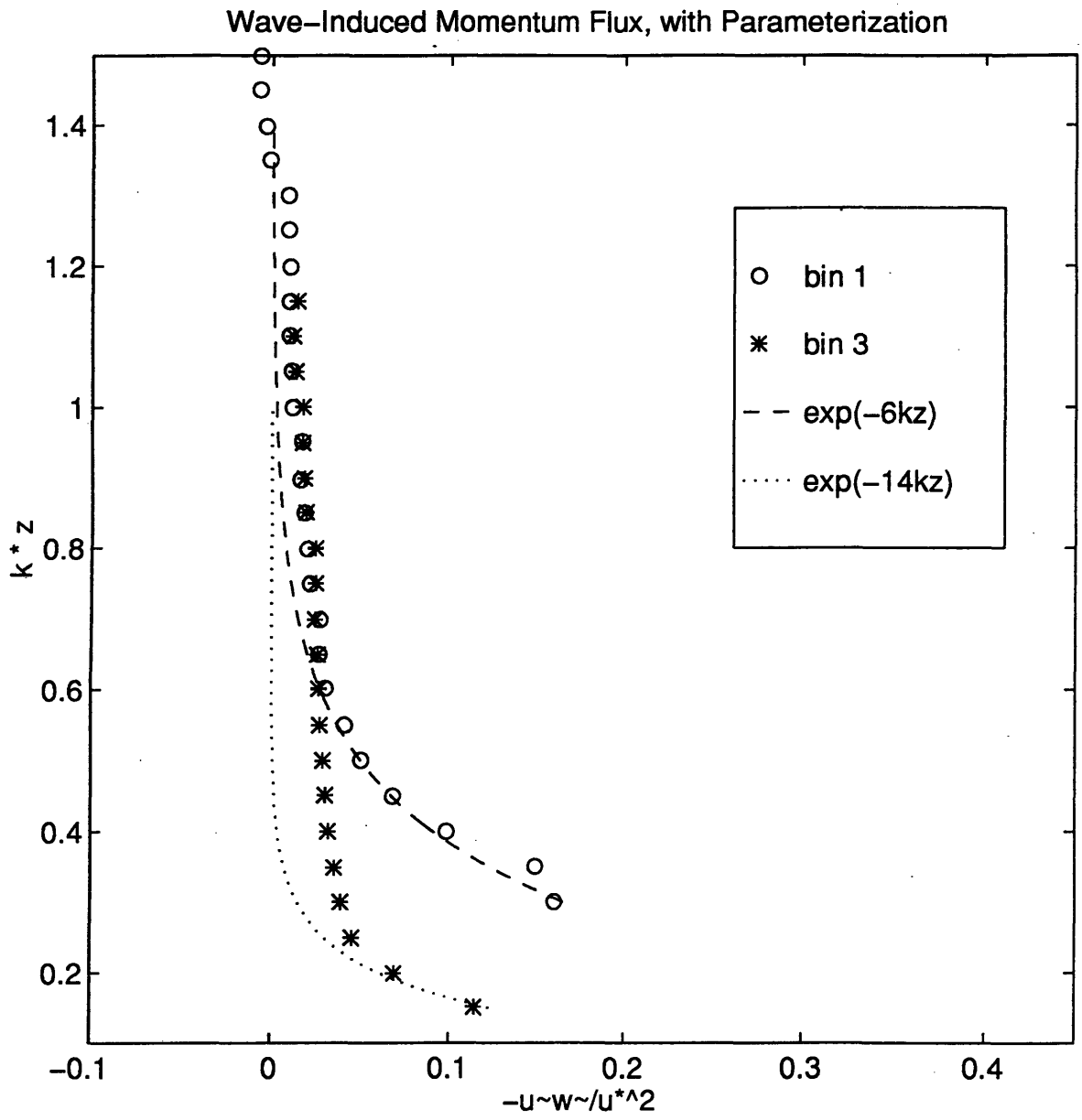

Figure 5.7 Illustration of a preliminary parameterization of wave-induced flux over a developing sea. The exponential curves show a good agreement with the flux profiles.

and not the smaller gravity-capillary waves which may influence the behavior of the flux profiles close to the surface. Thus, it is expected that by including measurements closer to the surface, and by including the effects of form drag from both the long and the short waves in a future investigation, the near-surface behavior of these profiles will be modified.

6. CONCLUSIONS AND FUTURE WORK

The work presented in this thesis constitutes an investigation of the contribution to total momentum flux from form drag due to the dominant wind-driven waves over the open ocean. This investigation has resulted in a set of vertical profiles expressing the wave-induced fraction of total flux as a function of sea state. It reveals a consistent trend in wave-induced momentum flux with variations in the wave age parameter. The success of this study indicates that phase averaging is a viable technique for open ocean conditions, provided certain modifications are made to accommodate a non-monochromatic wave field.

The results show that young, or developing, seas correspond to a positive (downward, according to the notation used in this study) wave-induced component of total momentum flux and mature, or fully developed, seas show no wave-induced flux at the measurement heights of this study ($kz > 0.1$). The contribution to total momentum flux changes sign over decaying waves, such that the dominant waves are supplying momentum to the atmosphere. The percentage of this upward flux to the total flux becomes more negative with increasing wave age. The profiles for all wave ages tend to zero with height as the top of the wave boundary layer is approached, at approximately $k\,z = 1$. Therefore, the behavior of these profiles are consistent with what is expected conceptually. Additionally, they agree well with the results from laboratory studies, and there is qualitative agreement among a number of variations performed as checks on the analysis technique that are given in the Appendix.

These results provide researchers with an opportunity to validify numerical models with data from open ocean conditions. In the past, these models have been compared to data from laboratory experiments (e.g., Mastenbroek *et. al*, 1996) which do not always provide an accurate representation of open ocean conditions and have been limited to developing seas. Additionally, this study leads toward a long-term investigation of the traditional Monin-Obukhov similarity theory over the open ocean. By relating the wave-induced flux at the surface to an easily-measured wave parameter, we are one step closer to extending the applicability of MO similarity theory to the entire marine surface layer. Recall the dimensionless wind shear similarity function defined in Equation 2.7, and restated as a

function of an unknown wave parameter in Equation 2.14. The results from this study provide preliminary evidence that the function ϕ_w may be dependent on $k\,z$ and the wave age. That is, it is likely that a set of curves can be derived expressing $\phi_w(\,kz,\ c/U_{10})$ as was done for momentum flux in this study. Also, it will be interesting to see if the differences between the wind shear function computed over the ocean and the accepted form for this function over land (Equation 2.9) can be reconciled by including the effects of the wave-induced momentum flux determined in this study.

The present study focused on the wave age parameter c/U_{10} as the important variable relating wave-induced momentum flux to sea state. The results indicate that the critical value of c/U_{10} for a fully developed sea is between 1.3 and 1.6, slightly larger than the commonly accepted value of 1.2 (*Donelan*, 1990). However, the values for U_{10} used in this study were not corrected for stability. Manipulation of Equation 3.20 reveals that this correction is defined according to:

$$u_N(z) = u(z) + \frac{u_*}{\kappa}\psi_m(z) \tag{6.1}$$

where $u_N(z)$ is the neutral (stability-corrected) horizontal velocity at height z. For this study, where conditions were near neutral, the ratio U_{10}/U_{10_N} is approximately 0.97. Thus, the critical values of 1.3-1.6 reported earlier should be reduced to 1.27-1.56.

It is also important to investigate the dependence of wave-induced momentum flux on other wave parameters. Another definition of wave age is the ratio of wave phase speed to friction velocity c/u_*. An accepted criteria for a fully developed sea is $c/u_* = 25$-30 (*Volkov*, 1970), and a preliminary investigation reveals that this value may also be inappropriate. Figure 6.1 shows a plot of c/u_* vs. c/U_{10_N} from the six days of data used in this study. Fitting a line to the data reveals that the range of critical values for c/U_{10_N} of 1.26-1.56 corresponds to $c/u_* = 36$ - 46, notably larger than the traditional criteria of 25-30. More work is needed to study this and other wave parameters.

Although the results of this study have led to some promising conclusions, the process toward a comprehensive understanding of the fluxes in a marine boundary layer has only begun. There are a number of modifications to be made to this study for further analysis, as

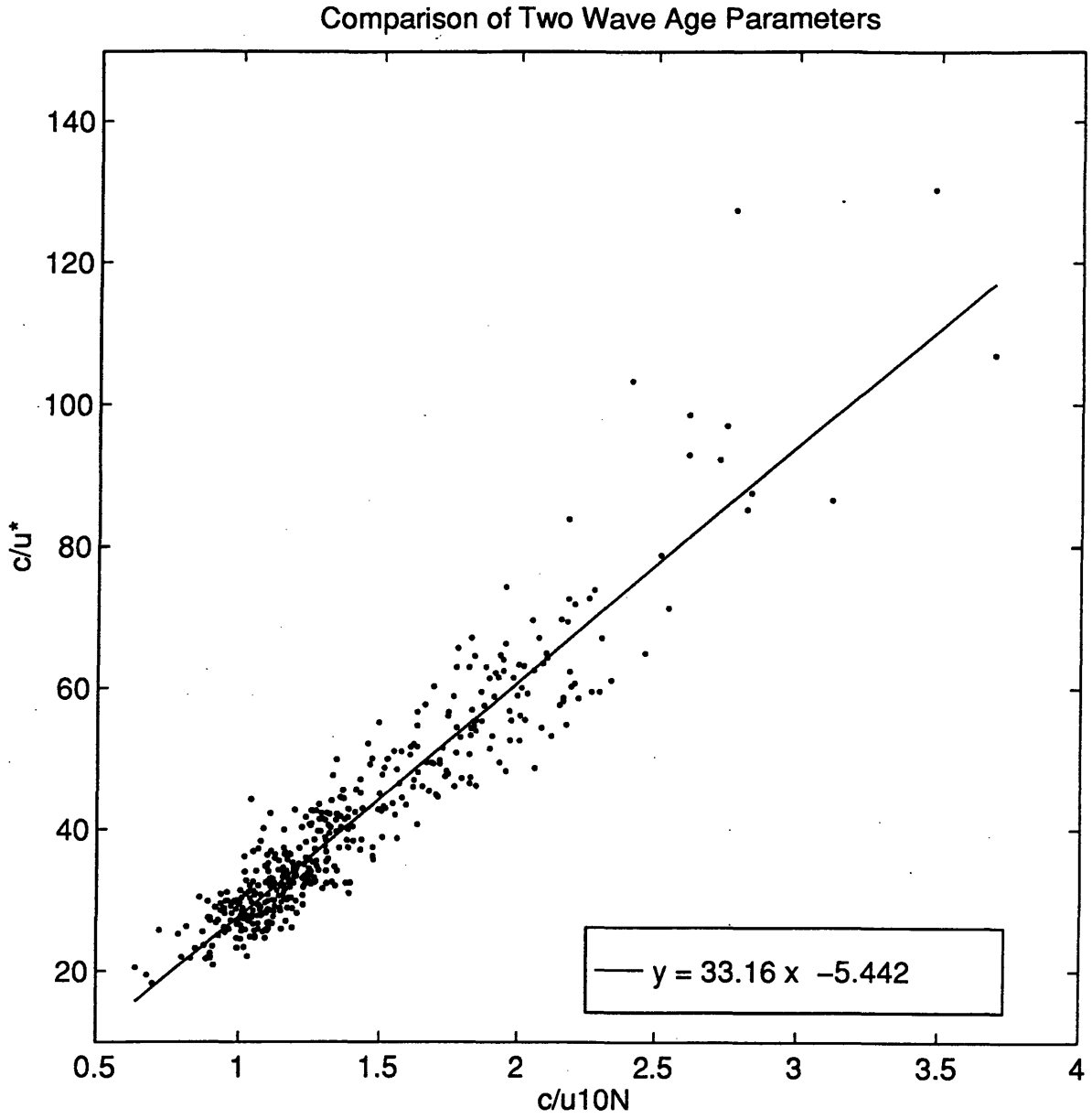

Figure 6.1 Comparison of the wave age parameters c / U_{10} and c / u_*

well as important issues to be addressed in future studies. In order to resolve the discrepancy in the magnitudes of wave-induced momentum flux profiles for large wave numbers, the data from the cup anemometers will be corrected for motion. It was assumed that the wind and wave fields were aligned, based on visual observation. This will be verified by incorporating the remaining three wave wires into the analysis to compute the directional wave spectra.

It would also be interesting to perform the analysis using a phase averaging period based on the swell frequency. The decay of these waves is a very slow process and they may travel long distances before breaking upon the shore or becoming another system's swell. In the latter case, one might expect the direction of the momentum flux from these waves to remain upwards even if the rest of the wave field is developing. This would allow us to investigate whether the momentum flux from swell to wind remains even over otherwise developing seas.

Additionally, future experiments designed to study interactions between the wind and wave fields should include measurements of wind speed closer to the surface than those used in this study. Laboratory experiments have used instrumented floats to capture the structure of the velocity fields between wave crests. If a similar measurement technique were employed in the open ocean, the present analysis could be extended to include the behavior of the very near surface fluxes and to include the effects of the smaller gravity waves. This would prove to be a difficult task, but may be possible using fiber-optics and laser Doppler anemometry.

The assumption of a constant total flux layer must also be addressed in future work. As discussed in Section 2.2 and Chapter 5, there are a number of uncertainties in applying this assumption to the marine boundary layer, and although the implications of this assumption to the results are discussed, this assumption was not part of the analysis. The idea of a constant flux layer over the ocean is merely an extension of the theory validated over land. This theory assumes stationarity, zero subsidence, and horizontal homogeneity, conditions which are valid at large scales over the ocean but are unlikely at the small scales (i.e., intrawave length) this study has investigated.

There is reason to expect some flux divergences over decaying seas if the upward wave-induced momentum flux is acting to accelerate the flow. Under these conditions, it is possible that the constant flux assumption only applies to the turbulent and viscous components, as

is the case over land. That is, the sum of the turbulent and viscous fluxes may remain constant with height, and total flux varies with the effect of the wave-induced components near the surface. To investigate this possibility, we can compare measurements made at height (above the wave boundary layer) of total flux with those values we measure near the surface. Preliminary work presented in Section 5.1.3 has indicated that these values are not equal. A future investigation will involve checking if the estimates for wave-induced momentum flux can account for the difference.

REFERENCES

Andreas, E.L., J.B. Edson, E.C. Monahan, M.P. Rouault, and S.D. Smith,1995. "The spray contribution to net evaporation from the sea: A review of recent progress." *Boundary-Layer Meteorology*, **72**, 3-52.

Businger, J.A., J.C. Wyngaard, Y. Izumi, and E.F. Bradley, 1971. "Flux-profile relationships in the atmospheric surface layer." *Journal of the Atmospheric Sciences*, **28**, 181-189.

Chalikov, D.V. and M.Yu. Belevich, 1993. "One-dimensionsal theory of the wave boundary layer." *Boundary-Layer Meteorology*, **63**, 65-96.

Champagne, F.H., C.A. Friehe, J.C. LaRue, and J.C. Wyngaard, 1977. "Flux measurements, flux estimation techniques, and fine-scale turbulence measurements in the unstable surface layer over land." *Journal of the Atmospheric Sciences*, **34**, 515-530.

Charnock, H.,1955. "Wind stress on a water surface." *Quart. J.Roy. Meteor.Soc.*,**81**,639-640.

Donelan, M.A, 1990. "Air-Sea Interaction." *The Sea: Ocean Engineering Science*, vol. 9A, LeMehaute, B. and D.M. Hanes, eds., New York: John Wiley, 239-292.

Donelan, M.A., F.W. Dobson, S.D. Smith, and R.J. Anderson, 1993. "On the dependence of sea surface roughness on wave development." *Journal of Physical Oceanography*, **23**, 2143-2149.

Deardorff, J.W., 1967. "Aerodynamic theory of wave growth with constant wave steepness." *Journal of the Oceanographical Society of Japan*, **23**:6, 278-297.

Dyer, A.J. and E.F. Bradley, 1982. "An alternative analysis of flux-gradient relationships at the 1976 ICE." *Boundary-Layer Meteorology*, **22**, 3-19.

Dyer, A.J., 1974. "A Review of Flux-Profile Relationships." *Boundary Layer Meteorology*, **7**, 363-372.

Earle, D.M. and J.M. Bishop, 1984. *A Practical Guide to Ocean Wave Measurement and Analysis*, ENDECO, Inc., Marion, MA.

Edson, J. B., J. E. Hare and C. W. Fairall, 1996. Direct covariance flux estimates from moving platforms at sea, submitted to *J. Atmos. Oceanic Tech.*

Fairall, C.W., E.F. Bradley, D.P. Rogers, J.B. Edson, and G.S. Young, 1996a. "Bulk parameterization of air-sea fluxes for Tropical Ocean-Global Atmosphere Coupled-Ocean Atmosphere Response Experiment." *Journal of Geophysical Research,* **101**, C2, 3747-3764.

Fairall, C.W., A.B. White, J.B. Edson, and J.E. Hare, 1996b. "Integrated shipboard measurements of the marine boundary layer." *Atmos. Oceanic Tech.*, submitted.

Finnigan, J.J., F. Einuadi, and D. Fua, 1984. "The interaction between an internal gravity wave and turbulence in the stably-stratified nocturnal boundary layer." *Journal of the Atmospheric Sciences,* **41**:16, 2409-2436.

Geernaert, G.L., 1990. "Bulk Parameterizations for the wind stress and heat fluxes." *Surface Waves and Fluxes: Volume I - Current Theory*, G.L. Geernaert and W.L. Plant, eds., Netherlands: Kluwer Academic Publishers, 91-172.

Geernaert, G.L., 1988. "Drag coefficient modeling for the near coastal zone." *Dynam. Atmos. Oceans*, **11**, 307-322.

Godfrey, J.S. and A.C.M. Beljaars, 1991. "On the turbulent fluxes of buoyancy, heat, and moisture at the air-sea interface at low wind speeds." *Journal of Geophysical Research*, **96**, C12, 22043-22048.

Hare, J.E., 1995. "A similarity analysis of the structure of the wave-induced flow fields." Ph.D. thesis, The Pennsylvania State University, 165 pp.

Hare, J. E., J. B. Edson, E. J. Bock, and C. W. Fairall, 1992. Progress on direct covariance measurements of air-sea fluxes from ships and buoys. *Tenth Symp. Turbulence and Diffusion*, Portland, OR, Amer. Meteor. Soc., 281-284.

Hasselmann, D. and J Bösenberg, 1991. "Field measurements of wave-induced pressure over wind-sea and swell." *Journal of Fluid Mechanics,***230**, 391-428.

Högström, Ulf, 1988. "Non-dimensional wind and temperature profiles in the atmospheric surface layer: a re-evaluation." *Boundary-Layer Meteorology,* **42,** 55-78.

Holton, J.R., 1979. *An Introduction to Dynamic Meteorology*, New York: Academic Press, 391 pp.

Hsu, C., E.Y. Hsu, and R.L. Street, 1981. "On the structure of turbulent flow over a progressive water wave: theory and experiment in a transformed, wave-following co-ordinate system." *Journal of Fluid Mechanics*, **105**, 87-117.

Jones, I.S.F. and Y. Toba, 1995. "Comments on 'The dependence of sea surface roughness on wave development' ." *Journal of Physical Oceanography,* **25,** 1905-1907.

Kaimal, J.C., J.C. Wyngaard, Y. Izumi, and O.R. Coté, 1972. "Spectral characteristics of surface-layer turbulence." *Quarterly J.R. Met. Soc.*, **98**, 563-589.

Krauss, T.P., L. Shure, and J.N. Little, 1994. *Signal Processing Toolbox User's Guide.* Natick, MA: The Math Works, Inc.

Mastenbroek, C., V.K. Makin, M.H. Garat, and J.P. Giovanangeli, 1996. "Experimental evidence of the rapid distortion of turbulence in the air flow over water waves." *Journal of Fluid Mechanics,* **318**, 273-302.

Monin, A.S., and Obukhov, A.M., 1954. "Basic laws of turbulent mixing in the surface layer of the atmosphere." *Tr. Akad. Nauk SSSR, Geofiz Inst.,* **151**, 163-87.

Obukhov, A.M., 1946. "Turbulence in an atmosphere with a non-uniform temperature." *Tr. Akad. Nauk. USSR, Inst. Teoret. Geofiz,* **1**. Translated and published in *Boundary Layer Meteorology,* **2**, 7-29, 1971.

Panofsky, H.A, and J.A. Dutton, 1984. *Atmospheric Turbulence.* New York: John Wiley & Sons.

Paulson, C.A., 1970. "The mathematical representation of wind speed and temperature profiles in the unstable atmospheric surface layer." *Journal of Applied Meteorology,* **9**, 857-861.

Smith, S.D., 1988. "Coefficients for sea surface wind stress, heat flux, and wind profiles as a function of wind speed and temperature." *Journal of Geophysical Research,* **93**, 15467-15472.

Snyder, R.L., F.W. Dobson, J.A. Elliot, and R.B. Long, 1981. "Array measurements of atmospheric pressure fluctuations above surface gravity waves." *Journal of Fluid Mechanics*, **102**, 1-59.

Volkov, Y.A., 1969. "The spectra of velocity and temperature fluctuations in the airflow above the agitated sea surface."*Izvestia Atmospheric and Oceanic Physics*,**5**,723-730.

Wieringa, J., 1980. "A Revaluation of the Kansas mast influence on measurements of stress and cup anemometer overspeeding." *Boundary-Layer Meteorology*, **18**, 411-430.

Wyngaard, J.C., 1973. "On Surface-Layer Turbulence." *Workshop on Micrometeorology*, Duane A. Haugen, ed., Boston, MA: American Meteorological Society, 101-149.

Zou, Q.P., 1995. "A viscoelastic model for turbulent flow over undulating topography and progressive waves." Ph.D. Thesis, University of California, San Diego, Scripps Institution of Oceanography, 91 pp.

APPENDIX: VARIATIONS ON THE ANALYSIS

As a means of checking the validity of the results, variations on the analysis are presented in this appendix. The results of these modifications are qualitatively consistent with those presented earlier, although there are some quantitative discrepancies. The discussion in this thesis accounts for most of these differences by considering the physical processes involved, and contends that the original findings presented in Section 5.1 (Figure 5.3) are the most tenable.

A.1 INCREASED DATA RESOLUTION

The original wave-induced momentum flux profiles shown in Figure 5.3 were computed using sonic anemometer measurements at only four heights for both the horizontal and vertical wind speeds. Specifically, sonics 5, 2, 3, and 4 were used (see Section 3.1.1 and Figure 3.4 for the location of these instruments). The first variation of this analysis involves using the cup anemometers for horizontal wind speed instead of the sonics, while still using sonics 5, 2, 3, and 4 for the vertical velocity measurements. This variation improves data resolution by spanning the same vertical measurement range with eleven cup anemometers instead of the four sonic anemometers. However, the drawback of this approach is that the cup anemometer measurements have not been corrected for motion. It is expected that this contamination is small, but the results show it may not be negligible, particularly for low wind speeds over large but decaying waves where the effect of the platform motion is a larger percentage of the actual wind speed. Another possible source of error in this variation is that the cup anemometers, compared to the sonic anemometers which have no moving parts, have a larger moment of inertia, making them susceptible to overspeeding (*Wieringa*, 1980).

The results of this first variation are presented in Figure A.1. A comparison of this figure with the original results (Figure 5.3) reveals a good agreement for low wave ages. The wave-induced flux is positive near the surface and tends to zero with height for the developing sea, and is nearly zero for the fully developed sea. For larger wave ages, the direction and shape of the flux is consistent for both cases; however, there are some quantitative differences. The

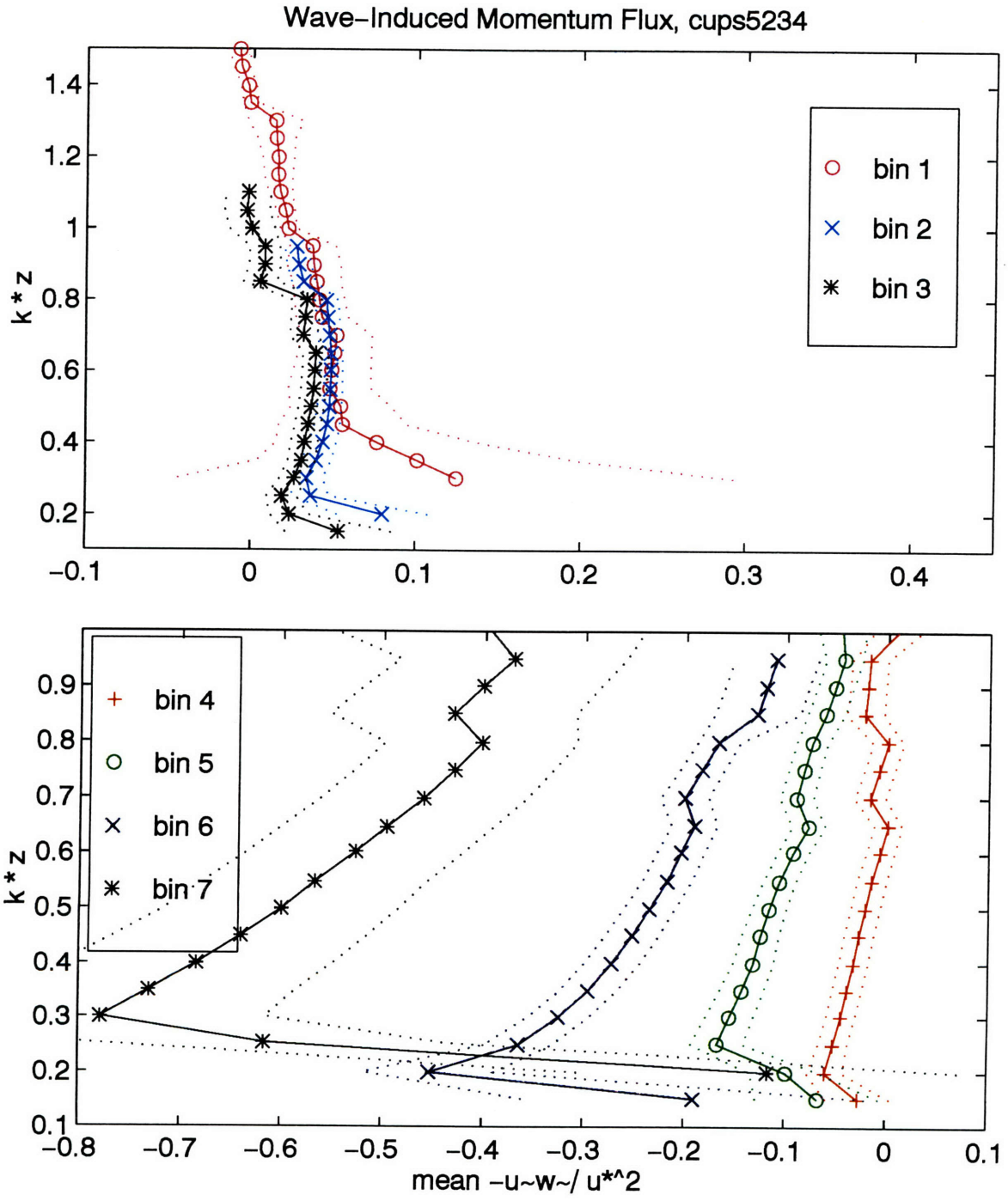

Figure A.1 Results of the first variation of the bin averaging analysis. 11 Cup anemometer measurements for horizontal velocity were used instead of the original 4 sonic anemometers.

magnitude of the wave-induced contribution to total flux reaches a negative maximum at approximately 80% for the results of this variation, as compared to 30% for the original results. Also, the depth of the layer of wave influence is greater for this variation.

It is likely that these differences are largely due to the effect of platform motion in the cup anemometer data. Consistent with what is observed in Figure A.1, this contamination should have a larger effect at higher wave ages since these periods correspond to conditions of large waves and low wind speeds. The platform continues to move with the waves and the motion makes up a larger fraction of the total measured velocity because of the lower wind velocities. In future work the cup anemometer data will be corrected for motion to check this hypothesis. Furthermore, it is difficult to physically justify a wave contribution to flux as large as 80%, as this component would be far more noticeable in the cospectral plots of the total flux (Figure A.2). The area under the cospectral peak at the wave frequencies clearly does not make up 80% of the total area. Additionally, the 30% contribution found originally is more consistent with previous investigations.

Since the general shape of all of the profiles remains unchanged, the quantitative discrepancy at large wave numbers does not appear to be related to the increased resolution of the vertical velocity measurements in this variation. Thus, the qualitative agreement between the results is regarded as evidence that the results presented in Figure 5.3 provide a good estimate of the wave-induced contribution to total momentum flux.

A.2 Unfiltered Wind Data

To illustrate the role filtering plays in the analysis and to quantify its effect, this Section presents a comparison between the original results (Section 5.1) which were computed by phase averaging the filtered wind velocities and the results of a similar analysis using unfiltered velocities. Plots of the wave-induced fraction of total momentum flux for both the filtered and unfiltered cases are shown in Figures A.3 and A.4 for the first three bins and the last four bins, respectively. These figures show a similar shape for the filtered and unfiltered results, with more scatter and larger significant error in the unfiltered data; however the unfiltered profiles appear to be consistently shifted horizontally 0.2 units to the right. That

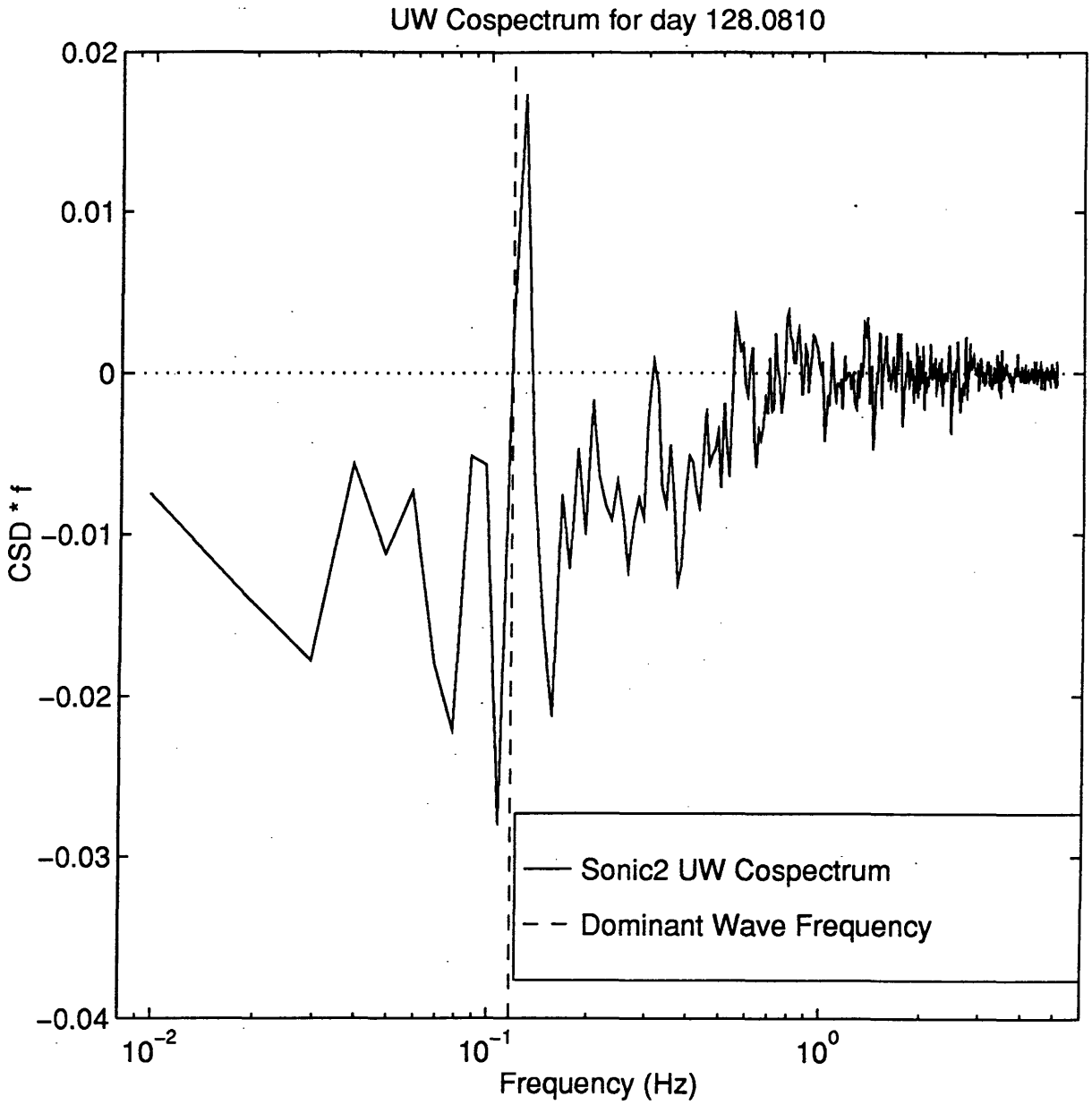

Figure A.2 Cospectrum of horizontal and vertical wind velocities. The large positive values corresponding to the dominant wave frequency (dotted line) illustrate a significant wave contribution to the atmospheric signal, however it is apparent that this contribution is not 80% of the total flux as the results from Figure A.1 indicated.

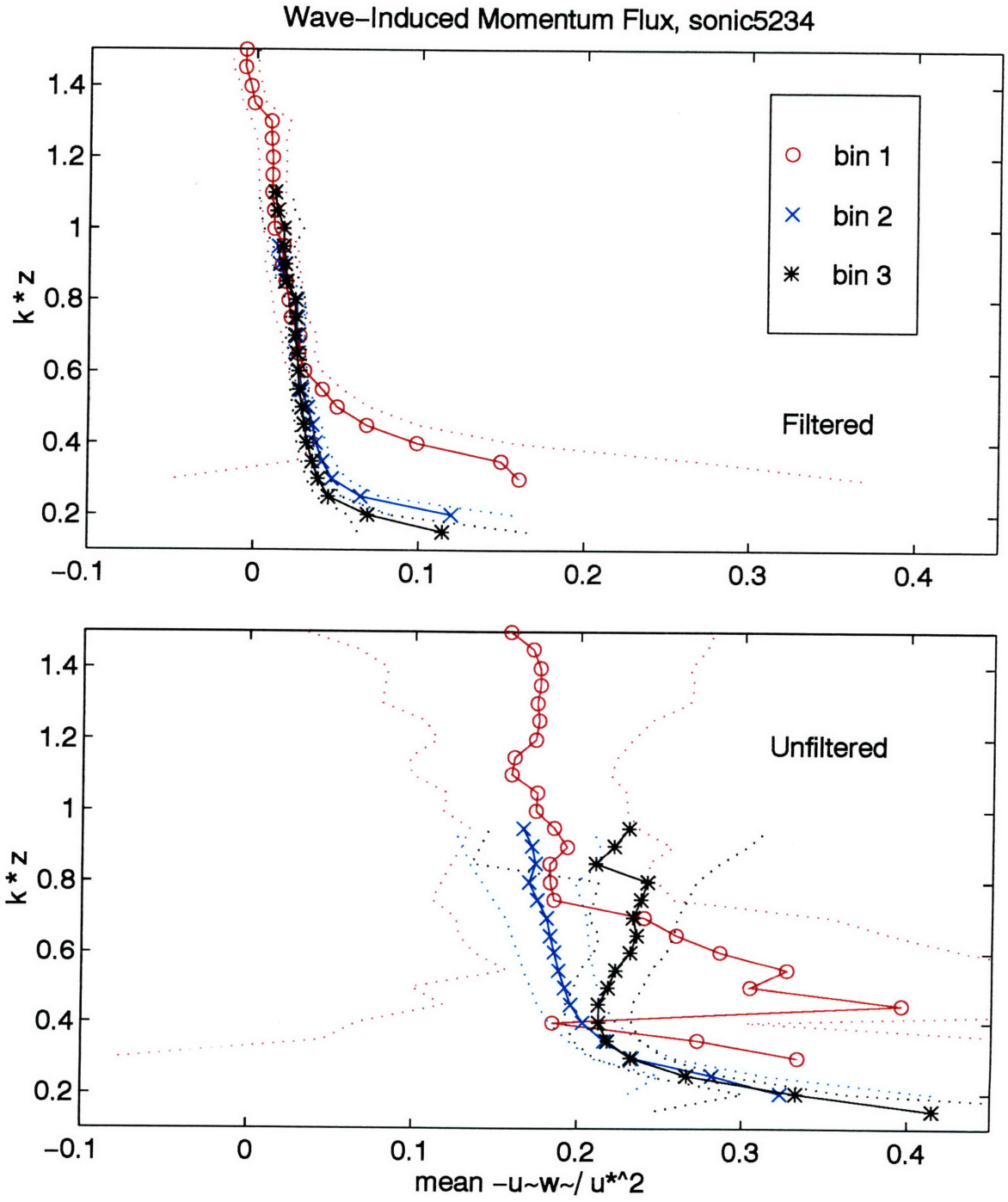

Figure A.3 Profiles of wave-induced momentum flux for bins 1-3 using filtered (top) and unfiltered (bottom) wind velocities in the analysis of the original results.

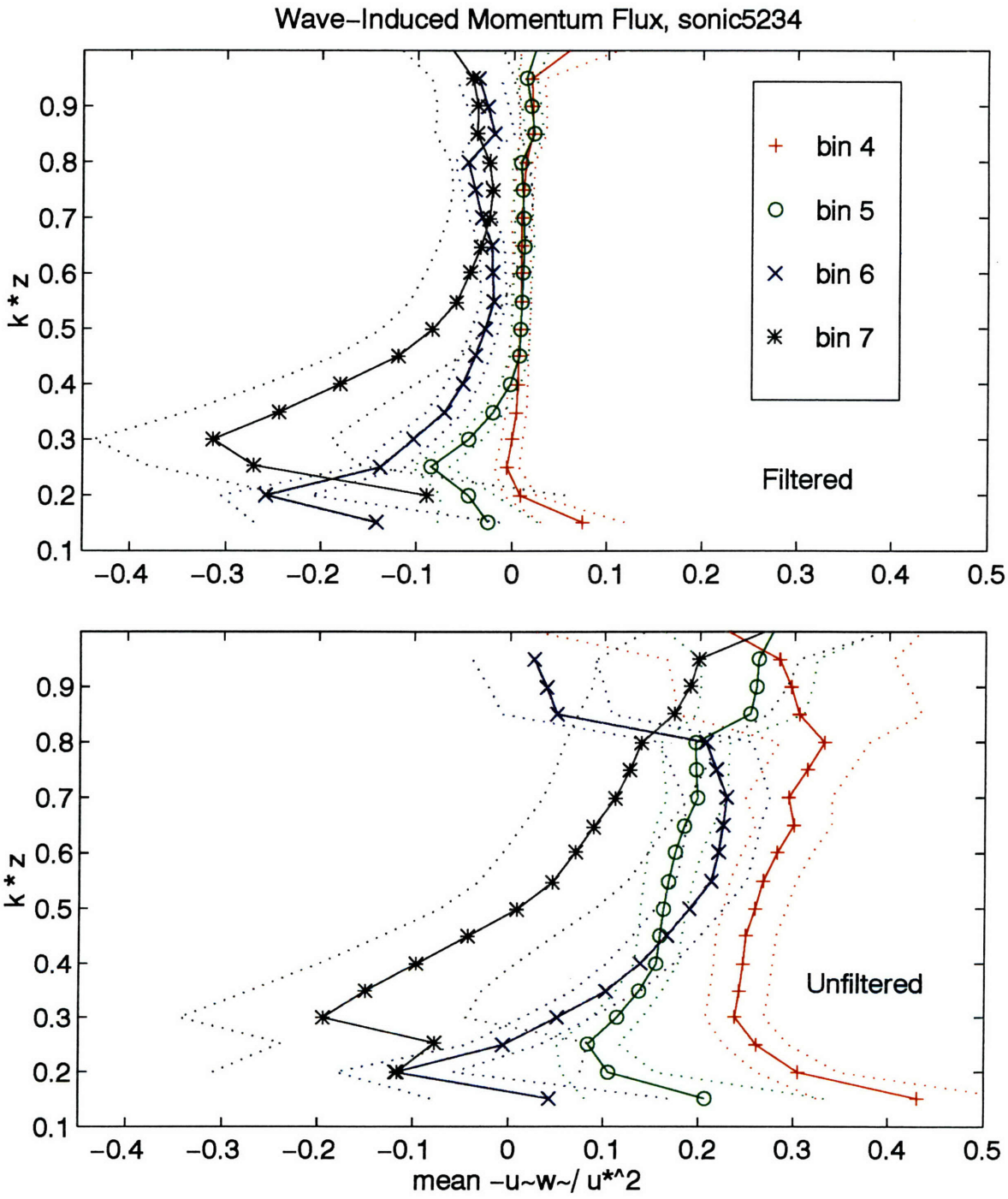

Figure A.4 Profiles of wave-induced momentum flux for bins 4-7 using filtered (top) and unfiltered (bottom) wind velocities in the analysis of the original results.

is, they generally tend towards 0.2 with height, instead of tending towards zero as expected; and the negative maxima are 0.2 greater than in the filtered results.

This feature is strikingly consistent in all the unfiltered results, and it is believed that the turbulent contributions to momentum flux that were not removed by phase averaging alone are responsible for the shift. Since turbulent momentum flux generally transfers momentum from the atmosphere to the surface (corresponding to a positive value for the quantity $-\overline{u'w'}$), the presence of any residual turbulent components in an estimate of the wave-induced momentum would translate the profiles to the right by an amount equal to the turbulent fraction remaining. Thus, the horizontal translation between the filtered and unfiltered results in figures A.3 and A.4 indicates that the turbulent reduction by filtering corresponds to 20% of the total momentum flux. Recall that the results from the simulation presented in Section 4.2 (Figure 4.10) demonstrate that phase averaging for one minute only reduces the turbulent fraction of total momentum flux by 10%. Figure 4.12 then shows that filtering before phase averaging decreases this turbulent fraction to 1.5%, indicating an additional 8.5% reduction of turbulence by filtering. A number of simplifications in the simulation and any remaining experimental or instrumental error could easily account for the difference between the estimate of turbulent reduction found by comparing the filtered and unfiltered wave-induced momentum flux profiles (20% of the total) and the estimate made from the results of the numerical simulation (8.5% of the total).

Thus it is entirely plausible that the difference between the filtered and unfiltered results shown in figures A.3 and A.4 is due to the influence of the turbulent fluctuations remaining in the velocity signal after phase averaging. This leads to the conclusion that filtering is an important part of the analysis technique, as it reduces the turbulent component of momentum flux by an additional 10-20% beyond the reduction by phase averaging alone. Additionally, since the filtered profiles consistently tend toward zero, it appears that the combination of filtering and phase averaging successfully removes all but a small fraction of the turbulent components.

A.3 Vertical Alignment of the Velocity Sensors

Finally, the lowest sonic anemometer used in the computations described in Chapter 5 was not aligned vertically with the rest of the sonic anemometers nor with the wave wire. This sonic was used because the horizontal velocity measurements of sonic 1, the lowest sonic on the mast, were unreliable. It was hung from the port boom, while the other instruments were located on the mast (see Section 3.1.1). The horizontal distance between sonic 5 and the wave wire was 3.7 m. Since the dominant wave trains were traveling with their crests nearly parallel to the boom, and their wavelengths ranged from 85 m to 125 m (i.e., much greater than the distance between sonic 5 and the mast) it was assumed that sonic 5 would accurately represent the conditions directly above the wave wire. This assumption will be investigated in a future study.